| | |
|---|---|
| **Titre:** Title: | GeSbSe as a Platform for Integrated Nonlinear Photonics |
| **Auteur:** Author: | Nicole Tebchrany |
| **Date:** | 2026 |
| **Type:** | Mémoire ou thèse / Dissertation or Thesis |
| **Référence:** Citation: | Tebchrany, N. (2026). GeSbSe as a Platform for Integrated Nonlinear Photonics [Mémoire de maîtrise, Polytechnique Montréal]. PolyPublie. https://publications.polymtl.ca/76587/ |



| | |
|---|---|
| **URL de PolyPublie:** PolyPublie URL: | https://publications.polymtl.ca/76587/ |
| **Directeurs de recherche:** Advisors: | Yves-Alain Peter |
| **Programme:** Program: | génie physique |

**POLYTECHNIQUE MONTRÉAL**
affiliée à l'Université de Montréal

# GeSbSe as a Platform for Integrated Nonlinear Photonics

**NICOLE TEBCHRANY**
Département de génie physique

Mémoire présenté en vue de l'obtention du diplôme de *Maîtrise ès sciences appliquées*
Génie physique

Mai 2026

**POLYTECHNIQUE MONTRÉAL**
affiliée à l'Université de Montréal

Ce mémoire intitulé :

**GeSbSe as a Platform for Integrated Nonlinear Photonics**

présenté par **Nicole TEBCHRANY**
en vue de l'obtention du diplôme de *Maîtrise ès sciences appliquées*
a été dûment accepté par le jury d'examen constitué de :

**Ludvik MARTINU**, président
**Yves-Alain PETER**, membre et directeur de recherche
**Stéphane VIRALLY**, membre

## DEDICATION

*To anyone curious or tenacious enough to read past the introduction...*
*And to those who never left my side, human or feline.*
*It's been quite a journey!*

## ACKNOWLEDGEMENTS

I want to start by thanking Yves-Alain Peter for welcoming me into his lab and indulging my interest in microfabrication. Thank you for pushing me and advising me throughout the years. I am incredibly grateful for all the opportunities you have afforded me, and I will forever cherish the memories and experiences from this time.

I also want to thank my colleagues at the Microphotonics Laboratory throughout the years: Ahmed S. Bahgat, Marc-Antoine Bianki, Richard Bienvenu Bomba, Khaled Elouaer, Vincent Girouard, Thomas Grenon, Régis Guertin, Thomas Lacasse, Thomas Lapointe, Cédric Lemieux-Leduc, Nicolas Malo, Salvador Poveda-Hospital, and Louis-Frédéric Racicot. Your advice and experience has been invaluable, and our discussions—research-related or otherwise—were always stimulating.

I am indebted to the professional staff at Polytechnique: Marie-Hélène Bernier, Christophe Clément, André Hoang-Goana, Alexandre Perron, Josianne Lefebvre, Bill Baloukas, Yves Drolet, Émile Jetzer, Mikaël Leduc, Jacques Massicotte; your knowledge and help were invaluable, and this project truly couldn't have been done without you. I also greatly appreciated all our non-technical conversations; your energy is infectious! I also could not have done half of the work presented here without Pierre-Luc Thériault, Abhay Anand, and Arnaud Petit: thank you for graciously lending me your time and your setup!

I would like to thank my friends, my family, and my cat for supporting me through every difficult moment. I especially want to thank Louis; without your support on those long evenings and weekends at the lab, I may never have accomplished this much. I also want to thank Sarah Albos for inspiring me with her hard work and for being by my side for so long. Michael, I am forever grateful for your encouragement, for your care, and for always believing in me.

Finally, I thank the jury members for agreeing to evaluate this work and for the time taken to do so.

# RÉSUMÉ

Le domaine émergent de la photonique quantique nécessite le développement de composantes telles que les sources de photons uniques ou les sources d'intrication. Ces sources peuvent être réalisées dans des guides d'onde et résonateurs sur puce, exploitant les propriétés optiques non-linéaires avantageuses de différents matériaux. Les verres de chalcogénure, incluant le $Ge_2Sb_2Se_5$ (GSSe), sont des matériaux à changement de phase ayant un potentiel démontré en applications d'optique non-linéaire grâce à leurs faibles pertes et leur non-linéarité de troisième ordre élevée. Par contre, la famille des chalcogénures démontre une grande variabilité en terme de ces propriétés, poussant la caractérisation de compositions diversifiées. L'objectif principal de ce mémoire est d'évaluer la pertinence du $Ge_2Sb_2Se_5$ dans ce contexte afin de permettre le futur développement de composantes non-linéaires plus complexes.

En premier lieu, des couches minces de $Ge_2Sb_2Se_5$ (GSSe) sont déposées par pulvérisation et recuites thermiquement. La composition matérielle de ces films est évaluée par spectroscopie photoélectronique à rayons X (XPS) et une déviation stœchiométrique pouvant atteindre près de 11% est mesurée. Une mesure d'ellipsométrie permet de trouver un indice de réfraction élevé ($n_0 \approx 2.9$) et des pertes négligeables à une longueur d'onde de 1550 nm. La technique du *z-scan* est utilisée pour trouver un indice non-linéaire ($n_2 \approx 2.9 \times 10^{-17}$ m$^2$/W) et de l'absorption à deux photons ($\beta_{2\text{PA}} \approx 7.2 \times 10^{-11}$ m/W) élevés, donnant un facteur de mérite comparable au silicium. Les couches minces recuites ont une réduction au niveau de ces deux propriétés ($n_2 \approx 0.81 \times 10^{-17}$ m$^2$/W, $\beta_{2\text{PA}} \approx 1.89 \times 10^{-11}$ m/W), plus importante pour l'absorption, améliorant ainsi légèrement le facteur de mérite et augmentant le seuil de dommage du matériau.

En second lieu, des guides d'onde et micro-résonateurs en anneau sont fabriqués à base de GSSe sur substrat de silicium, dans l'objectif de démontrer la réalisabilité d'expériences d'optique non-linéaire sur cette plateforme. Des guides d'ondes sont fabriqués ayant des pertes de propagation de l'ordre de $\approx 3.6$ dB/mm. La résonance est bien observée dans des micro-anneaux couplés à des guides d'onde de GSSe. Finalement, une expérience préliminaire de mélange à quatre ondes est réalisée. Ensemble, ces résultats servent à démontrer le potentiel du GSSe pour la fabrication future de sources de photons.

# ABSTRACT

Quantum photonics is an emerging field requiring the development of novel components such as single-photon and entanglement sources. These sources can be made by exploiting nonlinear optical phenomena in waveguides and micro-resonators on chip, using materials with high third-order nonlinearity and low absorption losses. Chalcogenide glasses, including $Ge_2Sb_2Se_5$ (GSSe), are phase-change materials which have demonstrated potential in such nonlinear photonics applications thanks to their suitable optical properties. However, within this material family, there is still a large variability in terms of nonlinearity and losses, giving rise to the necessity of characterizing more compositions in the form of thin films and waveguides. The primary objective of this thesis is to assess the performance of $Ge_2Sb_2Se_5$ in this context, in order to lay the groundwork for the development of more complex devices such as photon sources.

First, sputtered and annealed films of GSSe are characterized in terms of their material composition, linear optical properties, and nonlinear properties via z-scan measurement. We find that the composition of the films deviates from the theoretical $Ge_2Sb_2Se_5$ by up to 11%, but that the linear refractive index is elevated ($n_0 \approx 2.9$) and that linear losses are negligible at 1550 nm. From the z-scan, we obtain elevated Kerr index ($n_2 \approx 2.9 \times 10^{-17}$ m$^2$/W) and two-photon absorption ($\beta_{2\text{PA}} \approx 7.2 \times 10^{-11}$ m/W), yielding a figure of merit similar to that of silicon. Annealed films preliminarily saw a decrease in both properties ($n_2 \approx 0.81 \times 10^{-17}$ m$^2$/W, $\beta_{2\text{PA}} \approx 1.89 \times 10^{-11}$ m/W), with a greater decrease for two-photon absorption yielding a slightly improved figure of merit and an increased damage threshold.

The second half of this thesis is centred on fabricating $Ge_2Sb_2Se_5$ waveguides and resonators on silicon substrates in order to demonstrate the feasibility of conducting nonlinear optics experiments on this platform. Waveguides are fabricated with propagation losses of $\approx 3.6$ dB/mm. Resonance was demonstrated in GSSe micro-ring resonators. Finally, four-wave mixing was observed in GSSe waveguides, highlighting the potential of this material for the eventual fabrication of integrated photon sources.

# TABLE OF CONTENTS

# LIST OF TABLES

# LIST OF FIGURES

# LIST OF SYMBOLS AND ACRONYMS

| | |
|---|---|
| 2PA/TPA | Two-photon absorption |
| 3PA | Three-photon absorption |
| AFM | Atomic force microscopy |
| ChG | Chalcogenide glass |
| CL | Cody-Lorentz |
| CW | Continuous-wave |
| DSC | Differential scanning calorimetry |
| DTA | Direct transmission analysis |
| EBL | Electron-beam lithography |
| EDS | Energy-Dispersive X-ray Spectroscopy |
| FDE | Finite Difference Eigenmode |
| FDTD | Finite-Difference Time-Domain |
| FSR | Free spectral range |
| FWM | Four-wave mixing |
| GSSe | $Ge_2Sb_2Se_5$ |
| GST | $Ge_2Sb_2Te_5$ |
| MCN | Mean Coordination Number |
| MPA | Multi-photon absorption |
| MSE | Mean square error |
| OSA | Optical spectrum analyzer |
| PCM | Phase-change material |
| PIC | Photonic integrated circuit |
| RF | Radio-frequency |
| SEM | Scanning Electron Microscopy |
| SOI | Silicon-on-Insulator |
| SFWM | Spontaneous four-wave mixing |
| SPDC | Spontaneous parametric down-conversion |
| TE | Transverse electric |
| TL | Tauc-Lorentz |
| TM | Transverse magnetic |
| UV | Ultraviolet |
| XPS | X-ray Photoelectron Spectroscopy |
| XRD | X-ray Diffraction |

# LIST OF APPENDICES

# CHAPTER 1 INTRODUCTION

## 1.1 Context

The 2025 Turing Award was presented to Gilles Brassard and Charles H. Bennett for their contributions in the field of quantum information science. Notably, they are the creators of the first quantum cryptography protocol: BB84. In this scheme, Alice communicates with Bob via a quantum and a classical channel using polarized photons. She can choose between two bases, rectilinear (+: horizontal = 0, vertical = 1) or diagonal (×: diagonal = 0, anti-diagonal = 1) to encode her bit string. She selects a random basis for each bit, and sends the polarized photon to Bob. Next, Bob chooses his own list of random bases and measures the polarization of the received photons accordingly. If Bob chose the same basis as Alice, he should measure the same polarization and therefore will receive the correct bit. If Bob chose a different basis, he obtains a random bit. Using their classical communication channel, Bob shares his list of bases and Alice confirms which photons Bob measured in the correct basis. They discard the incorrectly measured bits, and compare their resulting bit strings. If the communication was not interrupted, they should have the same bit sequence.

In the event that Eve was eavesdropping on the quantum channel and intercepted Alice's photon string, she would have to use her own sequence of polarizations for measurement before sending the photons back to Bob. Eve faces the same challenge as Bob: she does not know Alice's bases, and thus risks altering the bit sequence Bob receives. Therefore, even when Alice confirms Bob's bases, they likely would have differences in their final keys. Below is an illustration of the process [8]:

| | | | | | | | | | |
|---|---|---|---|---|---|---|---|---|---|
| Alice's string | 0 | 1 | 1 | 1 | 0 | 0 | 1 | 0 | 1 |
| Alice's basis | × | × | × | + | + | × | + | + | × |
| Alice's photons | D | A | A | V | H | D | V | H | A |
| Eve's basis | × | + | + | + | × | × | + | × | × |
| Eve's photons | D | V | V | V | A | D | V | D | A |
| Bob's basis | + | × | + | + | × | × | × | + | × |
| Bob's photons | H | D | V | V | A | D | D | V | A |
| Bob's string | 0 | 0 | 1 | 1 | 1 | 0 | 0 | 1 | 1 |
| Bob's key | | 0 | | 1 | | 0 | | 1 | 1 |
| Alice's key | | 1 | | 1 | | 0 | | 0 | 1 |

This algorithm exploits the unique properties of quantum photonics to alert both parties

to the presence of an eavesdropper. Since then, developments to the field have been exponential, from the development of new quantum algorithms, to the fabrication of single photon detectors and emitters. Such hardware is essential to the realization of any quantum experiment.

### 1.2 Challenges and Motivation

As quantum computers become more and more powerful, the security of current encryption methods becomes more imminently fragile. It is therefore critical to have at hand the technology required to implement quantum-hardy algorithms. Among the necessary components are single photon sources. These sources must be efficient, but also accessible and resistant to external disruption. One interesting solution is to build the photon source on silicon chips, which provides the added benefit of being compact and lightweight.

Despite progress, the on-chip photon generation rate remains relatively low. As a result, we are required to use high-powered lasers, which are noisy and difficult to integrate. Therefore, we want to find materials with nonlinear optical properties that allow us to decrease the power requirements while obtaining elevated generation rates [9]. Recently, such a source was developed from the chalcogenide GeSbS [10], exploiting its photosensitivity to create a reconfigurable device. Other materials in this family may have more suitable properties for the creation of efficient nonlinear photonics sources, giving rise to the necessity of investigating them.

This work aims to investigate the usefulness of $Ge_2Sb_2Se_5$, a chalcogenide glass, as a platform for integrated nonlinear photonics as a means for the eventual fabrication of a photon source on chip.

### 1.3 Research Objectives

The main objective of this work is to assess the performance of $Ge_2Sb_2Se_5$ as a platform for integrated nonlinear photonics. This is broken down into the following sub-objectives:

1. Measure the linear and nonlinear optical coefficients of $Ge_2Sb_2Se_5$ in thin film form.
2. Fabricate waveguides using $Ge_2Sb_2Se_5$ and demonstrate linear transmission.
3. Observe nonlinear phenomena in $Ge_2Sb_2Se_5$ waveguides, namely four-wave mixing.

This work is exploratory in nature and aims to form the basis for future experiments with more complex designs from which a photon source could eventually be fabricated.

## 1.4 Thesis Outline

The thesis will begin with a brief overview of the basic concepts and theories in optics and materials necessary for the comprehension of this work. Then, a review of the literature regarding the proposed solution will be presented, focusing on materials for nonlinear optics and the characteristics of chalcogenides. The body of this thesis begins with the characterization of GSSe in thin film form, from a material composition perspective as well as a linear and nonlinear optical standpoint. Next, waveguides and resonators are fabricated using GSSe, showing preliminary results for nonlinear experiments. Finally, limitations and future work related to this study will be addressed in the conclusion.

# CHAPTER 2 THEORY

This chapter introduces the necessary theory which serves as the basis for the work discussed in this thesis.

## 2.1 Linear Optics

Integrated photonics refers to the development of optical components on-chip. The aim is to reduce the footprint of photonic devices by fabricating photonic integrated circuits (PICs), which use waveguides as the fundamental routing of light [11].

### 2.1.1 Optical Waveguides

The underlying principle which allows for electromagnetic waves to be guided is total internal reflection. This poses constraints on the insertion angle of light into the waveguide, known as the critical angle, $\theta_c$, as well as on the refractive indices of the waveguide core ($n_{\text{core}}$) and its cladding or substrate ($n_{\text{clad, sub}}$), such that

$$\theta_c = \arcsin\left(\frac{n_{\text{clad, sub}}}{n_{\text{core}}}\right) . \tag{2.1}$$

From Equation (2.1), it is clear that in a waveguide, total internal reflection occurs if light is travelling in a high index medium (core) surrounded by a lower index medium (cladding). Different rectangular waveguide geometries are presented in Figure 2.1.

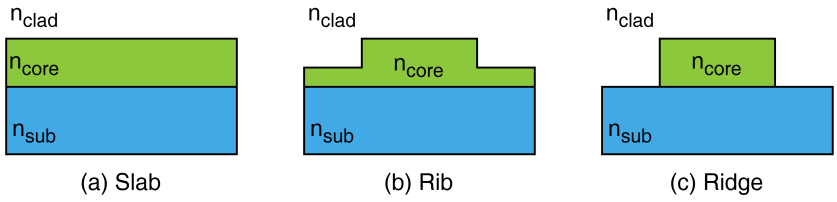


Figure 2.1 Types of waveguides.

The distribution of a scalar, monochromatic, plane electromagnetic field $\Psi$ in a slab waveguide with linear refractive index $n_0$ as exemplified in Figure 2.1 (a) is governed by the Helmholtz

equation:

$$\nabla^2\Psi + (k^2 n_0^2 - \beta_m^2)\Psi = 0 \ . \tag{2.2}$$

In Equation (2.2), the eigenvector solutions represent the spatial distribution of the field $\Psi$, called modes. The corresponding eigenvalue to each mode is the propagation constant $\beta_m$, which is defined as

$$\beta_m = n_{\text{eff}}\, k \ . \tag{2.3}$$

In Equations (2.2) and (2.3), $k$ is the wavenumber, given by $k = \frac{2\pi}{\lambda}$, with $\lambda$ being the wavelength. The effective refractive index $n_{\text{eff}}$ determines the degree of confinement of a mode within a waveguide, and must obey the following inequality [12]:

$$n_{\text{clad, sub}} < n_{\text{eff}} < n_{\text{core}} \ . \tag{2.4}$$

The closer $n_{\text{eff}}$ is to $n_{\text{core}}$, the more tightly the mode is confined within the waveguide, reducing the mode area.

### 2.1.2 Optical Losses

For a medium with losses, the linear refractive index $n_0$ is a complex quantity, such that

$$n_0 = n_0' + i n_0'' = n + i\kappa \ . \tag{2.5}$$

The imaginary part of $n_0$ is tied to the propagation losses in the medium and is also known as the extinction coefficient $\kappa$. From this quantity, the absorption coefficient $\alpha$ is given by

$$\alpha = \frac{4\pi\kappa}{\lambda} \ , \tag{2.6}$$

which describes the attenuation of a field's intensity $I_0$ over a propagation distance $z$ such that

$$I(z) \sim I_0\, e^{-\alpha z} \ . \tag{2.7}$$

## 2.2 Nonlinear Optics

Nonlinear optics refers to a regime where the refractive index of a material becomes modulated by the presence of light. The polarization $\mathbf{P}(t)$ of the system under an electric field $\mathbf{E}(t)$,

assuming instantaneous response for simplicity, can be expanded as [13]

$$\mathbf{P}(t) = \varepsilon_0[\chi^{(1)}\mathbf{E}(t) + \chi^{(2)}\mathbf{E}^2(t) + \chi^{(3)}\mathbf{E}^3(t) + \cdots] \ , \tag{2.8}$$

where $\epsilon_0$ is the vacuum permittivity and $\chi^{(i)}$ is the optical susceptibility of order $i$. The second-order susceptibility, $\chi^{(2)}$, produces a larger effect than $\chi^{(3)}$, but it is only present in non-centrosymmetric crystals [13], which greatly reduces the access to these phenomena. This study will mainly focus on third-order effects.

Recalling the relationship between susceptibility and refractive index

$$n = \sqrt{1 + \chi} \ , \tag{2.9}$$

we can then describe refractive index in the presence of third-order nonlinearity with

$$n = n_0 + n_2 I \ , \tag{2.10}$$

where $n_0 = \sqrt{1 + \chi^{(1)}}$ is the linear refractive index, $I$ is the intensity of the optical field, and $n_2$ is the intensity-dependent nonlinear refractive index, defined as [13]

$$n_2 = \frac{3}{4n_0^2\varepsilon_0 c}\Re(\chi^{(3)}) \quad \left[\frac{\mathrm{m}^2}{\mathrm{W}}\right] \ . \tag{2.11}$$

This nonlinear index is also known as the Kerr index. We will now investigate a few third-order nonlinear effects in more detail.

### 2.2.1 Kerr Lensing

One possible effect of the third-order nonlinearity is Kerr lensing, which can lead to self-focusing of a beam in a nonlinear material with positive $n_2$, or self-defocusing for a negative $n_2$. From Equation 2.10, it is clear that for a sufficiently intense optical field, the overall refractive index $n$ will be modulated, either increased or decreased depending on the sign of $n_2$. The spatial distribution of the beam $I(x, y)$ will consequentially induce spatial variations in $n(x, y)$ [11]. Taking the example of a Gaussian beam, the intensity is maximal at the centre and decays radially, leading to a corresponding refractive index gradient in the material, thus causing the lensing effect. This is illustrated in Figure 2.2.

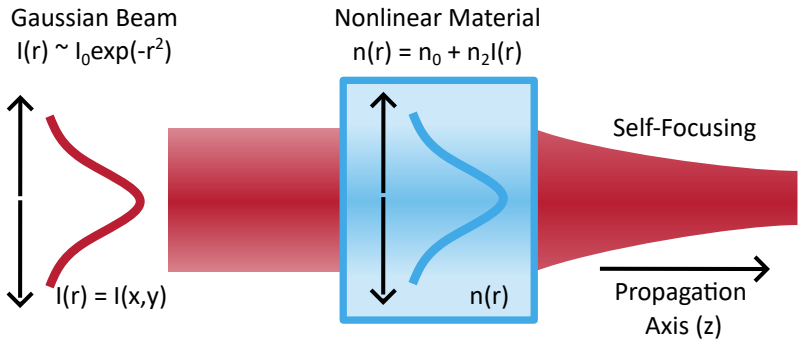


Figure 2.2 Illustration of Kerr self-focusing for $n_2 > 0$.

This phenomenon is exploited in the z-scan technique in order to characterize the nonlinear index of a material, which will be discussed in further detail in Chapter 4.5.

### 2.2.2 Four-Wave Mixing

Four-wave mixing (FWM) is a third-order nonlinear optical process involving the interaction of four electromagnetic waves: $\omega_1$, $\omega_2$, $\omega_3$, and $\omega_4$. The overall interaction of these waves must obey energy conservation, for example:

$$\omega_1 + \omega_2 = \omega_3 + \omega_4 \ . \tag{2.12}$$

They must also obey momentum conservation, leading to the following phase-matching requirement:

$$k_1 + k_2 = k_3 + k_4 \ , \tag{2.13}$$

where $k_x = \frac{2\pi n_0}{\lambda_x}$ is the wavenumber in the medium of refractive index $n_0$.

In the case of *degenerate* FWM, the input consists of two pump photons of the same frequency $\omega_1 = \omega_2 = \omega_\mathrm{p}$ which generate the signal frequency $\omega_3 = \omega_\mathrm{s}$ and the idler frequency $\omega_4 = \omega_\mathrm{i}$, such that Equations (2.12) and (2.13) become

$$\begin{aligned} 2\ \omega_\mathrm{p} &= \omega_\mathrm{s} + \omega_\mathrm{i} \ , \\ \frac{2}{\lambda_\mathrm{p}} &= \frac{1}{\lambda_\mathrm{s}} + \frac{1}{\lambda_\mathrm{i}} \ , \end{aligned} \tag{2.14}$$

and

$$2\ k_\mathrm{p} = k_\mathrm{s} + k_\mathrm{i} \ , \tag{2.15}$$

where $\lambda_x$ and $\omega_x$ are the wavelength and frequency of $x = \mathrm{p}, \mathrm{s}, \mathrm{i}$ being the pump, signal, or idler waves respectively.

In the classical regime, the signal beam $\omega_\mathrm{s}$ is also inputted in addition to the stronger pump beam $\omega_\mathrm{p}$ in order to drive generation of the idler $\omega_\mathrm{i}$. This is called *seeded* or *stimulated* four-wave mixing. The quantum equivalent requires no seeding from the signal, and is instead driven by vacuum fluctuations. This is referred to as *spontaneous* four-wave mixing (SFWM). Both processes are illustrated in Figure 2.3.

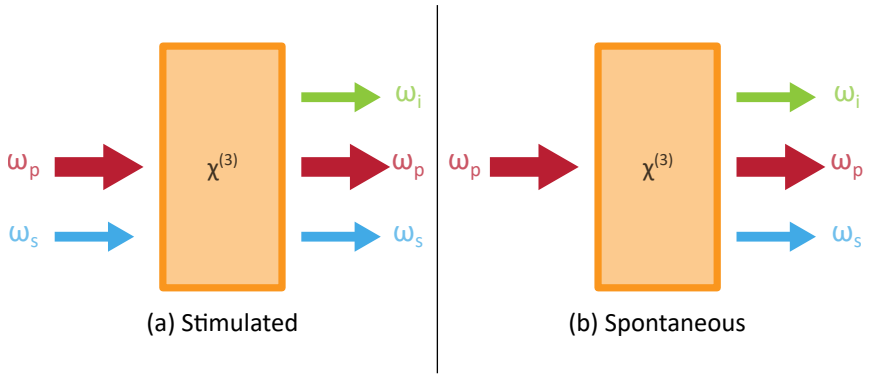


Figure 2.3 (a) Stimulated and (b) spontaneous four-wave mixing.

### 2.2.3 Multi-Photon Absorption

The nonlinear counterpart to linear absorption is multi-photon absorption (MPA). This phenomenon occurs when a material's electrons are excited from the ground state due to the absorption of $N$ photons providing combined sufficient energy for that transition. For this reason, the rate of MPA is directly related to a material's bandgap energy, which represents the minimum photon energy required for absorption and excitation. The rate of MPA naturally decreases with higher orders of $N$, given the decreased probability of interaction as the number of photons increases. The lowest order, where $N = 2$ is two-photon absorption (2PA or TPA, represented by $\beta_{2\mathrm{PA}}$), with the next being three-photon absorption (3PA), represented by $\beta_{3\mathrm{PA}}$. Using these coefficients, the total absorption of the material can be described in a manner analogous to the Kerr index in Equation (2.10):

$$\alpha_{\mathrm{tot}} = \alpha + \beta_{2\mathrm{PA}}\, I \; + \beta_{3\mathrm{PA}}\, I^2 \;, \tag{2.16}$$

where $\alpha$ is the linear absorption coefficient of the material.

## 2.3 Chalcogenides

Chalcogenides are a family of materials formed with any of the chalcogen elements S, Se, and/or Te in combination with other elements. These materials are phase-change materials (PCMs). They can exist in amorphous, glassy states, where they are often referred to as chalcogenide glasss (ChGs), as well as in ordered, crystalline states. More precisely, they are nonvolatile PCMs, in that once the material is in a given state, it will remain so until enough energy is provided to induce the change. This is in contrast to volatile PCMs, such as $VO_2$, which can change phases near room temperature, making them less stable without active control.

In particular, PCMs show markedly different material properties in either phase. For example, many ChGs show large refractive index and absorption modulation upon undergoing crystallization, which is useful for the development of reconfigurable photonic devices [14,15]. ChGs have been used for infrared photonics due to their typically large transparency. Even in their amorphous state, they can still possess short-range order, which leads to the observation semiconducting behaviour in the form of bandgap energy, which is a result of local electronic configuration [16,17].

In ChGs, films are typically deposited in amorphous form. They can be crystallized to various degrees by thermal processes, since crystallization is a process typically initiated by nucleation. Important temperatures include the glass transition temperature, $T_\mathrm{g}$, the nucleation temperature $T_\mathrm{N}$, and the crystallization temperature $T_\mathrm{c}$. The glass transition temperature is an experimental quantity related to the viscosity of the glass melt. $T_\mathrm{N}$ is the temperature at which the nucleation process reaches its maximum rate, to enable to formation of a crystalline structure. At $T_\mathrm{c}$, crystallization rate is maximized. The stability of a glass is often calculated as $T_\mathrm{x} - T_\mathrm{g}$, where $T_\mathrm{x}$ is the crystallization *onset* temperature, with a larger difference being desirable to avoid unwanted crystallization [18].

Chalcogenide glasses also have been known to exhibit photosensitive refractive index changes. One unique quality is the ability to reversibly alter the bandgap energy of amorphous chalcogenides using illumination. If $E_\mathrm{g}$ tends to longer wavelengths, this is known as photodarkening, while the contrary is referred to as photobleaching. After illumination, the original state of the material can be recovered using annealing near the glass transition temperature [17]. This phenomenon is distinct from the phase change described previously, but is nonetheless believed to be a result of structural changes. This reconfigurability allows for refractive index tuning, which can be exploited in the fabrication of photonic micro-resonators [10].

# CHAPTER 3 LITERATURE REVIEW

## 3.1 Photon Sources

There are two main approaches used for the generation of single photons. The first relies on solid-state sources, such as quantum dots. The second approach generates quantum states of light via nonlinear photonic platforms.

Solid-state sources such as quantum dots have the advantage of being semi-deterministic, meaning light is generated nearly on-demand (while still being limited by time-energy uncertainty), which allows for more reliable control on the user's part. However, since these sources operate with confined matter on a small scale, they are experimentally resource-intensive, require cryogenic cooling, and suffer from photon losses in device coupling [9].

Sources based on nonlinear photonics are probabilistic in nature, as they inherently rely on processes which are statistical and random: quantum vacuum fluctuations. The advantage of photonic sources lies in their comparatively inexpensive operation, as well as the ease of their production and integration into systems with PICs. The nonlinear phenomena which are principally exploited for these types of sources are spontaneous parametric down-conversion (SPDC) and spontaneous four-wave mixing (SFWM) [9, 19]. The following work focuses on the latter.

### 3.1.1 Nonlinear Photonics Sources

Nonlinear photonics sources make use of materials exhibiting elevated second- or third-order susceptibility and low absorption. Second-order phenomena include second-harmonic generation, sum- and difference-frequency generation, and spontaneous parametric down-conversion. Third-order phenomena include third-harmonic generation, stimulated Raman scattering, stimulated Brillouin scattering, self- and cross-phase modulation, and four-wave mixing [13, 19, 20].

SPDC is a $\chi^{(2)}$ phenomenon, which technically makes it a more efficient process over SFWM. However, since it is only accessible in non-centrosymmetric media, the platforms upon which SPDC sources can be built are quite limited. Phase matching conditions are more difficult to achieve than for SFWM, since the wavelength separation between the pump, signal, and idler photons is usually much larger for SPDC. There are techniques to break material symmetry and achieve so-called *quasi*-phase-matching such as periodic poling of the material [19]. The most commonly used material in this process is lithium niobate ($LiNbO_3$). There have also

been experiments where glasses, including chalcogenides, have been periodically poled to achieve a $\chi^{(2)}$ response [21].

SFWM, as described in Chapter 2, is a $\chi^{(3)}$ process. While theoretically less efficient than SPDC, every material can exhibit a $\chi^{(3)}$ response, drastically widening the candidate pool for potential platforms. Additionally, SFWM is a process relying on two pumps, which can confer an advantage in terms of customization of the output states, as well as in potential source brightness, since the generation rate scales quadratically with pump power instead of linearly as for SPDC [22]. Another important characteristic is the purity of the source, which is the degree to which only one photon is generated on command. This can be measured by evaluating the coincidence counts across two detectors after passing through a beam splitter: if only one photon is produced, both detectors will not have a simultaneous measurement [22]. The fidelity of these photons, i.e. the similarity between the generated photons and their target states, is another important criterion [22, 23].

Overall, both SPDC and FWM processes have been used to demonstrate purity $> 90\%$, collection efficiency $> 80\%$, and entanglement fidelity $> 95\%$ [22]. The rest of this review focuses on $\chi^{(3)}$ materials for FWM.

### 3.1.2 Methods to Characterize Nonlinear Response

As the key property for FWM is the third-order susceptibility, the Kerr index $n_2$ must be adequately characterized to evaluate a material's suitability in this application. Furthermore, acquiring this data is valuable for the creation of a material "inventory" researchers can use to select the optimal composition for their experiment [20].

#### Waveguides

In the case of integrated PICs, the material under study is typically ultimately patterned into a waveguide. It is therefore desirable to understand the nonlinear behaviour of the material in this final form. One common technique for obtaining $n_2$ of a waveguide is through self-phase modulation experiments. This involves injecting ultrashort laser pulses (typically femto- or picosecond duration) into a waveguide, and observing the spectral broadening of the output at varying input powers in comparison. In order to model the results, the nonlinear Schrödinger equation must be solved. This is typically done using the split-step algorithm, which numerically calculates the propagation of the field in the waveguide in steps. While this method is not particularly complex in terms of experimental setup given the appropriate equipment, the analysis of the expected results can be challenging when accounting

for dispersion. Other challenges include decoupling substrate influence, considering geometry variations over the propagation length, and precise knowledge of the confinement of the beam within the waveguide [24–26].

### Bulk and Thin Film

One way to circumvent the complex modelling required for waveguide $n_2$ calculation is to measure the value in the bulk material. One of the most commonly used techniques for this is the z-scan method [27], which will be further described in Chapter 5. The z-scan technique allows the measurement of $n_2$ and $\beta_{\text{2PA}}$ by exploiting the Kerr lensing effect described in Chapter 2.2.1. The experimental setup is somewhat more complex than in the case of self-phase modulation. However, modelling of the sample's response is typically more straightforward. In the case of a bulk material, no substrate is present, and the measurement is highly localized, which reduces experimental uncertainty.

The drawback of bulk measurements is not in the difficulty of validating the results, but rather that the measurement is not extracted from the material's thin film form. In the context of integrated photonics, thin films are prepared from bulk using various deposition techniques; the process by which a material is deposited can inherently affect its morphology, structure, stoichiometry, and density. As a result, discrepancies between bulk $n_2$ and thin film or waveguide $n_2$ values have been reported [28–31]. Additionally, using a technique such as the z-scan on mm-thick samples can cause parasitic effects if the irradiation intensity is too high, obscuring true two-photon absorption traces [2].

As a result, for the target application of integrated photonics, the measurement of nonlinear coefficients should study the material in thin film form, to account for any modifications induced by the deposition technique which will be used for subsequent patterning on chip. The z-scan technique can be applied to thin films, with considerations for substrate contribution, and remains less complex than waveguide characterization in terms of analysis, resulting in a more reliable outcome.

## 3.2 Materials for Third-Order Nonlinear Photonics

In order for a material to be useful in nonlinear photonic applications, it must have low linear and nonlinear losses (MPA), as well as a high nonlinear refractive index. We will consider these properties at the 1550 nm wavelength range. Additional considerations include material availability, toxicity, damage threshold, and CMOS-compatibility.

### 3.2.1 Silicon

Silicon is the material of choice for integrated chip photonics. Its high linear refractive index and low absorption in the near-infrared range make it a widely used platform for integrated photonics, often in Silicon-on-Insulator (SOI) devices. Silicon also presents an elevated third-order nonlinearity, but presents two-photon absorption (2PA) [19] and free-carrier absorption, which limits the performance of nonlinear devices [6,32]. Variations on standard silicon which have been explored for nonlinear photonics include hydrogenated amorphous silicon (a-Si:H), which has shown an increase in nonlinear refractive index with respect to its crystalline counterpart [33–35].

### 3.2.2 Silica Glass

Several forms of silica glasses exist, the most common of which is fused silica (FS), serving as a common benchmark material for the comparison of nonlinear optical performance [20]. Fused silica has the advantage of possessing negligible 2PA, but has a lower linear and nonlinear refractive index than silicon. A notable variant includes Hydex, a high-index doped silica glass, which also shows an enhanced Kerr index and broad transparency [36, 37].

### 3.2.3 Silicon Nitride

Stoichiometric silicon nitride, $Si_3N_4$, is a platform with growing popularity and has become widely available as a standard material in foundries. Silicon nitride has higher linear and nonlinear refraction than silica [37]. More recently, non-stoichiometric, silicon-rich nitride (SRN) has proven to be a useful material candidate, given the possibility of tuning its properties between that of stoichiometric nitride and silicon itself [38].

### 3.2.4 III-V Materials

Semiconductor alloys in general are commonly used materials for nonlinear optics experiments. In particular, materials from the III-V family are of interest, namely AlGaAs. Such alloys have optical properties which can be tuned by adjusting the proportion between each element, and show more elevated $n_2$ than silicon [20, 25]. However, it is worth noting that these materials are not CMOS-compatible due to the growth process. Other common III-V semiconductors include GaAs, which suffers from high absorption at 1550 nm [39], and is therefore better suited for mid-infrared applications.

### 3.2.5 Chalcogenides

Chalcogenides have been studied as platforms for nonlinear optics, in part thanks to their ability to be integrated into optical fibres [20]. Similarly to the semiconductors described previously, the variety of alloys and stoichiometric compositions allows for a vast repertoire of materials with differing nonlinear and linear optical properties.

### 3.2.6 Summary

The following table broadly summarizes some of the optical properties of materials of interest for third-order nonlinear photonics.

Table 3.1 Summary of optical material properties at 1550 nm.

| Material | | $n_0$ | Absorption ($\alpha$) [dB/cm] | Kerr Index ($n_2$) [$\times 10^{-18}$ m$^2$/W] | 2PA ($\beta_{2PA}$) [$\times 10^{-11}$ m/W] | Ref. |
|---|---|---|---|---|---|---|
| Si | c-Si | 3.48 | - | 6.7 | 1.03 | [40, 41] |
| | a-Si:H | 3.4 | $4.2 - 370$ | $21 - 74.3$ | $0.25 - 6.7$ | [33–35, 42] |
| $SiO_2$ | FS | 1.44 | - | 0.02 | - | [7, 43] |
| | Hydex | 1.45-1.8 | $< 0.06$ | 0.11 | - | [36] |
| SiN | $Si_3N_4$ | 2 | 0.5 | 0.26 | - | [44] |
| | SRN | 2.2-3.1 | 10 | 28 | - | [45] |
| III-V | AlGaAs | 3.34 | 0.4 | 15 | $< 0.15$ | [46] |
| | GaP | 3.1 | 1.2 | 12 | - | [47] |
| ChG | $As_2S_3$ | 2.29-2.43 | 0.05 | 2.92 | $< 0.01$ | [2, 48] |
| | $As_2Se_3$ | 2.81-2.84 | 0.009 | 12.7 | $< 0.16$ | [2, 49, 50] |
| | GeSbS | 2.18-2.6 | $\approx 0.5$ | $0.93 - 5.94$ | $< 0.13$ | [5, 28, 51] |
| | GeSbSe | 2.42-2.89 | 0.8 | 5.3-20.3 | $< 0.44$ | [1, 49, 52] |

As we can see from Table 3.1, the ChG family shows broad variations in optical properties, with refractive indices spanning $2.18 - 2.89$, nonlinear indices differing by a factor of 20, and low losses. This table is far from an exhaustive list, and in reality we can find even greater variability. Given this family's versatility, as well as their photosensitivity, they are good candidates for nonlinear integrated photonics. Having established this material family's position in the larger material landscape, we will explore it in more depth in the next section.

### 3.3 Chalcogenides – GeSbSe

From the chalcogenide family, the GeSbSe (GSSe) system is promising for its high reported $n_0$ and $n_2$ values. This ternary alloy is typically formed from a combination of GeSe or $GeSe_2$ with $Sb_2Se_3$. Within this group, we still find a large variation of linear and nonlinear refractive indices reported, in part due to variations in experimental methods used to determine the values, but also as a result of variations in composition. For example, Wang et al. performed z-scan measurements on millimetre-thick bulk samples of $Ge_xSb_ySe_{100-x-y}$, and found $n_0 = 2.533 - 2.863$, $n_2 = 5.95 - 14.9 \times 10^{-18}$ m$^2$/W, and $\beta_{2PA} \approx 0 - 0.37 \times 10^{-11}$ m/W, using the same methodology for different compositions [2]. This highlights the importance of understanding the precise stoichiometry of a given chalcogenide for the accurate reporting of optical properties. From this study, the composition which was found to have highest $n_2$ was $Ge_{22.5}Sb_{20}Se_{57.5}$, but no 2PA value was reported. Additionally, FWM has been demonstrated in hybrid silicon and $Ge_{28}Sb_{12}Se_{60}$ ring resonators, with a nonlinear parameter $\gamma_{NL} = 11.6$ W$^{-1}$m$^{-1}$ with a conversion efficiency up to $-37.1$ dB [53]. In simple ridge waveguides using $Ge_{12.5}Sb_{25}Se_{62.5}$, self-phase modulation and FWM were demonstrated with a conversion efficiency of $-42.6$ dB in the 1550 nm range [24].

This work will focus on $Ge_2Sb_2Se_5$ (or $Ge_{22.2}Sb_{22.2}Se_{55.6}$), a stoichiometric pseudo-binary glass from the $(GeSe)_{1-x}(Sb_2Se_3)_x$ system, with $x = \frac{1}{3}$. Prior work using this specific material include characterization of its linear optical properties via ellipsometry, which revealed it to have a large transparency window, from about $1 - 18.5$ µm in its amorphous form [15]. This composition's $n_2$ has not been reported, but based on the measurements of similar composition by Wang et al., it is expected to show a similarly elevated value. Conversely, elevated $n_2$ was found for materials with Mean Coordination Number (MCN) over 2.7 or below 2.4 [49]. MCN is calculated as a sum of each element's coordination number multiplied by the atomic percentage in the compound. The coordination numbers for Ge, Sb, and Se are respectively 4, 3, and 2. Thus, for $Ge_2Sb_2Se_5$, the MCN is estimated to be around 2.67, which is close to the observed threshold, although still in the intermediate range [54]. This implies that as a stoichiometric compound, the $n_2$ may be relatively lower for $Ge_2Sb_2Se_5$ than for other compositions which have higher proportions of homopolar bonds, particularly the highly polarizable Sb-Sb bond [49, 55]. Nevertheless, given the variations induced by deposition and the experimental measurements, we expect this composition to perform well as a nonlinear material [56].

# CHAPTER 4 THIN FILM CHARACTERIZATION

In this chapter, GSSe will be characterized in thin film form to better understand its properties for future fabrication efforts. Thin film chalcogenides exhibit different optical properties from their bulk counterparts [57]. Additionally, any deposition technique may result in stoichiometric deviations from the target composition, which can highly influence the optical properties [58]. It is therefore important to confirm the film composition. Chalcogenides are also prone to oxidation, which may be problematic for device production [52]. Finally, annealing can alter the linear and nonlinear optical properties of chalcogenide films [58]. As a result, this section aims to study the thin film characteristics of sputtered $Ge_2Sb_2Se_5$ in order to complete sub-objective 1.

## 4.1 Film Sample Preparation

### 4.1.1 Deposition Technique

There are three main physical vapour deposition techniques used for chalcogenides: sputtering, evaporation, and pulsed laser deposition. Sputtering preferentially conserves the target stoichiometry as opposed to evaporation [59]. Thermal evaporation has also been shown to increase crystallinity and thus reduce nonlinearity in GeSbSe chalcogenide films in comparison with the bulk material [58]. Pulsed laser deposition has been shown to decrease the selenium in proportion to the target composition but to a minimal extent [60].

Overall, sputtering is one of the preferred deposition techniques for chalcogenide photonics as it provides good adherence and uniformity [57,61]. While sputtering is considered to preserve target stoichiometry, varying the deposition parameters (radio-frequency (RF) power, gas pressure, flow, etc.) can still result in composition deviation, which can in turn strongly affect the optical properties of the film [3, 57, 58, 62].

Furthermore, chalcogenides exhibit different optical properties in thin film form and in bulk [63]. One explanation is that following deposition, the chemical bonds are rearranged and contain a greater proportion of defects including homopolar bonds, dangling bonds, and voids. These structural changes are associated with increased optical absorption [29].

All GSSe films were prepared using RF magnetron sputtering (target 1: Angstrom Sciences, USA; target 2: SCSM, Canada) at the Microfabrication Laboratory at Polytechnique Montréal. The chosen recipe consisted of a power of $50 - 75$ W, 5 mTorr pressure, 10 sccm argon flow rate, yielding an approximate deposition rate of $20 - 35$ nm/min. The use of different

targets must be taken into account when drawing comparisons between the films.

### 4.1.2 Annealing

After depositing the films, some samples were post-processed by annealing. Thermal annealing can alter the optical properties of ChG films and relax the bonds towards the structure of bulk glass, potentially mitigating optical losses [29]. Reflowing has also been used to decrease the surface roughness of GSSe waveguides in order to decrease scattering losses [52]. In this work, annealing is explored in an attempt to increase the bandgap energy and thus reduce linear and nonlinear optical losses at the target wavelength of 1550 nm.

Chalcogenides being phase-change materials, care must also be taken to avoid unwanted crystallization, which is associated with increased absorption in the case of $Ge_2Sb_2Se_5$ [15]. As such, the temperature range for annealing must be chosen with careful consideration of the crystallization onset temperature, as well as the glass transition temperature $T_g$. A common approach for relaxing chalcogenide films without inducing crystallization is to anneal them at $T_g - 30$ K. This gives sufficient energy for slight structural rearrangements to reduce stress without overstepping into crystallization ranges [18]. It is worth noting that these temperatures, typically measured on bulk or powdered samples, can fluctuate in practice as a result of film thickness and the film's substrate [64, 65].

#### Annealing recipe

Literature reports a glass transition temperature of about 245 °C for $Ge_2Sb_2Se_5$, with crystallization onset at $T_c \approx 300$ °C for a heating rate of 10 °C/min [66, 67]. Following the guideline for film relaxation at $T_g - 30$ K, the temperature is chosen to be 215 °C, which should be well below the crystallization threshold for $Ge_2Sb_2Se_5$. The relaxed samples are annealed in a furnace with constant nitrogen flow, with a temperature ramp of 2.5 °C/min, a 1 hour plateau at 215 °C, and a ramp down which consisted of turning off the oven. One set of samples was annealed at 400 °C for 3 minutes with a heating rate of 10 °C/min, which allowed us to observe the crystallization process.

## 4.2 Sample Appearance and Crystallization

### 4.2.1 Optical Microscope

The films were visually inspected following sputtering and following annealing.

The first set of samples was prepared as 400 nm-thick GSSe films sputtered on silicon with

5 µm of oxide. Since the eventual nonlinear characterization by z-scan requires thicker films, a second set of samples was prepared by sputtering approximately 2.2 µm of GSSe on thin 150 µm borosilicate glass cover slides. For each type of substrate, one sample was investigated in its as-deposited state, after a 215 °C annealing, and a 400 °C annealing as described in Chapter 4.1.

Upon withdrawing these samples from the oven, there was a change to the surface of the thicker, cover glass annealed samples which was visible to the naked eye. The surfaces were inspected with an optical microscope, with photographs presented in Figure 4.1.

The 215 °C cover glass sample showed a subtly cloudier surface visible to the naked eye under certain angles, but optical microscopy did not reveal any significant crystallization, as can be seen in Figure 4.1 (c).

The 400 °C cover glass sample showed signs of crystallization visible to the naked eye upon withdrawing it from the oven, while the thinner film on the oxidized silicon substrate did not appear strikingly different from its as-deposited counterpart. Closer inspection under an optical microscope revealed nucleation in both 400 °C films, as presented in Figure 4.1 (e) and (f).

Overall, in Figure 4.1, we can see that both the as-deposited and 215 °C annealed samples have relatively smooth surfaces regardless of the film thickness or substrate. At 400 °C, both the cover glass and silicon samples show clear signs of crystallization. The cover glass sample, which is thicker, shows significantly more pronounced nucleation. It is worth noting that all three cover glass samples had more surface defects to begin with, which could be a result of residue following the removal of tape used during the sputtering process, or could even be attributed to the longer deposition time, potentially generating more substrate heating, which could result in film defects. These defects, whether residual dust on the surface or film variations, are highly likely to precipitate the nucleation process. The 400 °C samples will not be studied for nonlinear effects as a result of their heterogeneous and diffusive surfaces.

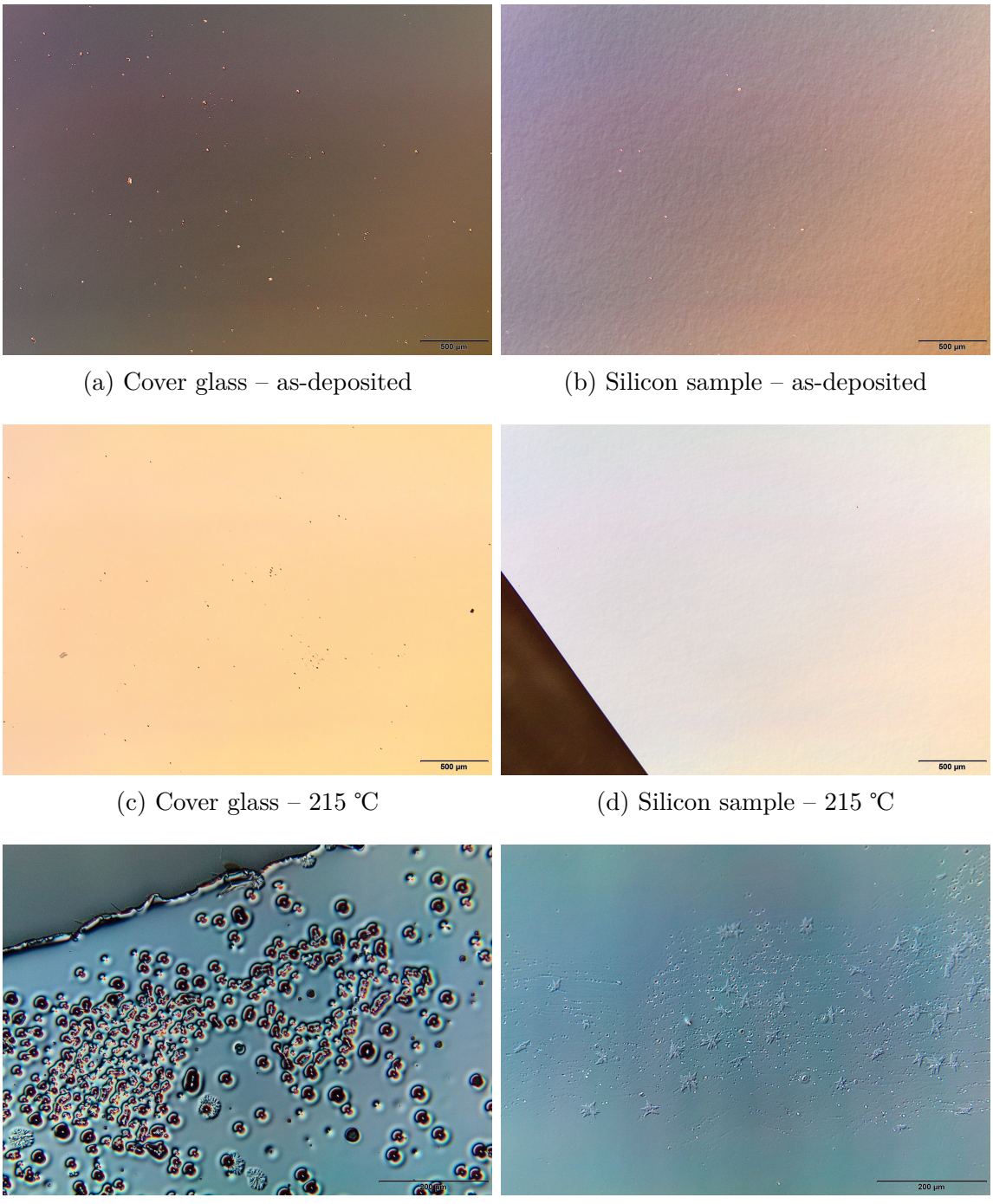

(a) Cover glass – as-deposited

(b) Silicon sample – as-deposited

(c) Cover glass – 215 ℃

(d) Silicon sample – 215 ℃

(e) Cover glass – 400 ℃

(f) Silicon sample – 400 ℃

Figure 4.1 Optical microscope images of GSSe film samples following annealing.

### 4.2.2 Scanning Electron Microscope

To further clarify the structure of the films' surfaces, samples were analyzed using Scanning Electron Microscopy (SEM). A 2.2 µm thick GSSe film on cover glass substrate with no annealing was imaged in Figure 4.2. As seen in Figure 4.1 (a), this sample showed only minor surface defects under optical microscopy.

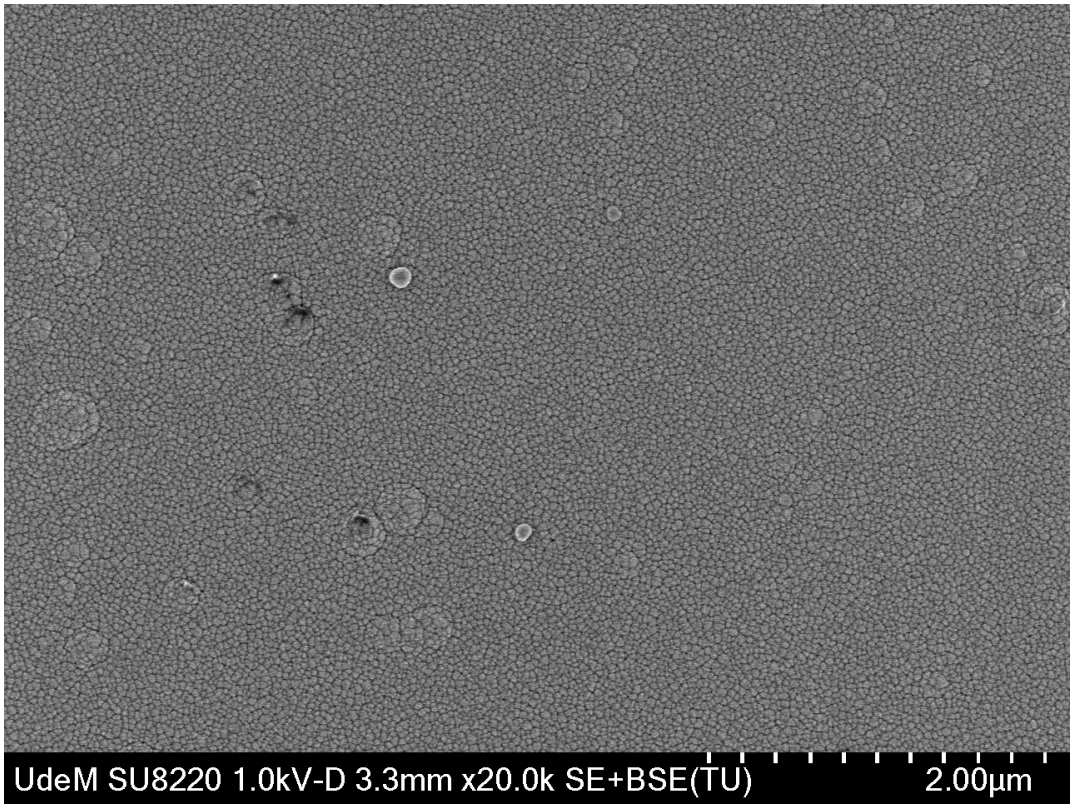


Figure 4.2 SEM micrograph of as-deposited GSSe film surface.

At a magnification of 20000×, the granular structure of the film's surface becomes visible. There are also small circular aggregations present, with diameters of the order of $\approx 100 - 400$ nm. This microstructure is likely a direct result of the sputtering parameters, especially the relatively low argon pressure of 5 mTorr, and the increased substrate temperature resulting from prolonged sputtering at a power of 75 W. The sputtering equipment used for the preparation of this sample did not have in-situ cooling or temperature measurement, so the actual temperatures reached during the deposition are not known. However, upon withdrawing the samples from the equipment, the substrate holder was noticeably warm to the touch after the 55 minutes of the process elapsed. Further studies could be conducted to measure the resulting surface roughness and optimize the sputtering parameters in consequence of this analysis.

## 4.3 Material Characterization

After visual inspection, the composition of the deposited films was studied. X-ray Photoelectron Spectroscopy (XPS) was used to determine the precise stoichiometry of the deposited films, as well as the presence of any oxidation.

### 4.3.1 Oxidation

Surface oxidation is a common occurrence for ChGs, although GSSe is considered less prone to this effect in comparison to arsenic-based chalcogenides [52]. In order to determine the nature and degree of oxidation of GSSe sputtered films, three sets of XPS measurements were performed on a total of 4 samples by Josianne Lefebvre, research associate at the Material Surface Analysis Laboratory at Polytechnique Montréal.

#### High Resolution Surface Survey

A first, as-deposited, GSSe film sample was prepared for XPS analysis by sputtering 400 nm on a silicon substrate, from Target 1. Figure 4.3 shows the fitted envelope of the entire spectrum, with some of the important peaks identified, following the first survey.

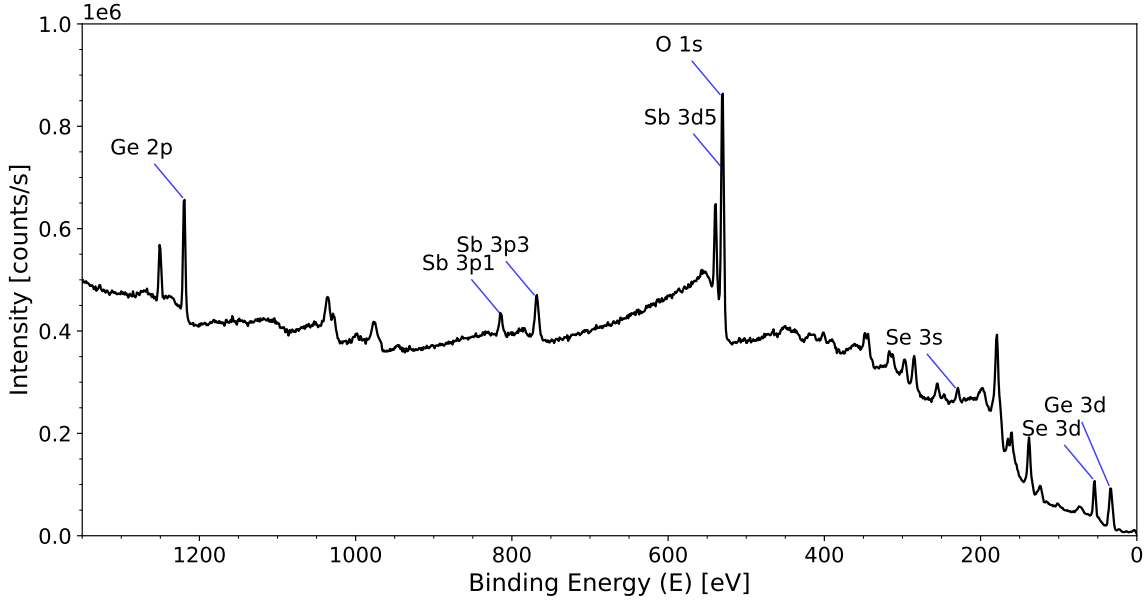


Figure 4.3 High resolution XPS survey of GSSe sample 1 surface.

A finer view of the scan around the Ge 3d region (30 eV) is presented in Figure 4.4, where

we can see the traces for each element in addition to the fitted envelope.

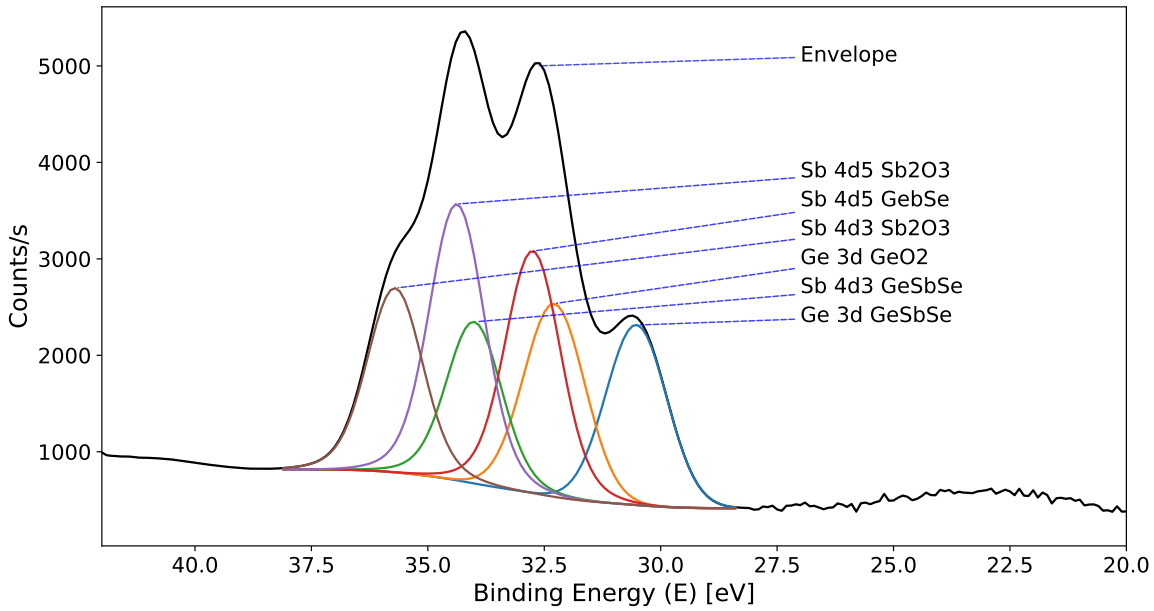


Figure 4.4 High resolution XPS survey of sample 1 around Ge 3d peak.

This initial XPS analysis revealed the presence of $GeO_2$ and $Sb_2O_3$ oxidation states, as can be seen in Figure 4.4, in addition to oxygen adsorbed on the surface of sample 1. In order to assess the stability of the sample, a second XPS survey was performed on the same sample 1 13 months later, stored in a controlled environment (20 °C, 23% relative humidity). The surface composition of sample 1 after the initial survey is summarized in Figure 4.5 (a). The composition revealed by the second survey conducted 13 months later is shown in Figure 4.5 (b).

As expected, both measurements revealed significant oxidation of the GSSe film for sample 1. The initial survey showed an oxygen proportion of about 40%, while the second survey showed about 39%. While surface oxidation should not decrease over time, this difference is quite minimal and is attributable to local differences on the film's surface, since XPS only measures a small region on the sample. The selenium proportion remained similar, while the ratio between germanium and antimony changed, with an increased relative content of antimony locally. This could be a result of the inhomogeneity of the surface. Overall, once the oxide layer has already formed on the surface of the GSSe film, the composition appears to be stable over time.

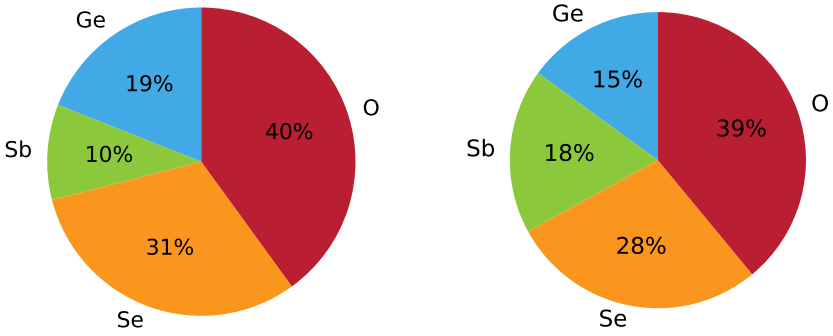


(a) Survey 1 (b) Survey 2 (13 months later)

Figure 4.5 Sample 1 (As-deposited, Target 1) surface composition over time.

A third set of XPS surveys was conducted on new samples prepared with the second sputtering target (Target 2) once it was received. These samples were prepared in the same manner as before, sputtering a 400 nm film on silicon substrates. One sample was left as-prepared (sample 2), one sample was annealed at 215 °C (sample 3), and another at 400 °C (sample 4), according to the protocol described in Chapter 4.1.2. The compositions are presented in Figure 4.6.

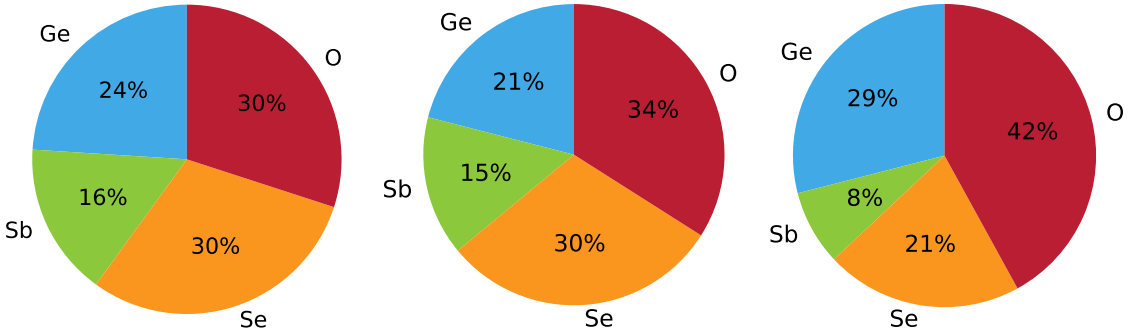


(a) As-deposited (b) Annealed 215 °C (c) Annealed 400 °C

Figure 4.6 Surface composition of samples (a) 2, (b) 3, and (c) 4 prepared with Target 2.

From Figure 4.6, we can see that samples 2, 3, and 4, prepared from Target 2, still present significant oxidation, similar to the sample 1 prepared from Target 1. Samples 2 and 3, shown in Figure 4.6 (a) and (b) respectively, have similar proportions for each element, while sample 4 in (c) has a markedly higher degree of oxidation and antimony depletion. While there is variation between the as-deposited sample and the sample annealed at 215 °C, it is on the order of that observed on sample 1 over the course of the months between the

first two surveys. This reinforces the notion that 215 °C is a sufficiently low temperature for GSSe annealing, which does not dramatically alter the film surface composition. On the other hand, it is clear that annealing at 400 °C, even under nitrogen flow, is enough to induce change in the surface composition, from which we may expect changes in optical properties as well.

### Oxidation Depth Profile

In order to determine the depth of the oxides on the surface of GSSe films, during survey 1 on sample 1, XPS spectra were collected for electron emission angles varied from $0 - 70°$. This analysis showed the relative depth of the different compounds detected, presented in Figure 4.7.

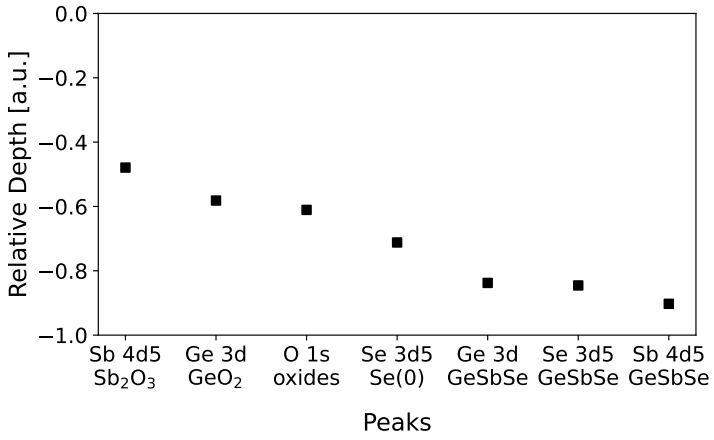


Figure 4.7 Relative depth of the detected peaks with respect to surface.

With this angle sweep, the layer thicknesses were obtained by comparing the relative intensities associated to each peak for given angles and electron attenuation lengths. The calculated overlayer thicknesses are 0.2 nm for $Sb_2O_3$, 0.3 nm for $GeO_2$, and 0.1 nm for Se compounds. This result shows that while significant oxidation occurs at the surface of GSSe films, as evidenced by the proportions in Figures 4.5 and 4.6, it remains largely superficial, with the thickest overlayer measuring 0.3 nm. This conclusion is made with the underlying assumption that the oxide layer is somewhat continuous, which should be verified using other characterization techniques such as atomic force microscopy (AFM).

While oxidation is found to be significant, the thickness of the oxide is negligible in contrast to the overall film, and is deemed unlikely to inherently influence the effective refractive index of a GSSe waveguide. Capping waveguides with a cladding such as $SiO_2$ however would

decrease the mode confinement by reducing the index contrast of the waveguide, which is undesirable for the nonlinear photonics applications considered.

### 4.3.2 Stoichiometry

The second objective of the XPS surveys was to determine the stoichiometry of the GSSe sputtered films. Since the surface scans revealed surface oxidation, XPS measurements were repeated at varied depths throughout the film. To do so, the XPS measurement was repeated at various time intervals while an argon ion beam (3 keV) was used to sputter the film until the substrate was reached.

The first sample analyzed was the same as in the previous section, sputtered from Target 1 and left as-prepared. The result of the measurement for sample 1 is presented in Figure 4.8. The data is presented according to etch time as opposed to etch depth, since the XPS measurements were not continuous, and because neither the exact film thickness (approximately 400 nm) nor the etch rate are known.

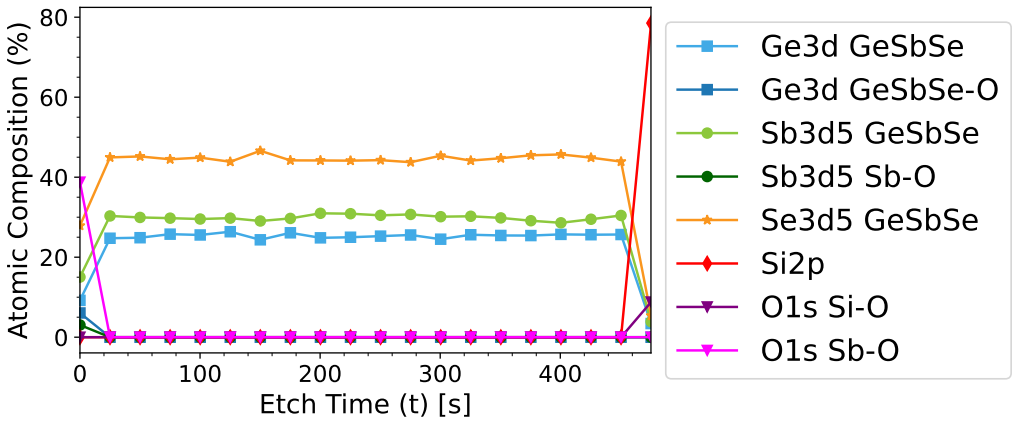


Figure 4.8 Sample 1 atomic composition throughout the film.

At $t = 0$ s, the presence of oxygen is still observed. After $t = 25$ s, the oxide compounds are no longer detected. After 450 s, the entire GSSe layer is etched through, and the silicon substrate is reached. Using the data points between $25 - 450$ s, the average composition of the deposited film is found to be $Ge_{25.4}Sb_{29.9}Se_{44.7}$. This corresponds to differences with respect to the theoretical composition of $\Delta Ge = +3.1\%$, $\Delta Sb = +7.1\%$, and $\Delta Se = -10.9\%$.

Samples 2, 3, and 4 were the same as described previously, sputtered from Target 2. Since these samples were prepared from a new sputtering target, it was important to validate the composition similarity. Additionally, samples 3 and 4 served to verify the stability of the film

composition throughout the bulk of the film after annealing. The relatively low temperature of 215 °C for sample 3 was not expected to alter film composition [58], but the 400 °C for sample 4 was shown in Figure 4.6 (c) to impact the surface composition. The depth profiles for samples 2, 3, and 4 are presented in Figures 4.9, 4.10, and 4.11 respectively.

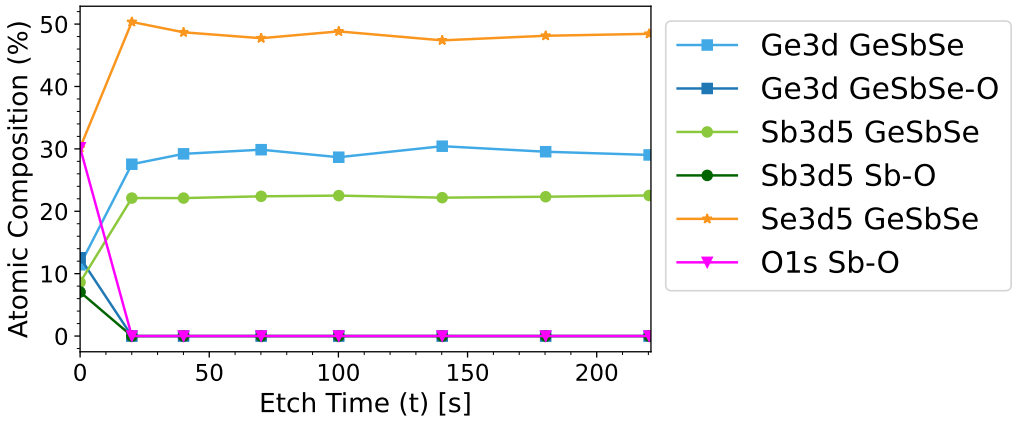


Figure 4.9 Composition of sample 2, as-deposited from Target 2.

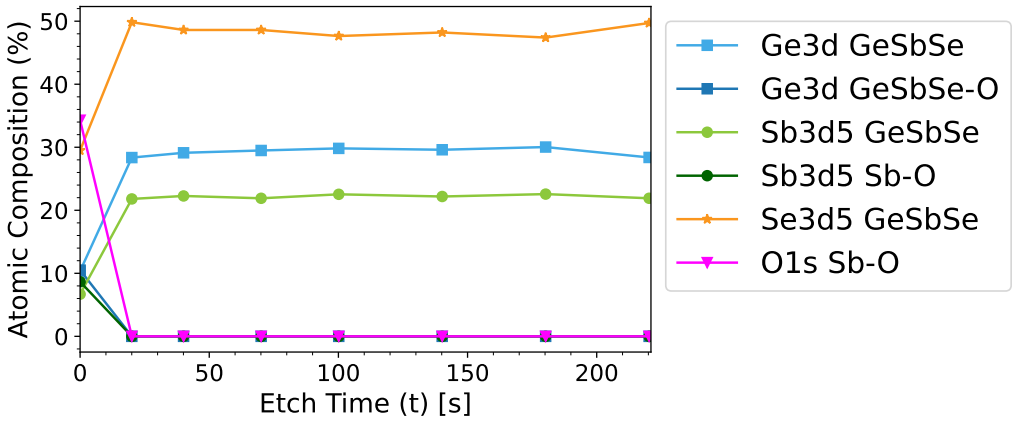


Figure 4.10 Composition of sample 3, annealed at 215 °C from Target 2.

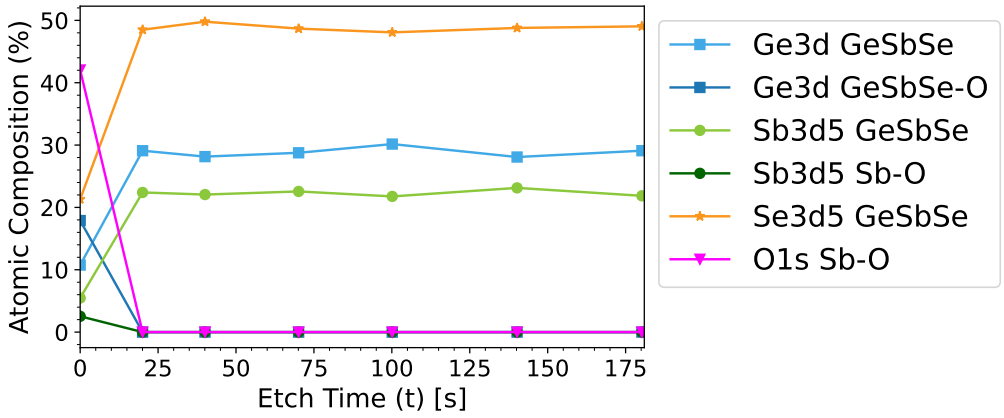


Figure 4.11 Composition of sample 4, annealed at 400 °C from Target 2.

The resulting average composition from the depth profiling for sample 2 was $Ge_{29.2}Sb_{22.3}Se_{48.5}$, $Ge_{29.3}Sb_{22.2}Se_{48.6}$ for sample 3, and $Ge_{28.9}Sb_{22.3}Se_{48.8}$ for sample 4. There is a maximum deviation of 0.4% between any one of these compositions, which indicates that neither annealing processes affected the bulk composition of the film. This confirms that the relative antimony deficit measured from the surface scan of sample 4 in Figure 4.6 (c) was a result of surface oxidation which could be precipitated by annealing, but that the integrity of the film was otherwise unaffected. However, comparing the composition of these samples sputtered from Target 2, there is a marked deviation from the film sputtered from Target 1.

### Composition Summary

The average compositions throughout each sample are summarized in Table 4.1, calculated by averaging measurement points throughout the film. The uncertainty is calculated as the highest of either the standard error across the measurement range or rounded up to 0.1% atomic, which corresponds to the limit of detection of the instrument.

Table 4.1 XPS compositions of GSSe samples.

| Sample | Target | Process | Ge | Sb | Se |
|---|---|---|---|---|---|
| 1 | 1 | As-deposited | $(25.4 \pm 0.1)\%$ | $(29.9 \pm 0.2)\%$ | $(44.7 \pm 0.2)\%$ |
| 2 | 2 | As-deposited | $(29.2 \pm 0.4)\%$ | $(22.3 \pm 0.1)\%$ | $(48.5 \pm 0.4)\%$ |
| 3 | 2 | Annealed 215 °C | $(29.3 \pm 0.3)\%$ | $(22.2 \pm 0.1)\%$ | $(48.6 \pm 0.4)\%$ |
| 4 | 2 | Annealed 400 °C | $(28.9 \pm 0.3)\%$ | $(22.3 \pm 0.2)\%$ | $(48.8 \pm 0.2)\%$ |
| | | Theoretical | 22.2 % | 22.2 % | 55.6 % |

From Table 4.1, we can see that samples 2, 3, and 4, all prepared from Target 2, have compositions within each other's calculated uncertainty ranges. This confirms that neither the low- or high-temperature annealing processes affected the bulk film composition. However, comparing the composition of sample 1, prepared from Target 1, to the subsequent films from Target 2, we find notable differences. Target 1 has a lower concentration of Ge with respect to Sb, whereas this ratio is inverted for Target 2. Additionally, Target 1 is more strongly deficient in Se, with $\Delta\mathrm{Se}_1 = -10.9\%$ versus $\Delta\mathrm{Se}_2 = -7.1\%$. For simplicity's sake, either composition may still be referred to as $Ge_2Sb_2Se_5$, but noting these differences will be a factor for drawing further conclusions and comparisons in their optical properties.

## 4.4 Linear Optical Characterization

### 4.4.1 Models

In order to determine the refractive index, absorption, and bandgap energy of thin film GSSe, we used variable angle spectroscopic ellipsometry (J. A. Woollam). Ellipsometric models appropriate for ChGs are the Cody-Lorentz (CL) model or the Tauc-Lorentz (TL) model. Chalcogenides are indirect bandgap films [68], and amorphous semiconductors, for which these models are suitable.

The Cody-Lorentz model has exponential absorption known as the Urbach tail in the sub-bandgap region, which accounts for intraband transitions. The Tauc-Lorentz model instead has no absorption in that region. The CL model ignores indirect transitions as well as Coulomb effects. The TL model simulates interband transitions and neglects intraband absorption and defect contributions [69]. Both models are considered suitable for amorphous chalcogenides, but the CL model is preferred due to its inclusion of the Urbach tail, which is significant in thin films [70]. As such, analysis of the deposited GSSe thin films will use the CL model. From this model, the film thickness (L), the real and imaginary parts of the index of refraction, and the bandgap energy, $E_g^{\mathrm{CL}}$, will be extracted. A second bandgap energy value will be calculated using Tauc's method in order to better situate the result of these measurements with respect to the literature.

Tauc's method is applicable for amorphous semiconductors with indirect bandgaps and states the following behaviour of photon energy:

$$\sqrt{\alpha(E)\ h\nu} \propto h\nu - E_g^{\mathrm{opt}}\ , \tag{4.1}$$

where $\alpha(E)$ is the absorption coefficient, $E = h\nu$ is the photon energy, and $E_g^{\mathrm{opt}}$ is the

bandgap determined by this method. By plotting $\sqrt{\alpha(E)\ h\nu}$ versus photon energy, the bandgap corresponds to the extrapolated x-intercept of the linear portion of the graph [71].

### 4.4.2 Measurements

For each measurement, reflection spectra were collected at angles of incidence of 45, 55, 65, and 75° and fitted simultaneously using CompleteEASE software. The spectra were fitted by minimizing mean square error (MSE).

The first film to analyze was the as-deposited sample sputtered from Target 1 GSSe. To do so, samples were prepared by sputtering approximately 2 µm of GSSe on 150 µm borosilicate cover glass slides using the 75 W sputtering recipe. The blank cover glass substrate was also fitted using a simple Cauchy model to confirm the refractive index information. The result of the ellipsometric fit was a refractive index of 2.92 and negligible absorption ($\kappa \leq 10^{-3}$) at a wavelength of 1550 nm. The film thickness was confirmed to be around 2.3 µm. The bandgap energy extracted from the CL model, $E_g^{CL}$, was $1.30 \pm 0.08$ eV. The dispersion data for the GSSe film is presented in Figure 4.12.

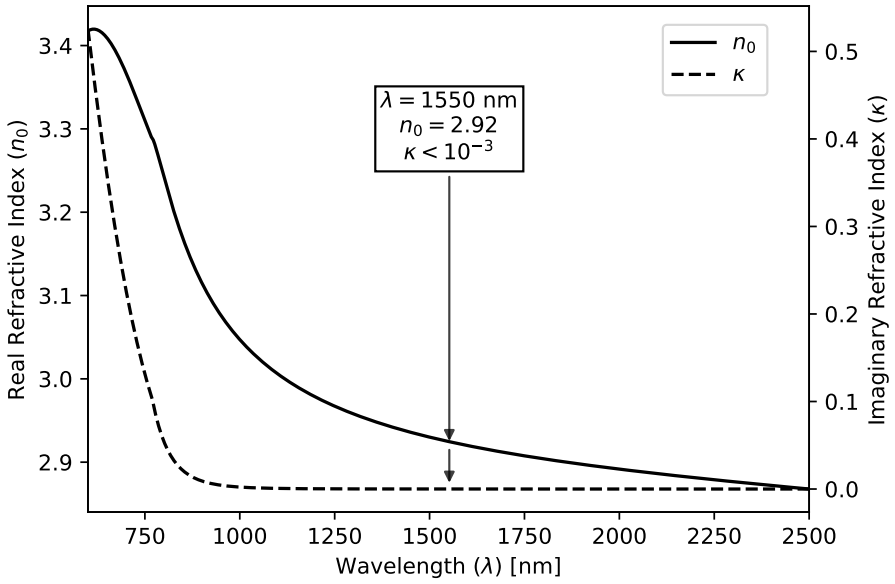


Figure 4.12 Fitted refractive index of GSSe film from Target 1.

Using the absorption data fitted from the ellipsometric model, the optical bandgap as determined by the Tauc method, $E_g^{opt}$, was found to be 1.38 eV, which is at the upper edge of the model's uncertainty for the CL bandgap. The Tauc plot used to extract the bandgap is presented in Figure 4.13, as an example.

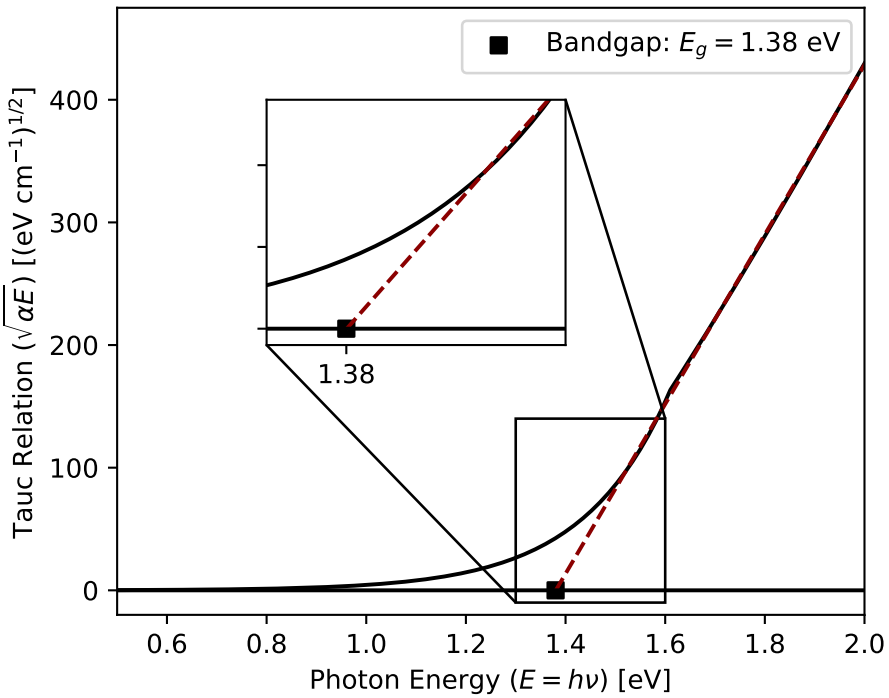


Figure 4.13 Tauc plot for as-deposited film from Target 1.

Films deposited with Target 2 were also analyzed. More samples were prepared by the same process, sputtering approximately 2 µm of GSSe on the same type of cover glass substrates. One sample was left as-deposited, one was annealed at 215 °C, and another at 400 °C. Following the same process as described for the first sample, each film was measured using ellipsometry and fitted with the CL model, then using the Tauc plot method.

### 4.4.3 Discussion

The parameters extracted are summarized in Table 4.2 below. The dispersion curves and Tauc plots for each sample are available in Appendix A.

Table 4.2 Ellipsometric determination of linear optical properties at 1550 nm.

| Sample | Target | Thermal | L [µm] | n | $\kappa$ | $E_g^{CL}$ [eV] | $E_g^{opt}$ [eV] |
|---|---|---|---|---|---|---|---|
| 1 | 1 | As-dep. | 2.34 | 2.92 | $< 10^{-3}$ | $1.30 \pm 0.08$ | 1.38 |
| 2 | 2 | As-dep. | 2.29 | 2.93 | $< 10^{-3}$ | $1.27 \pm 0.04$ | 1.35 |
| 3 | 2 | 215 °C | 2.25 | 2.93 | $< 10^{-3}$ | $1.3 \pm 0.1$ | 1.37 |
| 4 | 2 | 400 °C | 2.17 | 3.01 | 0.05 | $1.263 \pm 0.006$ | 1.37 |

From Table 4.2, we can see that using either definition, the as-deposited film from Target 1 has a slightly higher bandgap energy and a very slightly lower refractive index. They are both within each other's uncertainty ranges however. In terms of the influence of annealing, the 215 °C process seems to have slightly increased the bandgap energy, which is in accordance to expectations. For the 400 °C process, the refractive index appears to have increased along with the losses at 1550 nm, which points to crystallization of the film. The CL model may no longer be appropriate for this film, and no nonlinear optical analysis will be conducted as a result of the significant losses observed.

Literature shows $E_g^{opt}$ for thermally evaporated $Ge_2Sb_2Se_5$ films of approximately $1.4-1.6$ eV [72]. The values extracted in this work are on the lower end of this range, which could be the result of differences from the deposition processes. The implications of this lower bandgap energy are that higher losses might be expected at a wavelength of 1550 nm than might be elsewhere measured. Previous work on GSSe family chalcogenides has shown that the annealing of sputtered films can cause bleaching, resulting in an increase of the bandgap energy. For example, $Ge_{24}Sb_{11}Se_{66}$ had an increase of $E_g^{CL}$ from 1.87 eV to 1.96 eV, and a slight RI decrease of 2.55 to 2.54 [73]. In comparison with these results, we see a similar trend from sample 2 to sample 3, i.e. comparing the as-deposited film with annealing at 215 °C, where the bandgap energy increased slightly, but the refractive index was essentially the same. However, when looking at sample 4, annealed at 400 °C, we see a marked increase in refractive index and a similar bandgap energy. This suggests there may be an inconsistency either with the ellipsometric model itself, or that the surface of the analyzed sample may have been too rough to provide a consistent measurement, leading to error in interpretation of the data.

In summary, the main purpose of this analysis was to determine the linear optical coefficients in GSSe films so that they may be used for nonlinear device fabrication. As such, despite some uncertainty remaining on the exact parameters for the sample annealed at 400 °C, the first part of sub-objective 1, i.e. the determination of the linear optical coefficients of GSSe, can be considered completed, since the high-temperature annealed film is not a candidate for the fabrication of such devices, and merely served as a contrasting sample in this analysis.

## 4.5 Nonlinear Optical Characterization

### 4.5.1 Z-scan Theory

In order to determine the nonlinear optical coefficients of GSSe in thin film form, the z-scan technique [27] was employed. This method involves measuring the transmission of a Gaussian

beam through a thin sample, which is translated through the focus of the beam (position $z = 0,\ z_0$).

To determine the two-photon absorption ($\beta_{\text{2PA}}$) of the sample, this measurement is first done without an aperture before the detector, and is referred to as the "open aperture" trace. If the sample exhibits 2PA, as it nears the beam's focus, the increased intensity will result in increased absorption. This is reflected as a dip in the transmission at the detector around $z_0$.

If an aperture is included before the detector, the technique becomes sensitive to nonlinear refraction, which induces a self-lensing effect in the sample, as explained in Chapter 2.2.1. The aperture, which may be physically or digitally integrated, enables the measurement of $n_2$, since the phase shift induced by the sample is much stronger at the centre of the Gaussian beam. This "closed aperture" trace is used to extract the magnitude and sign of a material's $n_2$.

In the case of a positive $n_2$, when the sample approaches the focus from $z < z_0$ (before the focus), the increased intensity leads to self-lensing which shifts the beam focus closer to the sample, thus increasing divergence in the far field near the detector. Once the sample transits past the focus to $z > z_0$, the continued self-focusing effect results in increased intensity at the detector. Together, this results in a valley and peak in the transmission at the detector. For a negative $n_2$, the self-defocusing would result in a closed aperture trace with a peak followed by a valley [74].

Gu et al. developed a model for extracting the phase shifts from z-scans with femtosecond pulses, which allows $n_2$ and $\beta_{\text{2PA}}$ to be calculated [75]. For pulses with a hyperbolic secant squared temporal profile, the open aperture trace transmission $T$ at a normalized position with respect to the Rayleigh range $z_{\text{R}} = kw_0^2/2$, defined as $x = z/z_{\text{R}}$, should follow:

$$T(x) = \sum_{m=0}^{\infty} \frac{(-q_0)^m\ 2^m\ m!}{(x^2+1)^m(m+1)(2m+1)!!}\ , \tag{4.2}$$

where $w_0$ is the beam waist radius, and $q_0$ is the peak "imaginary" phase shift induced by the sample's nonlinear absorption, such that

$$q_0 = \beta_{\text{2PA}}\ I_0\ (1-R)\ L_{\text{eff}}\ , \tag{4.3}$$

where $I_0$ is the incident intensity at the sample, $R = ((1-n_0)/(n_0-1))^2$ is the Fresnel reflectivity at the air interface, and $L_{\text{eff}} = (1-\exp(-\alpha L))/\alpha$ is the effective sample length scaled by the absorption coefficient $\alpha$. Note that $L_{\text{eff}}$ reduces to $L$, the total sample length, in the case of negligible absorption.

For higher order multi-photon absorption, such as three-photon absorption, we use a similar model described by Chen et al. [76]:

$$T(x) = \sum_{m=0}^{\infty} \frac{(-p_0)^m}{(2m+1)!(2m+1)^{1/2}(1+x^2)^m} \ , \tag{4.4}$$

with

$$p_0 = 2 \ \beta_{3\mathrm{PA}} \ I_0^2 \ (1-R)^2 \ L'_{\mathrm{eff}} \ , \tag{4.5}$$

where $\beta_{3\mathrm{PA}}$ is the three-photon absorption coefficient, and $L'_{\mathrm{eff}} = (1 - \exp(-2\alpha L))/(2\alpha)$ is the effective length in the case of 3PA. The original paper does not include the $(1-R)^2$ factor, but it was included here for consistency between intensity definitions with Gu's model.

Finally, the normalized closed aperture trace's transmission using Gu's model should follow [75]:

$$\begin{aligned} T(x) = 1 &+ \frac{2}{3}\frac{4x\Delta\phi_0 - (x^2+3)q_0}{(x^2+1)(x^2+9)} \\ &+ \frac{8}{15}\frac{4\Delta\phi_0^2(3x^2-5) + q_0^2(x^4+17x^2+40) - 8\Delta\phi_0 q_0 x(x^2+9)}{(x^2+1)^2(x^2+9)(x^2+25)} \ , \end{aligned} \tag{4.6}$$

with $\Delta\phi_0$ being the peak "real" phase shift induced by the sample's nonlinear refraction, such that

$$\Delta\phi_0 = \frac{2\pi}{\lambda} \ n_2 \ I_0 \ (1-R) \ L_{\mathrm{eff}} \ . \tag{4.7}$$

These equations are valid in the case of "small nonlinearity", i.e. phase shifts $\Delta\phi_0$, $q_0$, and $p_0 < 1$ rad, and for a sample thickness $L$ such that $L \ll z_{\mathrm{R}}$, where $z_{\mathrm{R}} = \frac{k\omega_0^2}{2}$ is the Rayleigh range of the Gaussian beam.

### 4.5.2 Experiment

#### Blank Substrate Measurement

Since the goal of these experiments was to measure the nonlinear properties of GSSe sputtered films, samples had to be prepared using suitable substrates. These consisted of borosilicate cover glass slides with a thickness of about 150 µm, since this material is expected to possess much weaker $n_2$ and virtually no 2PA in comparison to the GSSe under study. The substrate thickness was also minimized to reduce the proportion contributed to the overall measured transmission, since the phase shift is a product of $n_2$ and $L$. In order to ascertain the suitability of these substrates, z-scan measurements were performed using the same setup as

for the film samples. This consisted of a 1550 nm laser with a repetition rate of 100 kHz, a pulse duration of 172 fs, and a beam waist radius at focus of 14 µm. The transmission was measured with an InGaAs detector with no physical aperture in the beam path between the sample and the detector. For closed aperture traces, the aperture was digitally integrated. A more detailed description of the processing is provided in Appendix B. The measurements and processing were carried out with the help of Pierre-Luc Thériault, Abhay Anand, and Arnaud Petit at Polytechnique Montréal's Light-Matter Group. A schematic of the z-scan setup is presented in Figure 4.14.

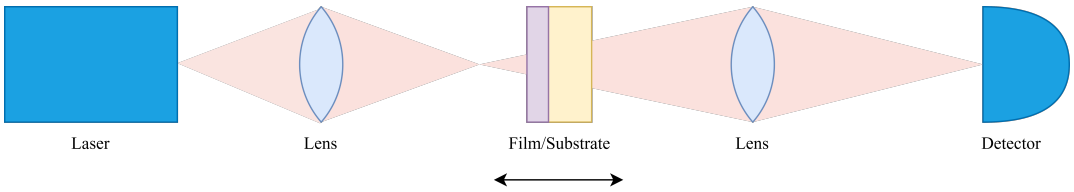


Figure 4.14 Schematic of the z-scan setup.

The laser intensity was gradually increased until any change in the transmission was observable. Only at an incident intensity at the sample of 279 GW/cm$^2$ was a response measured in the closed aperture trace, corresponding to the onset of nonlinear refraction. This intensity far exceeds the range used for the GSSe film samples, and no nonlinear absorption was observed. As such, the laser intensity was not further increased since no measurements would be performed in this range. The normalized closed aperture trace is presented in Figure 4.15.

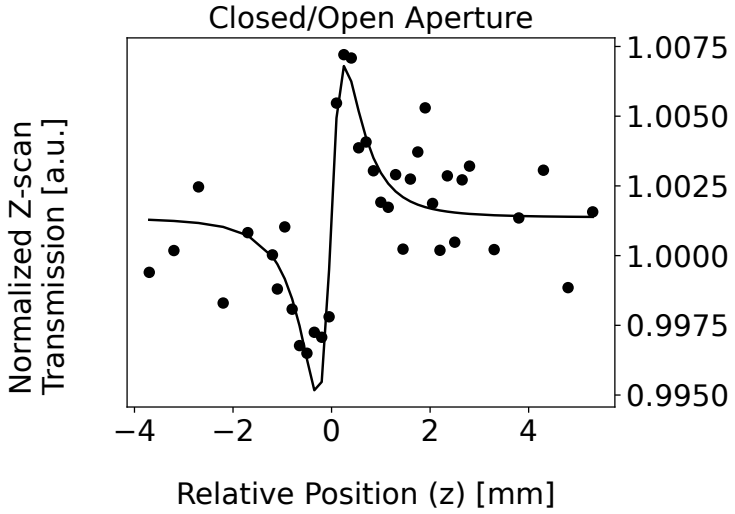


Figure 4.15 Normalized closed aperture trace for substrate z-scan at $I_0 = 279$ GW/cm$^2$.

From Figure 4.15, using Equations (4.6) and (4.7), the real phase shift $\Delta\phi_0$ was extracted as 43.6 mrad and the nonlinear index of the substrate was extracted as $n_2 \approx 2.57 \times 10^{-20}$ m$^2$/W. This is in range with other silica-based glasses [7], and several orders of magnitude below the expected value for GSSe, which will be confirmed subsequently. With this, the calculations for GSSe films will ignore the substrate contributions.

### Target 1 As-Deposited Film Measurement (Sample 1)

The first thin film sample analyzed was the exact sample 1 described in Table 4.2, with a GSSe film thickness of 2.3 µm, as-deposited from Target 1. Using the same z-scan setup described previously, but with a beam waist radius at focus of 12 µm, measurements were performed at different locations on the sample, with incident beam intensities ranging between $I_0 = 15.8 - 35.2$ GW/cm$^2$. Example closed and open aperture traces are presented in Figure 4.16.

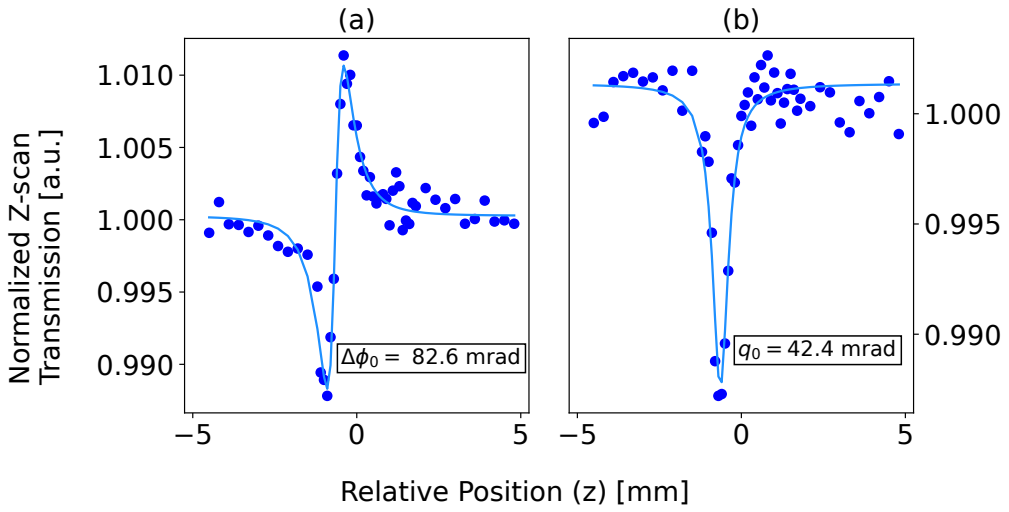


Figure 4.16 Z-scan (a) closed and (b) open aperture traces for sample 1 at $I_0 = 27.7$ GW/cm$^2$.

From the fitted traces in Figure 4.16 (a) and (b), real and imaginary phase shifts of $\Delta\phi_0 = 82.6$ mrad and $q_0 = 42.4$ mrad are calculated. The fitting and phase shift extraction process is repeated for each scan point, and the results are summarized in Figure 4.17, with each different measurement location on the sample illustrated with different colours. The shaded area in the figure serves to illustrate the spread of the data points, showing the minimum and maximum slopes based off the extracted values.

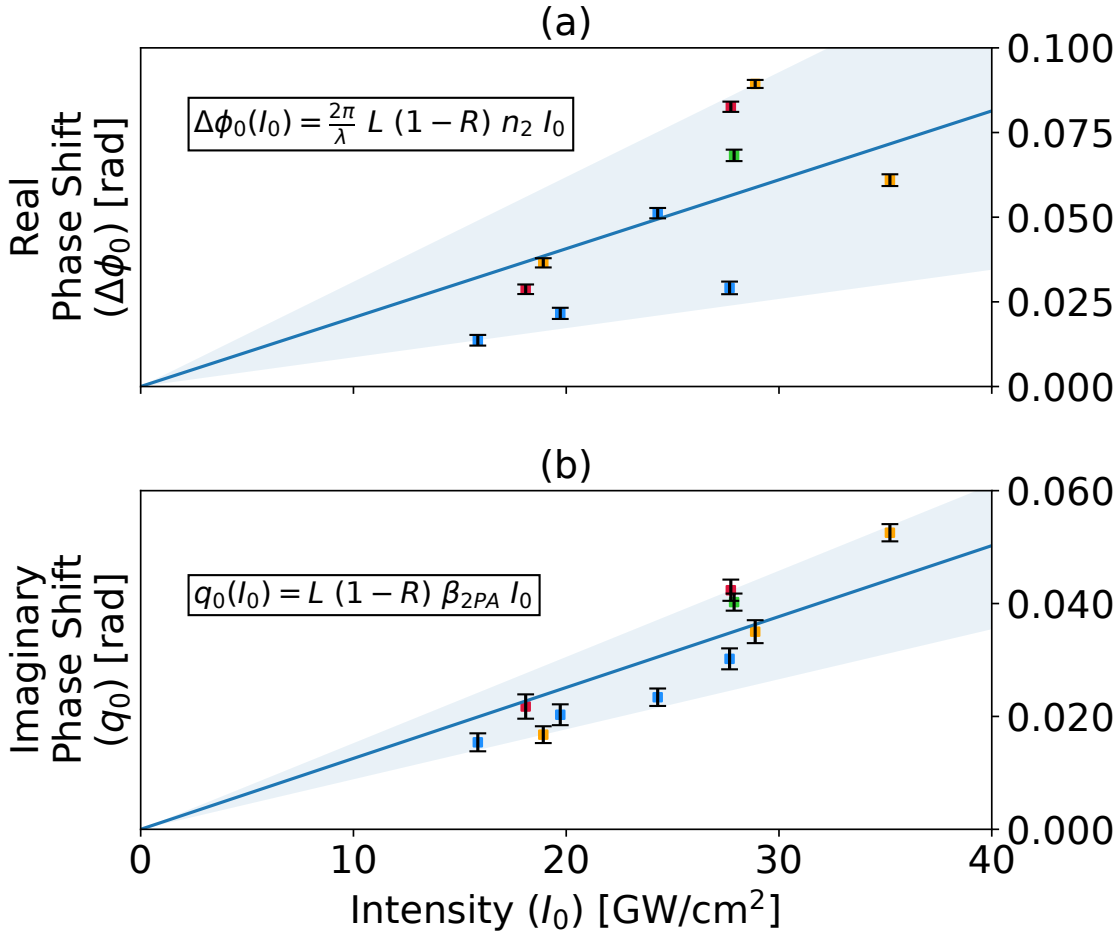


Figure 4.17 (a) $n_2$ and (b) $\beta_{2PA}$ extraction for sample 1 z-scan. The data points are coloured to indicate different measurement locations on the same sample. The shaded area shows the spread of the data. Error bars represent the standard error calculated from the numerical fit of the model.

From the data points in Figure 4.17, linear regressions are fitted using equations (4.7) and (4.3) to extract $n_2 = (2.9 \pm 0.3) \times 10^{-17}$ m$^2$/W and $\beta_{2\text{PA}} = (7.1 \pm 0.4) \times 10^{-11}$ m/W. The uncertainty on the values comes from the standard error on the slope fit.

### Target 2 As-Deposited Film Measurement (Sample 2)

A z-scan measurement was performed on the as-deposited GSSe sample prepared from Target 2, corresponding to sample 2 in Table 4.2. The beam waist radius at focus was 14 µm, and the intensity ranged from $24.1 - 53.8$ GW/cm$^2$. Figure 4.18 presents closed and open aperture traces from this set of measurements as representative data. As before, the extracted phase shifts are plotted with respect to intensity and presented in Figure 4.19.

By performing linear regressions on Figure 4.19, we find $n_2 = (2.8 \pm 0.2) \times 10^{-17}$ m$^2$/W and $\beta_{2\text{PA}} = (7.2 \pm 0.6) \times 10^{-11}$ m/W, with uncertainties resulting from the standard error on the fits.

### Target 2 Annealed Film Measurement (Sample 3)

In order to determine the effects of annealing, a z-scan measurement was performed on sample 3 from Table 4.2, i.e. sputtered from Target 2 and annealed at 215 °C. No z-scan was performed on the film annealed at 400 °C (sample 4), since the surface was too rough and inhomogeneous to allow for an adequate signal to be measured. The beam waist radius at focus was again 14 µm, and all other parameters remained the same as described previously. Figure 4.20 presents closed and open aperture traces from this set of measurements as representative data. The extracted phase shifts are plotted with respect to intensity and presented in Figure 4.21.

From the linear regressions, we find $n_2 = (0.81 \pm 0.04) \times 10^{-17}$ m$^2$/W and $\beta_{2\text{PA}} = (1.89 \pm 0.06) \times 10^{-11}$ m/W for sample 3.

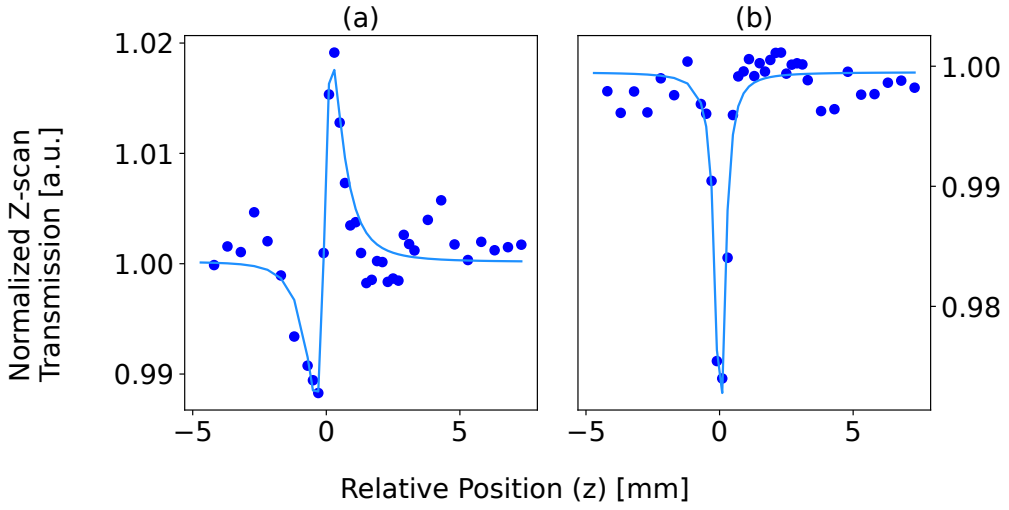


Figure 4.18 (a) Normalized closed and (b) open aperture traces on sample 2 at $I_0 = 49.8$ GW/cm$^2$.

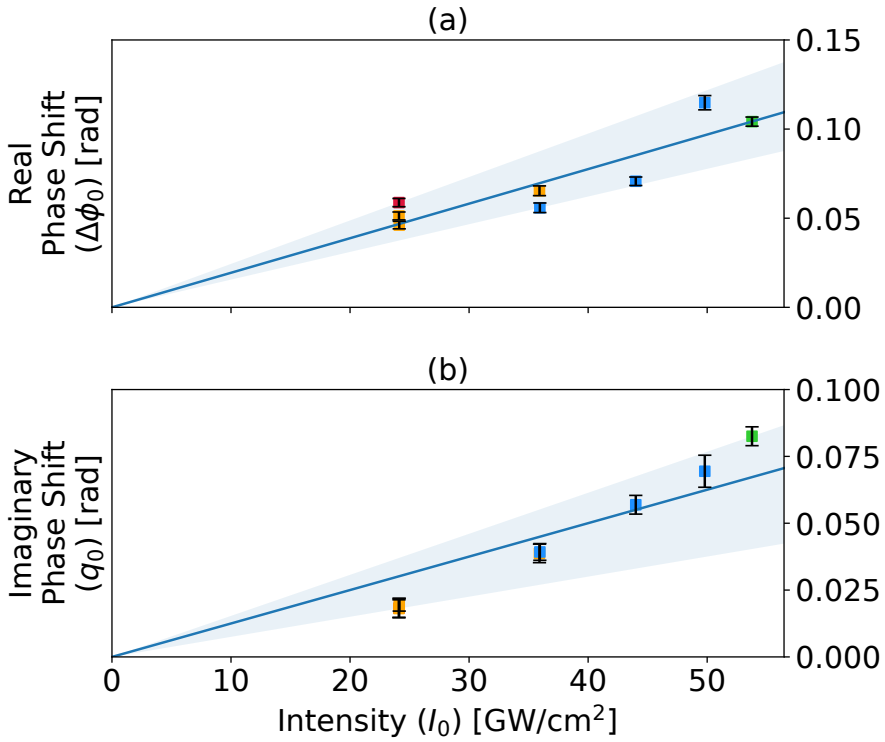


Figure 4.19 (a) $n_2$ and (b) $\beta_{2PA}$ extraction for sample 2. Colours represent different measurement locations on the sample; shaded area shows spread of data points. Error bars correspond to standard error.

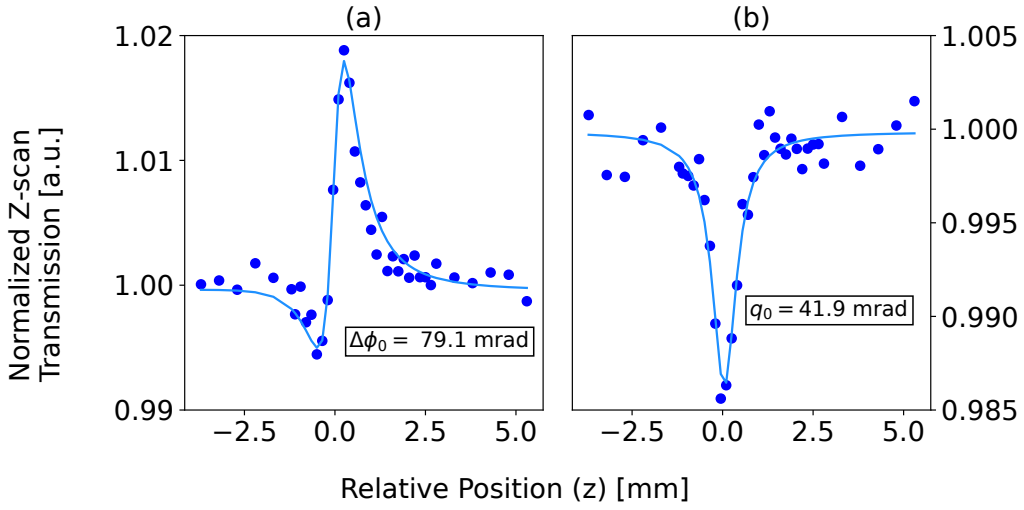


Figure 4.20 (a) Normalized closed and (b) open aperture traces on sample 3 at $I_0 = 124.5$ GW/cm$^2$.

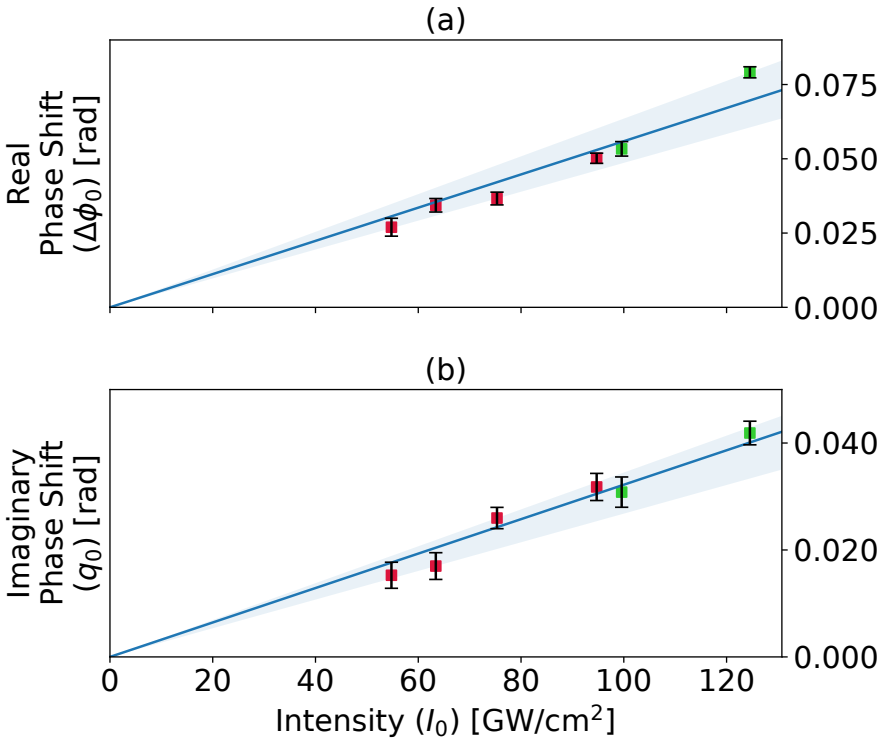


Figure 4.21 (a) $n_2$ and (b) $\beta_{2PA}$ extraction for sample 3. Colours represent different measurement locations on the sample; shaded area shows spread of data points. Error bars correspond to standard error.

**Thermal Effects**

The z-scan technique can be sensitive to thermal effects which can lead to mistaken determinations of the nonlinear coefficients. Thermal effects can be induced in the sample when long pulses (> 200 ps) are used, or when the repetition rate is elevated, leading to cumulative effects in the sample. While the former is not an issue since the pulses were much shorter (172 fs), we must investigate the second scenario. The repetition rate $f_{\text{rep}}$ can lead to cumulative lensing effects when [77, 78]:

$$\frac{1}{f_{\text{rep}}} < t_c = \frac{w_0^2}{4D} \ , \tag{4.8}$$

where $t_c$ is the characteristic thermal diffusion time, dictated by the beam's waist diameter 2 $w_0$, and the thermal diffusion coefficient $D = K/(\rho C)$ related to the thermal conductivity $K$, density $\rho$, and $C$, the specific heat capacity of the sample. For the GSSe z-scans, 2 $w_0 \approx$ 28 µm, $K \approx 0.25$ W/(m·K), $\rho \approx 4.66$ g/cm$^3$, and $C \approx 0.33$ J/(g·K) [79]. This yields $1/t_c \sim 10^3$ s$^{-1}$, which is well below the 100 kHz repetition rate used.

In the closed aperture traces, thermal lensing would manifest as an increase in the apparent $n_2$ from an increased peak-valley amplitude in the transmission ($\Delta T_{\text{p-v}}$). This amplitude should remain constant for a given peak laser power, but will be seen as increasing linearly with average power with no regard to peak power in the event of thermal lensing [78].

To validate the absence of thermal lensing in the prior z-scan measurements, another set of experiments was performed on samples 2 and 3. The same general setup was used as described previously. The parameters remained a 1550 nm wavelength, 172 fs pulse duration, and repetition rate was varied between 1 kHz, 10 kHz, and 100 kHz. The beam waist radius at focus was 14 µm. Note that this measurement was performed at a separate date from the previous ones on samples 2 and 3, and that the calibration shows a discrepancy with the previous data. This may affect the exact numerical values extracted from these curves, which is not an issue, given that the intent of these scans was simply to identify whether a trend was observed with repetition rate. For each sample, at a given nominal peak laser power, the normalized open and closed aperture traces are presented in Figures 4.22 (a) and (b).

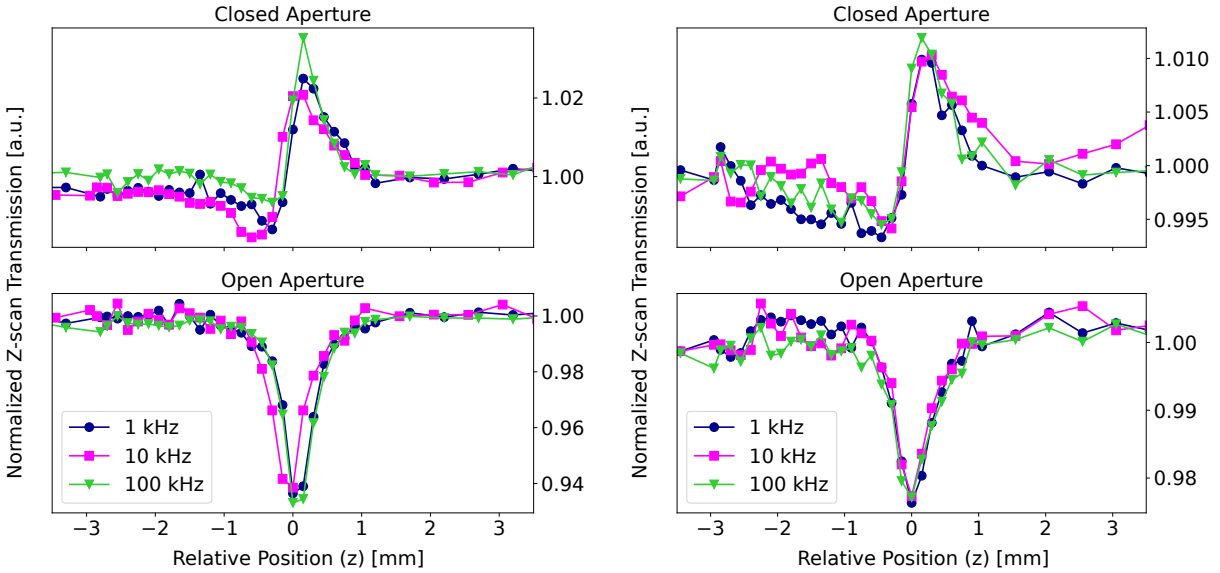


(a) As-deposited, $P_{\mathrm{p}} = 150$ kW

(b) Annealed, $P_{\mathrm{p}} = 219$ kW

Figure 4.22 Normalized closed and open aperture traces at varied repetition rates with fixed peak powers for (a) sample 2 and (b) sample 3.

From Figures 4.22 (a) and (b), we can see that there is little distinction between the curves corresponding to different repetition rates in the raw data. Next, from the fitted models of these traces, the peak-valley transmission $\Delta T_{\mathrm{p-v}}$ is extracted from the closed aperture traces and plotted with respect to repetition rate for simplicity of visualization. We recall the relationship between peak power and average power for a laser,

$$P_{\mathrm{avg}} = P_{\mathrm{p}}\ \Delta t\ f_{\mathrm{rep}}\ , \tag{4.9}$$

with $\Delta t = 172$ fs corresponding to the laser's pulse duration, for a fixed peak power of $P_{\mathrm{p}} = 150$ kW for the as-deposited sample and $P_{\mathrm{p}} = 219$ kW for the annealed sample. As pulse duration and peak power are fixed, the average power varies proportionally with the repetition rate. Therefore, if thermal lensing is obscuring the z-scan nonlinearity measurement, we expect a linearly increasing $\Delta T_{\mathrm{p-v}}$ with repetition rate. The result is presented in Figure 4.23.

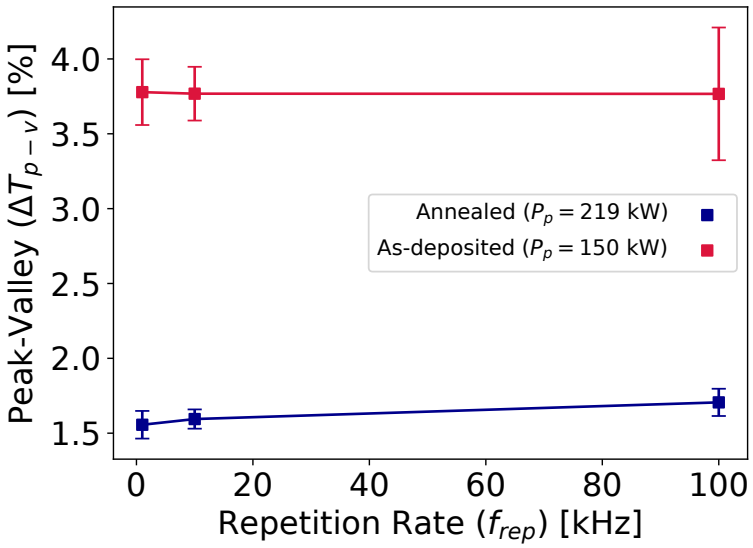


Figure 4.23 Effect of repetition rate on amplitude of peak-valley transmission for both samples.

### 4.5.3 Z-scan Discussion

The extracted nonlinear coefficients for samples 1, 2, and 3 are summarized in Table 4.3.

Table 4.3 Nonlinear optical properties at 1550 nm measured by z-scan.

| Sample | Target | Thermal | $n_2$ [$\times 10^{-17}$ m$^2$/W] | $\beta_{2PA}$ [$\times 10^{-11}$ m/W] |
|---|---|---|---|---|
| 1 | 1 | As-dep. | $2.9 \pm 0.3$ | $7.1 \pm 0.4$ |
| 2 | 2 | As-dep. | $2.8 \pm 0.2$ | $7.2 \pm 0.6$ |
| 3 | 2 | 215 °C | $0.81 \pm 0.04$ | $1.89 \pm 0.06$ |

**Index Comparison**

Comparing the values presented in Table 4.3 with the substrate results, it is clear that at these intensity ranges, i.e. approximately one order of magnitude below that necessary to elicit a response in the blank substrate, the primary contributor to nonlinear refraction observed must be due to the film itself. Both as-deposited samples, despite being prepared from targets with different compositions, have appreciably the same $n_2$ values, within the uncertainty range. However, the annealed sample has a markedly lower $n_2$, about 3.5× smaller than either as-deposited sample.

Comparing these $n_2$ values to other measurements for GSSe-family chalcogenides, we find higher results than reported in literature for the as-deposited films, and comparable results for the annealed sample. Depending on the precise composition, as well as the measurement method, $n_2$ values from $0.53 \times 10^{-17}$ m$^2$/W [49] to $2.03 \times 10^{-17}$ m$^2$/W [1] have been reported. These values are typically measured by z-scan on thick glass samples ($\approx$ 1 mm thick), or by direct transmission analysis (DTA), whereas the measurements performed in this work are for sputtered thin films. As previously discussed, sputtering may influence the structure and optical properties of a material. As a result, the $n_2$ values calculated from our thin film z-scan may better correspond to the actual response which would be observed in a fabricated waveguide or resonator on chip, as opposed to the bulk values found in literature.

Situating these values more globally among other ChGs and nonlinear materials, the as-deposited samples in particular yield an elevated $n_2$ value. Miller's relation suggests an increase in $n_2$ with increased $n_0$, and can be written as [5]:

$$n_2 = C\frac{(n_0^2 - 1)^4}{n_0^2}\ , \tag{4.10}$$

where $C$ is a constant often fitted empirically. To better visualize the results of this work, the obtained $n_2$ values are plotted against $n_0$ along with other materials from literature in Figure 4.24.

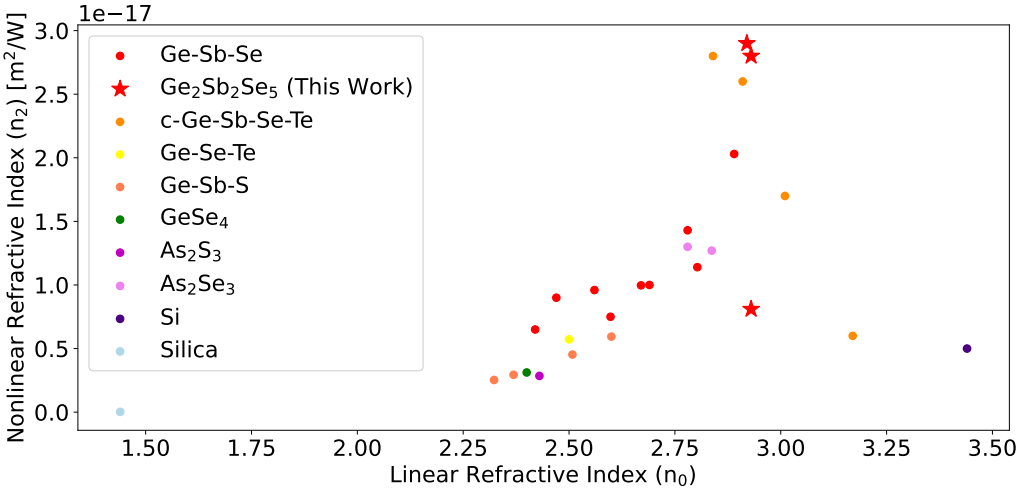


Figure 4.24 Comparison of $n_0$ and $n_2$ values [1–7].

From Figure 4.24, we can see that the extracted values seem to be in line with the overall trend of Equation 4.10 and other materials. The elevated $n_2$ in the case of the GSSe samples reported in this work is associated with a correspondingly elevated $n_0$. This result indicates

that GSSe films may indeed be promising candidates for on-chip nonlinear photonics devices, but must be weighed in comparison with their absorption.

Another relevant finding is that typically, as the bandgap energy decreases, the linear and nonlinear refractive index of a material increase [56]. Considering the $E_g$ values determined in Chapter 4.4, which were lower than expected, an elevated $n_2$ is also expected.

Finally, as discussed in Chapter 3, the MCN of a material is correlated to its optical properties. For the theoretical composition of $Ge_2Sb_2Se_5$, the MCN is 2.67. However, using the compositions which were determined by XPS in Chapter 4.3, we find MCN $\approx$ 2.8. According to the observations in [49], this puts the glass films in the "stressed-rigid" region (MCN $>$ 2.67), where elevated $n_2$ is observed. This further confirms the result from a material structure perspective.

### Multi-Photon Absorption

In terms of 2PA, as was the case for $n_2$, both as-deposited samples are found to have about the same value of $\beta_{2PA} \approx 7.2$ cm/GW. However, the annealed sample is again found to have significantly lower absorption, by a factor of around 3.8$\times$ in comparison. This is in good agreement with the idea that annealing should relax the film and increase the bandgap, which was observed in the linear experiments summarized in Table 4.2.

A commonly used figure of merit for nonlinear optical processing is:

$$\text{FOM} = \frac{n_2}{\beta_{2PA}\lambda} \ , \tag{4.11}$$

by which we can compare the overall performance of various materials. For the three measured samples, we find respective FOM values of 0.26, 0.25, and 0.28. We can see that despite annealing undesirably reducing the nonlinear index, the corresponding decrease in absorption is enough to compensate and even slightly improve the overall merit of the material.

Situating the measured values with the literature, all three samples again show elevated $\beta_{2PA}$, which for other GSSe ChGs, ranges from negligible to around $0.84 \times 10^{-11}$ m/W [1, 49]. In this regard, the samples perform unexpectedly poorly. However, considering the FOM, we find values on the order of silicon which has a FOM $\approx$ 0.3 at 1550 nm [80]. Unfortunately, many materials cannot be compared this way due to the difficulty in measuring low values of 2PA, which results in reports of "negligible" 2PA for many ChGs.

It is worth noting that once again, these types of measurements are typically done on bulk glass samples, which means that lower incident intensity is required to elicit a measurable

response, given the much larger optical path length through the sample ($\approx 2$ µm in film vs. $1-2$ mm in bulk). The necessary use of higher intensity in this experiment could mean that we were able to measure absorption in a regime which was not excited in other, lower-powered experiments.

Additionally, 2PA is expected to become observable at wavelengths corresponding to photon energies $h\nu/E_\mathrm{g} \geq 0.5$ [1,5]. Even when accounting for the varying definitions of $E_\mathrm{g}$, especially in the case of amorphous semiconductors such as GSSe, most reported values are higher than those calculated for samples $1-3$. In the case of this experiment, $E_\mathrm{g}/2 \approx 0.65$ eV $\approx 1910$ nm, whereas many articles cite $E_\mathrm{g} \approx 1.6$ eV or higher [1], for which $E_\mathrm{g}/2 \approx 1550$ nm. As such, the observation of 2PA in the case of this work's samples is consistent with the expected onset, albeit slightly elevated, while other GSSe measurements would show negligible 2PA at 1550 nm with higher $E_\mathrm{g}$. However, at mid-infrared wavelengths, GSSe might show better performance in this form, which could be validated with z-scans at longer wavelengths.

More generally, the thresholds for $N$-photon absorption can be described as following [5]

$$h\nu \geq E_\mathrm{g}/N \ , \tag{4.12}$$

with two- and three-photon absorption ($N = 2, 3$) expected at $h\nu < E_\mathrm{g} < 2h\nu$ and $2h\nu < E_\mathrm{g} < 3h\nu$. Following this relation, 2PA is indeed expected for our measured $E_\mathrm{g}$. However, considering the large majority of literature reports for GSSe $E_\mathrm{g}$ are closer to or greater than 1.6 eV, 3PA may be within reach.

Taking all these factors into account with the fact that two- and three-photon absorption have been known to occur simultaneously in ChG films [81], the possibility of the observed transmission dips in the open aperture spectra being attributed to 3PA was considered. The spectra were retroactively fitted with Equation (4.4) to extract phase shifts and subsequently, $\beta_\mathrm{3PA}$ from Equation (4.5). An example of this fit for each sample is presented in Figure 4.25, in conjunction with the original 2PA model fit and the respective $R^2$ values for each model.

Overall, the 3PA model fits the open aperture traces well, but to a similar degree as the 2PA model. To further investigate, the extracted 3PA phase shifts $p_0$ are plotted against the intensities in Figure 4.26. The data points are fitted according to Equation (4.5).

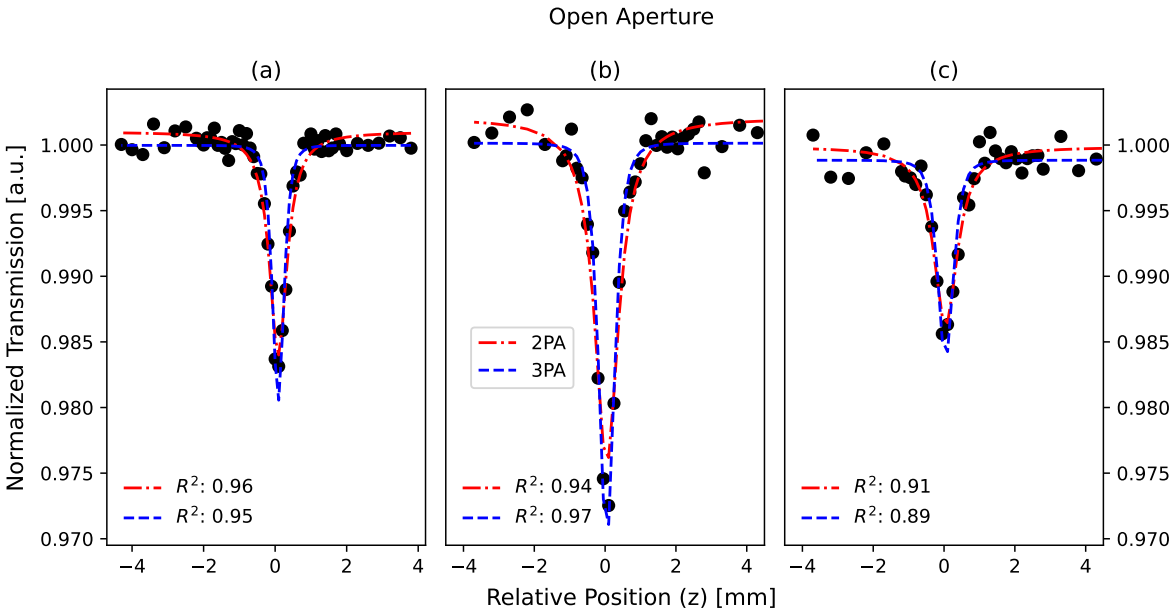


Figure 4.25 Open aperture traces fitted with 2PA and 3PA models for samples (a) 1, (b) 2, and (c) 3.

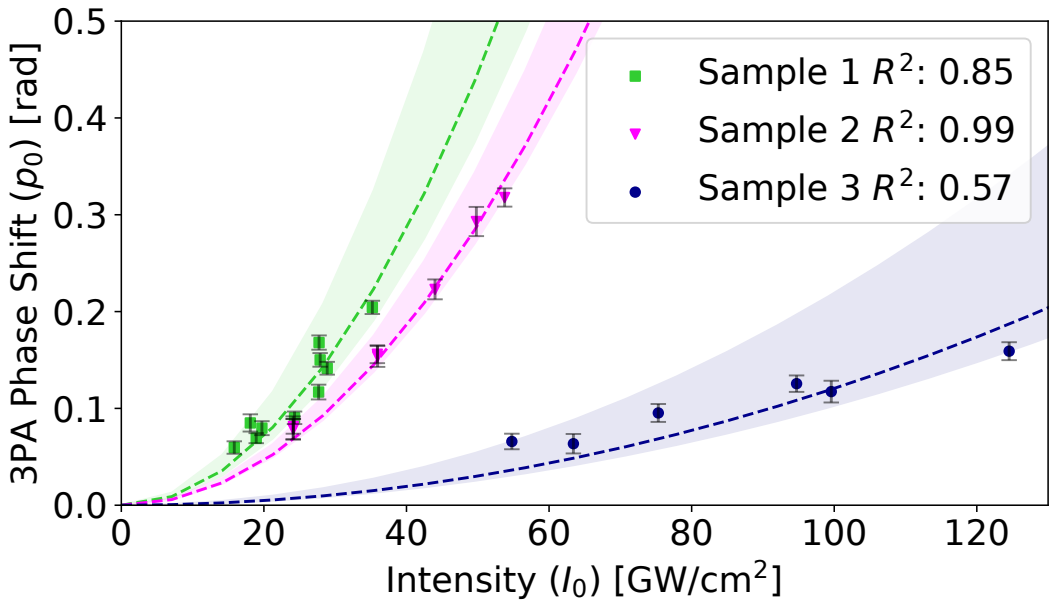


Figure 4.26 Three-photon absorption extraction for samples $1-3$. The shaded areas again illustrate the range of the quadratic coefficients which would be extracted from the spread in data points.

As in Equation (4.5), the phase shift $p_0$ follows a quadratic dependence on $I_0$, as opposed to linear in the case of $q_0$ for $\beta_{\mathrm{2PA}}$. In order to compare the linear 2PA and quadratic 3PA fits, the $R^2$ values are investigated. The results are summarized in Table 4.4.

Table 4.4 Multi-photon absorption extracted for each sample.

| Sample | Target | Thermal | $\beta_{\mathrm{2PA}}$ [$\times 10^{-11}$ m/W] | $R^2$ | $\beta_{\mathrm{3PA}}$ [$\times 10^{-25}$ m$^3$/W$^2$] | $R^2$ |
|---|---|---|---|---|---|---|
| 1 | 1 | As-dep. | $7.1 \pm 0.4$ | 0.772 | $6.6 \pm 0.3$ | 0.850 |
| 2 | 2 | As-dep. | $7.2 \pm 0.6$ | 0.822 | $4.40 \pm 0.09$ | 0.987 |
| 3 | 2 | 215 °C | $1.89 \pm 0.06$ | 0.946 | $0.47 \pm 0.04$ | 0.575 |

From Table 4.4 as well as Figure 4.26, we can see that the 3PA model provides a better fit than the 2PA model for both as-deposited samples 1 and 2. Contrastingly, the 2PA model fits much better for the higher intensity data acquired from the annealed sample 3.

Another method for the distinction of the multi-photon absorption order is to plot the result of $\ln(1 - T_{\mathrm{OA,\,min}})$ against $\ln(I_0)$, where $T_{\mathrm{OA,\,min}}$ is the minimum transmission observed in the open aperture trace dip. The slope should then provide an indication of the order, such that 2PA gives a slope of 1, while 3PA gives a slope of 2 [49]. This fit was performed for samples $1-3$, once letting the slope vary as a free parameter, and then by fixing the value to 1 or 2, to verify the $R^2$ of the fit in either theoretical circumstance. The results of these fits are presented in Table 4.5.

Table 4.5 Result of $\ln(1 - T_{\mathrm{OA,\,min}})$ vs. $\ln(I_0)$ slope fits for samples 1-3.

| Sample | Best Slope | $R^2$ | Slope 1 (2PA) $R^2$ | Slope 2 (3PA) $R^2$ |
|---|---|---|---|---|
| 1 | 1.53 | 0.925 | 0.814 | 0.839 |
| 2 | 1.84 | 0.960 | 0.759 | 0.953 |
| 3 | 1.17 | 0.928 | 0.909 | 0.453 |

From Table 4.5, it appears that sample 1 may be better represented by a combination of two- and three-photon absorption; sample 2 fits well with 3PA, and sample 3 would suit 2PA. While annealing should reduce losses, and thus we would expect less loss in sample 3, we also probed the sample at much higher intensities, which could excite simultaneous 2PA and 3PA.

Finally, the z-scan open aperture traces for each sample were fitted using a model for simultaneous 2PA and 3PA [82]. In this model, the on-axis peak phase shifts due to two- and

three-photon absorption are variables, along with the vertical and horizontal offset on the traces, similarly to the previous models. On each trace, this model, as well as the simple 2PA or 3PA models were compared using the $R^2$ values.

On an individual trace level, the simultaneous model yielded comparable fits to either pure 2PA or 3PA model. Unfortunately, it remained difficult to differentiate between 2PA and 3PA, since similar quality fits could be obtained on a single trace by fitting either contribution to the phase shift ($q_0$ or $p_0$) as the predominant one. This resulted in some fits showing stronger 2PA and others showing stronger 3PA on different traces for the same sample, which is not logically consistent. This is attributed to the noisiness of the z-scan data, as well as the narrow range of data points, resulting in similar fits over a broad range of parameters.

Using all of the information presented, for sample 1, the individual traces typically fit very slightly better with the pure 3PA model. Looking at the overall phase shift trends in Table 4.4, we see this reflected as well, with the 3PA coefficient $R^2$ being more elevated. Finally, using the transmission dip slope from Table 4.5, we again find a slightly better result for 3PA. However, we also see that the optimal slope was about 1.53, which points to simultaneous effects.

For sample 2, the individual traces showed consistently better results using the 3PA model, although close with the other models for some traces. Comparing the phase shift vs. intensity trend fits, the 3PA phase shifts matched significantly better than the 2PA phase shifts, as in Table 4.4. Using the logarithm slope method, 3PA was again the superior model, specified in Table 4.5. Thus, sample 2 seems to align better with a 3PA behaviour.

For sample 3, the individual trace fits were mostly better using the 3PA model, but only very marginally so, with the 2PA model being extremely close and surpassing 3PA in some cases. The 2PA model strongly outperformed the 3PA model when comparing the phase shift trends as well as the logarithm transmission dip, as evidenced in Tables 4.4 and 4.5. As a result, it seems that sample 2 would be best modelled using 2PA. The lower value of $\beta_{2\mathrm{PA}}$ found for this annealed sample is also more consistent with literature, which reinforces this assessment.

Overall, the data is mostly well represented by either model, and while in the as-deposited samples the 3PA model provides a modestly better fit, the opposite is true for the annealed sample. The 2PA model fits all samples quite well, and given the higher probability of 2PA over 3PA in consideration of $h\nu/E_{\mathrm{g}}$, 2PA is assumed to be the primarily observed phenomenon. The simultaneous occurrence of both phenomena should better explain the results, in particular for sample 1, but the modelling was inconclusive. Further analysis using more in-depth models accounting for saturation could provide clearer insight [83]. Given a

wider range of intensities, the order of MPA should be more evident [83]. Repeating z-scan measurements on samples with thicker GSSe films may help to extract more data points at lower intensities to verify the nature of the absorption process.

### Thermal Effects

In terms of the origin of the transmission changes observed, regardless of whether two- or three-photon absorption is at play, the results of the repetition rate experiments showed that the effects do not come from thermal lensing. In Figure 4.23, we can see that despite the low number of data points, the peak-valley transmission appears relatively constant from $1 - 100$ kHz. Since the average power scales with the repetition rate, we can conclude that the observed traces are constant over two orders of magnitude of average power, especially considering the standard deviation on the values extracted from the fit. In fact, if fitting a linear model over Figure 4.23, we find slopes of about $1.4 \times 10^{-5}$ and $-7.6 \times 10^{-7}$ for the as-deposited and annealed sample respectively. These are very close to zero, confirming the constant model as prevailing over a linear trend. As such, we can safely rule out thermal lensing as the primary contributor to any observed phase shift.

Other phenomena are sometimes attributed to these variations, such as free carrier absorption. Free carrier absorption occurs when "free carriers," generated following electronic transitions, absorb photons and alter the refractive index of the material [84]. This absorption would manifest in the closed aperture traces [28], and is a known drawback of silicon, but for GSSe and other ChGs, carrier losses are negligible [85]. As a result, we can confidently attribute the transmission dips to nonlinear absorption.

### Damage Threshold Estimation

The z-scans of samples 2 and 3 were performed with increasing intensity with the secondary objective of qualitatively assessing the onset of laser damage. Laser damage can be observed either visually, on the surface of the sample, or as an aberration in the z-scan traces. When the z-scan is performed, the sample is translated through $z_0$ forward and backward. If on the return, the trace follows a markedly different trajectory than on the forward passage, this is an indication that damage has occurred and the sample is locally altered.

The as-deposited sample 2 traces are shown in Figure 4.27 (a). The traces for the annealed sample 3 are shown in Figure 4.27 (b).

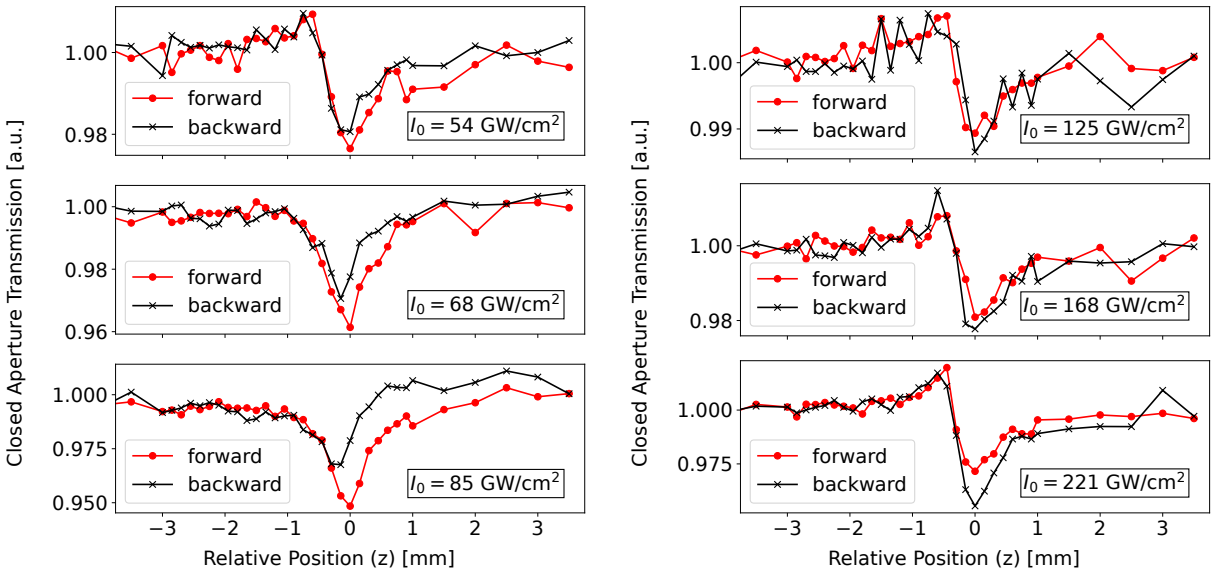


(a) Sample 2 (As-deposited)

(b) Sample 3 (Annealed)

Figure 4.27 Closed aperture traces showing damage.

From these two figures, we can qualitatively estimate the damage threshold for sample 2 to be between $54 - 85$ GW/cm$^2$ and $125 - 221$ GW/cm$^2$ for sample 3. While these are not to be taken as exact measurements, it is clear that the damage threshold is much higher for the annealed sample than the as-deposited sample. This is unsurprising given the reduced absorption observed in sample 3, which would also point to higher irradiation being necessary to cause alterations on the sample.

Further experiments could be performed with a finer step in intensity levels in order to acquire more data to pinpoint a precise threshold. Regardless of the exact values, the annealed sample clearly showed improved resilience to higher intensities than the as-deposited sample, with approximately twofold increase in the damage threshold. This confirms the hypothesis of reduced absorption increasing damage threshold for sputtered GSSe films.

### 4.5.4 Conclusion

All factors considered, the second half of sub-objective 1 can be considered at least partially successful. The goal was to determine the nonlinear optical parameters of thin film GSSe, which was evaluated by z-scan to find $n_2$ and $\beta_{2\text{PA}}$ for as-deposited and annealed sputtered films. There remains some room for debate as to the order of the multi-photon absorption which was measured, which should be clarified with additional measurements, but the

absorption behaviour can be well modelled in either case, which is the important consideration for nonlinear device fabrication. Clear differences were also observed after annealing, which suggests future work could be carried out to optimize and tune the resulting nonlinear coefficients.

# CHAPTER 5 WAVEGUIDES AND RESONATORS

In this chapter, GSSe is deposited and fabricated into waveguides for nonlinear optics. First, waveguide component design and simulation is discussed, followed by fabrication and linear characterization, in alignment with sub-objective 2. Preliminary results for the fabrication of micro-ring resonators are also discussed. Finally, the observation of four-wave mixing in GSSe waveguides is investigated, in accordance with sub-objective 3.

## 5.1 Component Design

### 5.1.1 Coupler Design

#### Edge Couplers

In order to perform experiments with waveguides on a chip, light must be coupled into and out of the waveguides via optical fibres. The first considered strategy is edge coupling, where light is injected directly in-plane with the waveguide's facets.

This strategy is relatively straightforward and poses little restriction on wavelength or polarization. The biggest challenge comes from the mismatch between the typically small waveguide mode and the often much larger fibre mode. Precise alignment is also required to maximize coupling, which can be experimentally challenging. The most common implementation of an edge coupler is a taper.

In a taper, the waveguide dimensions (typically the width) are gradually expanded to more closely correspond to the fibre's output. Alternatively, in an inverse taper, the waveguide is significantly narrowed such that the mode becomes less confined within its core and the evanescent field grows, potentially matching the fibre mode. This typically requires very narrow widths which may be challenging to fabricate. As such, this work will focus on the former, expanding taper. The design choice consisted of simply expanding the width of the waveguide linearly up to a width of 10 µm, which is closer to the mode size of the single-mode fibres used, and allows for easy visual alignment.

#### Grating Couplers

The second investigated solution is grating coupling, where light is injected into and out of the chip with out-of-plane via diffraction gratings on chip. The main advantage of this method is that it allows light to be coupled into waveguides with smaller dimensions and that it reduces

the risk of parasitic coupling between the fibres themselves. One drawback of this method is the design complexity, as there are many parameters which affect coupling efficiency. Furthermore, these couplers are intrinsically wavelength and polarization-dependent, which induces bandwidth limitations that may restrict nonlinear optical experiments. Finally, the narrow and closely spaced periodic structures characteristic of grating couplers require careful optimization of the lithography process to mitigate any undesirable proximity effects.

The primary parameters for grating coupler design are the grating pitch ($p$) and the duty cycle ($d$), which both strongly affect the grating's central wavelength and performance. Other parameters include the fibre angle and position over the grating. While the fibre angle can affect the central wavelength, it will be fixed in this simulation for simplicity, while pitch and duty cycle will be the variables. The fibre position affects insertion loss, but is not a design factor dictating the overall performance of the device, and as such it will also be fixed in the following simulations. Finally, the etch depth of the grating is another highly influential parameter, but since the gratings in this work will be fabricated by lift-off, only a fully-etched design will be analyzed. The design parameters are summarized in Figure 5.1 [86].

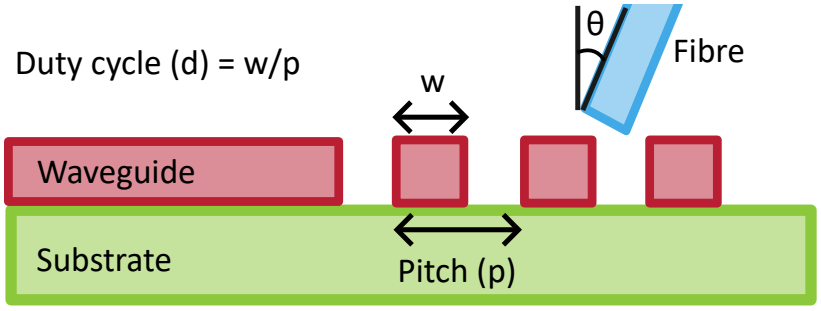


Figure 5.1 Fully-etched grating coupler design parameters.

In order to identify suitable design parameters, 2D Finite-Difference Time-Domain (FDTD) simulations were performed using Ansys Lumerical. The simulations were run on a mesh refinement of 4, using the software's non-uniform meshing, which provided cells of approximately $\Delta x = \Delta y = 20$ nm in the grating region.

The device was designed to be air-clad, fully etched, and with a GSSe thickness of 400 nm. Refractive index data was imported from ellipsometry data as presented in Chapter 4. For simplicity, the fibre angle was fixed at 10°. The simulations were performed by sweeping the pitch between $0.5 - 2.5$ µm and the duty cycle between $0.3 - 0.8$, with 25 points for each parameter. Performance was measured as the normalized transmission from the fibre into the waveguide at the target wavelength of 1550 nm for a TE polarization. The result of the simulation is presented in Figure 5.2.

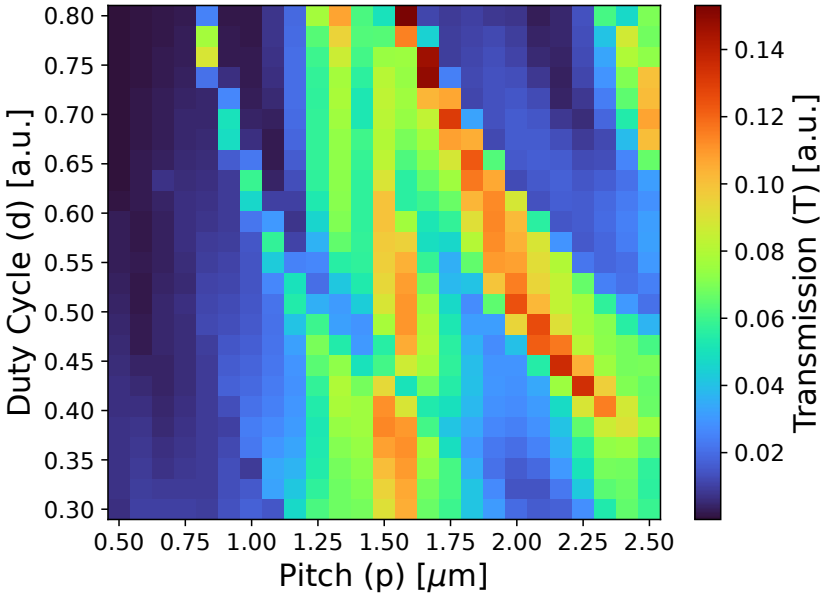


Figure 5.2 Simulated grating coupler transmission at 1550 nm across various dimensions.

Figure 5.2 shows several parameter ranges presenting local maxima in transmission. It is again worth noting that while the transmission values are low, the fibre position can be optimized in practice to yield higher values without altering the device's design.

The final design was chosen to be kept as simple as possible as a first iteration. A pitch of 2 µm and a duty cycle of 50% was selected. With these design parameters, a coarse sweep of the fibre position was performed and transmission was found to reach about 20%, which is likely near the maximum value, but may be further optimized by adjusting the other parameters previously mentioned. Future work could include designing partially etched couplers to decrease back-reflection losses, and apodizing the grating pitch to decrease mode mismatch between the fibre and coupler [86]. Adding an oxide cladding could also decrease back-reflections, in addition to optimizing the chosen buried oxide thickness to create constructive interference from the reflections off the substrate [87].

### 5.1.2 Waveguide Design

In terms of the waveguides themselves, single mode operation is the ultimate goal in order to minimize mode losses. For a waveguide to only support one transverse electric (TE) or transverse magnetic (TM) mode, its cross-section (width and height) must be sufficiently small. Additionally, since the ultimate application of these waveguides is for nonlinear pho-

tonics, the effective mode area ($A_{\text{eff}}$) must be small to maximize the waveguide's nonlinear parameter $\gamma_{\text{NL}}$ [12]:

$$\gamma_{\text{NL}} = \frac{2\pi\ n_2}{\lambda\ A_{\text{eff}}}\ , \tag{5.1}$$

with an effective area given by

$$A_{\text{eff}} = \frac{(\int |\mathbf{E}|^2\ \mathrm{d}A)^2}{\int |\mathbf{E}|^4\ \mathrm{d}A}\ . \tag{5.2}$$

For these reasons, the reduction of the waveguide's dimensions is advantageous. However, fabrication and experimental constraints ultimately pose limitations on the achievable minima, with larger waveguides being significantly easier to fabricate. As such, some waveguides will be fabricated beyond these ideal dimensions in order to serve as a starting point for future improvement.

### Waveguide Modes

In order to determine the single mode cutoff dimensions, Finite Difference Eigenmode (FDE) simulations were performed. A two-dimensional sweep was performed using Ansys Lumerical, where width and height were varied and the mode effective indices $n_{\text{eff}}$ were tracked to determine the point where multiple TE and/or TM modes were supported. All simulations were performed for a target wavelength of 1550 nm.

The waveguide configuration was chosen to be a simple rectangular GSSe strip, to maximize confinement and fabrication simplicity with a lift-off process. The dispersion data of the GSSe film measured in Chapter 4 via ellipsometry was imported into the software and used for the simulations. The waveguide was chosen to be air-clad to maximize refractive index contrast and thus increase confinement, and the substrate was chosen to be a 5 µm-thick $SiO_2$ layer on a silicon wafer. The configuration is illustrated in Figure 5.3.

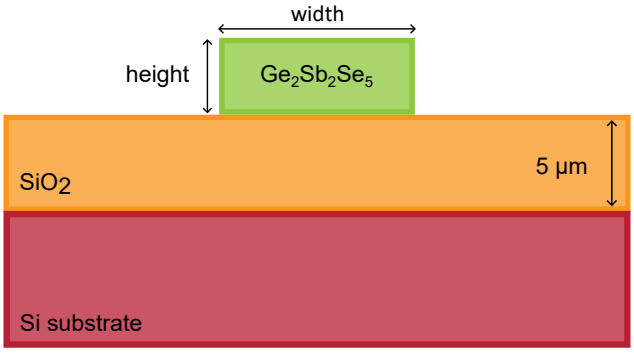


Figure 5.3 Schematic of the GSSe waveguide configuration for design.

The simulations were run using mesh steps of approximately $\Delta x = 0.0375$ µm and $\Delta y = 0.025$ µm. The width of the waveguide was swept from $200 - 1000$ nm and the height was swept from $200 - 1000$ nm, with 17 points for each range. The resulting number of supported modes in accordance to the waveguide dimensions is presented in Figure 5.4.

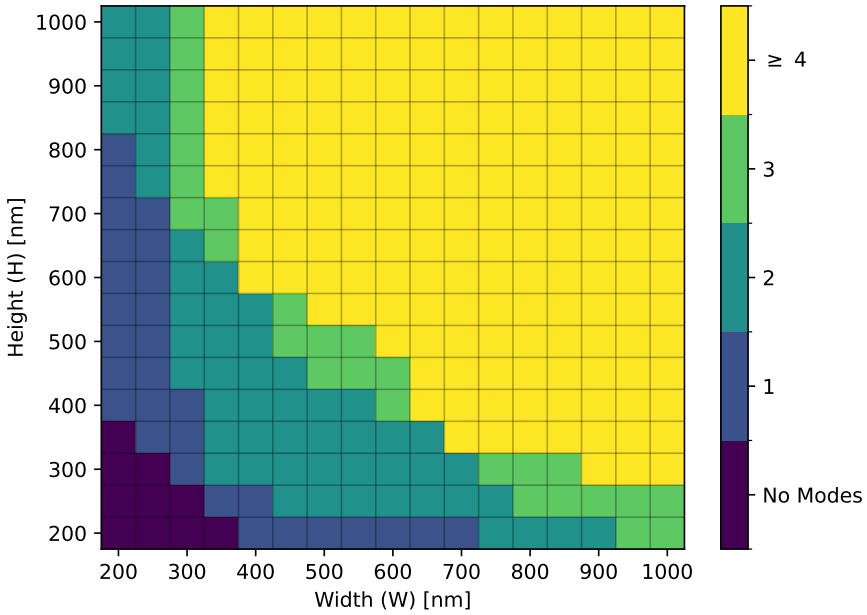


Figure 5.4 Number of modes supported across waveguide dimensions at 1550 nm.

The results of the simulations presented in Figure 5.4 show that 300 nm is the minimum of either dimension required for mode propagation in the waveguide.

### Effective Mode Area

The effective area of the fundamental mode for each dimension was also calculated. A mapping is presented in Figure 5.5. The mode effective area presented below is that which is built into Lumerical's FDE solver, corresponding to Equation (5.2).

From Figure 5.5, two symmetric regions with minimal effective area of $0.3\,\mu m^2$ or less are revealed. Overall, the effective area does not show great variation in the low-mode waveguide dimensions, which lends more flexibility to the waveguide sizing.

Considering the results of both Figures 5.4 and 5.5, ideal waveguide dimensions for nonlinear photonics would be in the area of 600 nm by 200 nm, as this minimizes both mode number and effective area. In practice, larger waveguides will be fabricated in order to facilitate coupling

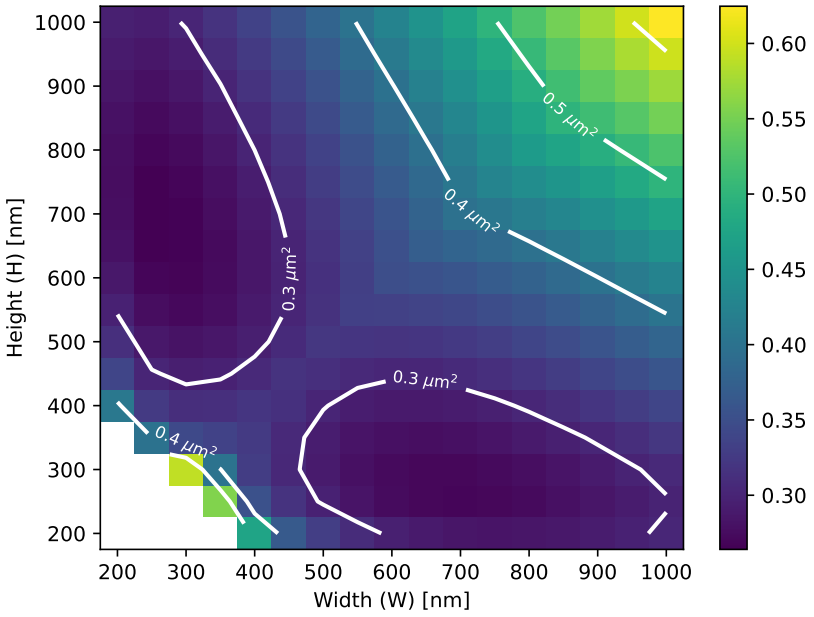


Figure 5.5 Effective area of the fundamental mode across waveguide dimensions.

and fabrication, at the cost of increased mode losses and reduced nonlinear efficiency. Future work should focus on successful fabrication and coupling with single-mode waveguides.

### 5.1.3 Micro-ring Resonator Design

The last basic element to be fabricated to achieve four-wave mixing for eventual photon generation consists of micro-ring resonators. In this design, they are coupled evanescently to straight waveguides as described in the previous section, with a schematic presented in Figure 5.6.

Micro-ring resonators aim to increase the light-matter interaction in order to enhance observed nonlinear effects. The resonant condition,

$$m\lambda_0 = n_{\text{eff}} L \ , \tag{5.3}$$

is satisfied when the optical path in the cavity of length $L = 2\pi R$ and effective index $n_{\text{eff}}$ corresponds to integer multiples $m$ of the target wavelength $\lambda_0$. At these wavelengths, light is

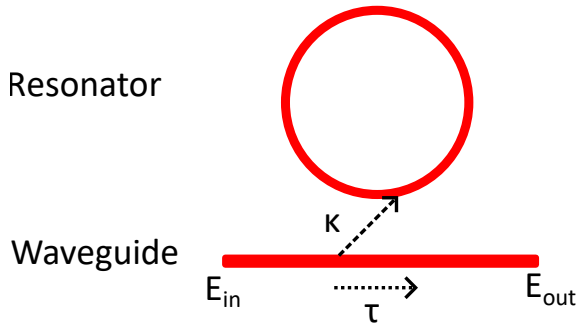


Figure 5.6 Micro-ring resonator coupling schematic.

confined, which gives rise to dips in a transmission spectrum. The resulting spectrum follows

$$T = \frac{a^2 - 2\tau a \cos(\phi) + \tau^2}{1 - 2\tau a \cos(\phi) + (\tau a)^2} \ , \tag{5.4}$$

where $a^2 = \exp(-\alpha L)$ is the power attenuation coefficient, $\tau$ and $\kappa$ are the self- and cross-coupling coefficients as in Figure 5.6, with $|\tau|^2 + |\kappa|^2 = 1$, and $\phi = 2\pi\ n_{\text{eff}}\ L/\lambda$.

The separation between peaks is represented by the free spectral range,

$$\text{FSR} = \frac{\lambda^2}{n_g L} \ , \tag{5.5}$$

with $n_g$ the group index of the waveguide.

The sharpness of these peaks is related to the degree of confinement of light in the resonator, and can be measured using the quality factor $Q$:

$$Q = \frac{\lambda_0}{\delta\lambda} \ , \tag{5.6}$$

where $\delta\lambda$ is the full width at half maximum in terms of wavelength [26].

In the context of four-wave mixing, micro-ring resonators provide a field enhancement factor given by [88]:

$$F = \left| \frac{\kappa}{1 - \tau \exp(-\alpha L/2 + iLk)} \right|^2 \tag{5.7}$$

The resonators designed for FWM must have resonances at the target pump, signal, and idler wavelengths with the correct spectral separation to allow each of these frequencies to interact in the resonator and benefit from the enhancement in Equation (5.7).

Using Lumerical FDE, the group index for the fundamental mode of waveguides with a width

of 600 nm and a height of 430 nm was calculated to be 3.58, and the effective index, 2.33. For ring resonators, the length corresponds to $L = 2\pi R$. Resonators were fabricated with radii of 8 µm and 12 µm, giving expected FSR of 13.4 nm and 8.4 nm respectively.

## 5.2 Summary of Fabricated Structures

The general fabrication process consisted of cleaning thermal oxide silicon substrates, followed by resist spin-coating, baking, and developing. Lithography was used to transfer the desired pattern into the resist, after which GSSe was sputtered to the desired thickness following the processes described in Chapter 4. Finally, a lift-off process concluded the patterning by soaking the sample in the appropriate commercial remover solution.

Two lithography techniques were considered for this work, namely electron-beam lithography (EBL) and direct laser writing lithography. EBL allowed for narrower waveguide widths due to its higher resolution, but limited the waveguide height due to the thin nature of EBL resists available. Direct writing allowed for thicker GSSe films, but restricted the minimum width due to the more limited lateral resolution in comparison to EBL.

Three chips were used to gather the data reported here. Since the fabrication processes available ultimately constrained the achievable feature sizes, the lithography and lift-off steps affected the final design choices. In the end, all chips which will be discussed were fabricated using direct laser writing lithography.

### 5.2.1 Chip B1 - Waveguides for Propagation Loss

The first chip, labelled Chip B1, was used to estimate the propagation loss of waveguides using the cut-back method.

On a clean silicon substrate with 5 µm of oxide, LOR 5A and AZ 900 MIR resist were spin-coated and subsequently exposed using direct-write lithography (Raith PicoMaster 150, Polytechnique Montréal Microfabrication Laboratory). After development with AZ 726 MIF, GSSe was sputtered (9 min, 75 W RF power, 10 sccm Ar gas flow, 5 mTorr pressure) to an approximate thickness of 400 nm, and lift-off was completed in Microposit Remover 1165 solution. This chip was fabricated with the assistance of Salvador Poveda-Hospital and Khaled Elouaer from the Microphotonics Laboratory.

The chip layout consisted of 90° bends with a large radius of 600 µm in order to minimize bend losses. The total waveguide lengths varied from about $2.4 - 5.6$ mm after cleaving for edge coupling. In order to facilitate alignment, the waveguides had an input width of

10 µm, which was tapered down to 3 µm for the main component width. A schematic of the chip layout is presented in Figure 5.7 (a), and a close-up of the resulting tapers following fabrication is presented in Figure 5.7 (b). We can see that the GSSe layer adhered well to the substrate and preserved the smooth taper design.

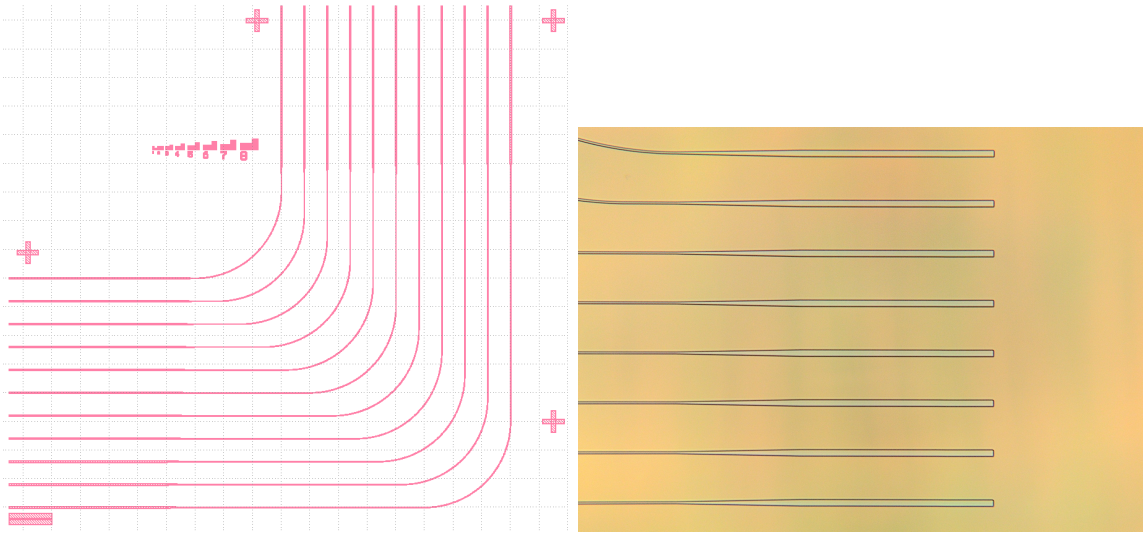

(a) Chip B1 layout. (b) Chip B1 tapers.

Figure 5.7 Fabrication of Chip B1.

### 5.2.2 Chip B2 - Waveguides for Four-Wave Mixing

The second chip, labelled Chip B2, was fabricated with the intent of obtaining waveguides in which preliminary four-wave mixing experiments could be performed, while simplifying fabrication.

On a clean silicon substrate with a 5 µm-thick thermal oxide layer, LOR 5A and AZ 5214 E were spin-coated and patterned using a direct laser writer photolithography system (Raith PicoMaster 100) at the LaCIME facilities at the École de technologie supérieure, then developed using AZ 726 MIF solution. The GSSe film was sputtered (25 min, 75 W RF power, 10 sccm Ar gas flow, 5 mTorr pressure) to a thickness of 1.1 µm as measured by profilometry. The patterning was completed with a lift-off in a Microposit Remover 1165 solution bath.

The layout, presented in Figure 5.8, consisted of large straight waveguides with widths varying from $0.5 - 10$ µm, paired with a taper to a maximum width of 10 µm. The pattern was repeated with s-bend segments of the same dimensions, in an attempt to offset any parasitic coupling between the fibres themselves during alignment. The waveguides were cleaved for

edge coupling to a total chip length of approximately 9 mm including the wide tapered segments.

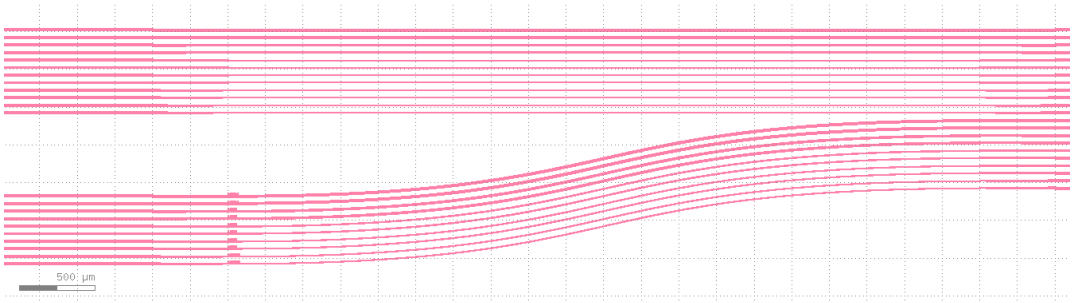


Figure 5.8 Schematic of Chip B2 layout.

After lift-off, only the waveguides with widths of 2 µm and larger remained, as can be seen in Figure 5.9. This is likely due to a sub-optimal development of the narrower features during lithography causing resist residue which prevented adhesion of GSSe to the substrate. The larger waveguides were still in good condition and were used for subsequent experiments.

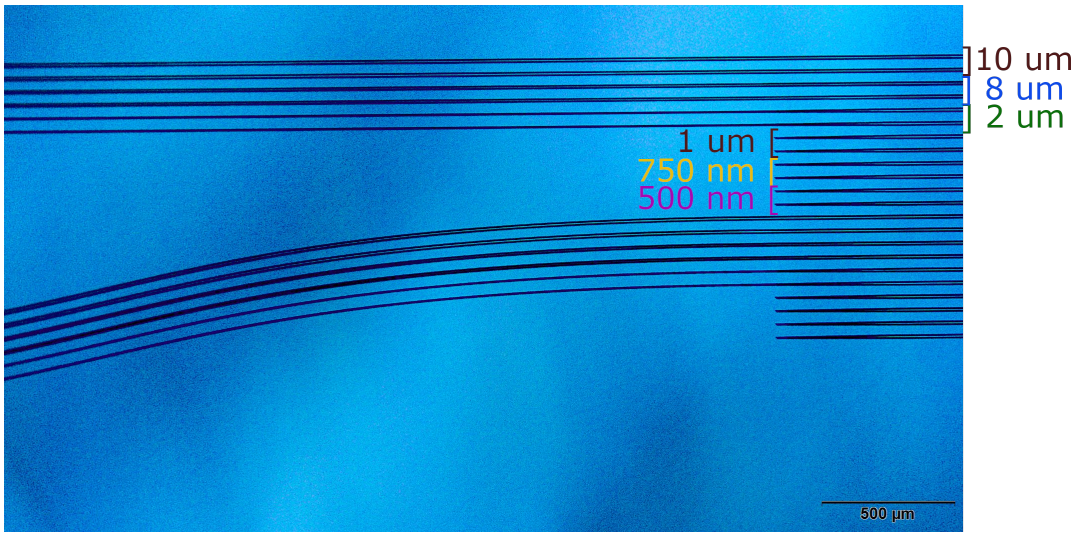


Figure 5.9 Waveguide delamination on Chip B2 after lift-off.

### 5.2.3 Chip B3 - Waveguides with Resonators

The third chip, labelled Chip B3, was fabricated to test waveguide coupling with grating couplers and micro-ring resonators.

On a clean silicon substrate with 5 µm of thermal oxide, OIR 674-11 resist was spin-coated and patterned by direct-write lithography (Raith PicoMaster 150). A 430 nm GSSe layer was

then sputtered (50 W, 10 sccm, 5 mTorr argon gas, 19 minutes) and measured by profilometry. Lift-off was completed with a soak in Microposit Remover 1165.

The layout consisted of straight waveguides with lengths between $2.75 - 3.75$ mm and a nominal width of 600 nm. Two different grating coupler models were used, each having a pitch of 2 µm and a 50% duty cycle, with one model being a simple rectangular grating paired with a taper, and the second using a triangular focusing design. Additionally, micro-ring resonators were coupled to some waveguides, with radii of 8 µm and 12 µm, and nominal coupling gaps between $300 - 700$ nm. A schematic of the layout is shown in Figure 5.10, with the proportions slightly altered for the sake of visibility in the diagram.

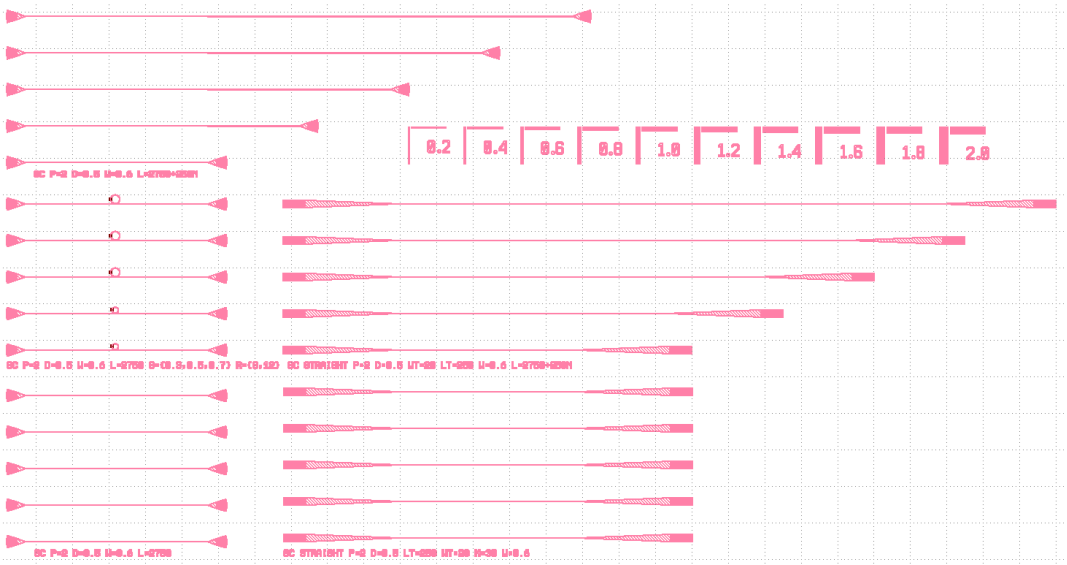


Figure 5.10 Schematic of Chip B3 layout (resized for visual clarity).

After development, the resulting pattern in the resist was investigated with an optical microscope. There, it was observed that the narrow spacing of 1 µm between the grating teeth resulted in over-exposure in the grating areas, which altered the design. After lift-off, there appeared to be resist remaining under the GSSe layer in the grating. These defects are presented in Figure 5.11. While this was not the original design intent, the gratings were tested regardless, as the elevated refractive index of GSSe should still allow propagation through this multi-layered structure.

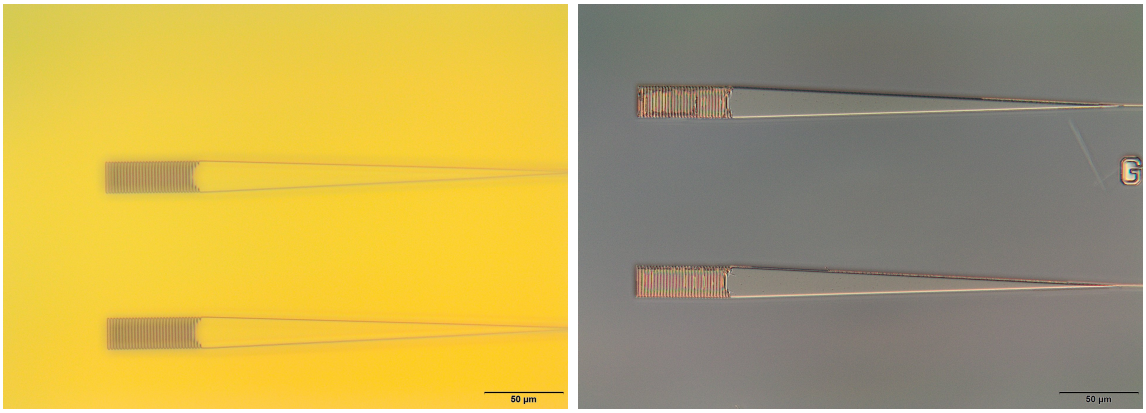

(a) After development (b) After lift-off

Figure 5.11 Defects during fabrication of straight grating couplers on Chip B3.

## 5.3 Linear Optical Characterization

### 5.3.1 Waveguide Transmission

Chip B1, as described in chapter above, was used to perform measurements on waveguide transmission. In order to measure the propagation losses in the waveguides, the cut-back method was employed by edge-coupling a 12.3 dBm laser at a wavelength of 1550 nm to the various waveguides on the fabricated chip. As a reminder, each waveguide had a nominal height of 400 nm and a component width of 3 µm. The measured total losses are plotted in Figure 5.12.

In order to extract the insertion losses and deduce the propagation losses, the data points from Figure 5.12 are fitted to the following equation:

$$\text{Loss} = \alpha_{\text{wg}} x + 2\,\text{IL} \tag{5.8}$$

with $\alpha_{\text{wg}}$ corresponding to the waveguide propagation loss in dB/mm, $x$ being the total waveguide length in mm, and IL representing the insertion loss for each facet in dB. The linear regression finds a propagation loss of 3.58 dB/mm and an insertion loss of about 12 dB per facet. From these results, and considering the negligible material absorption of GSSe as measured in Chapter 4, it is clear that the losses are mostly attributable to scattering from the waveguides as well as mode mismatch between the fibres and waveguides. In order to improve these results, the fabrication process could be optimized, perhaps using dry etching to pattern the waveguides followed by a reflow as in [52]. Nevertheless, the propagation loss

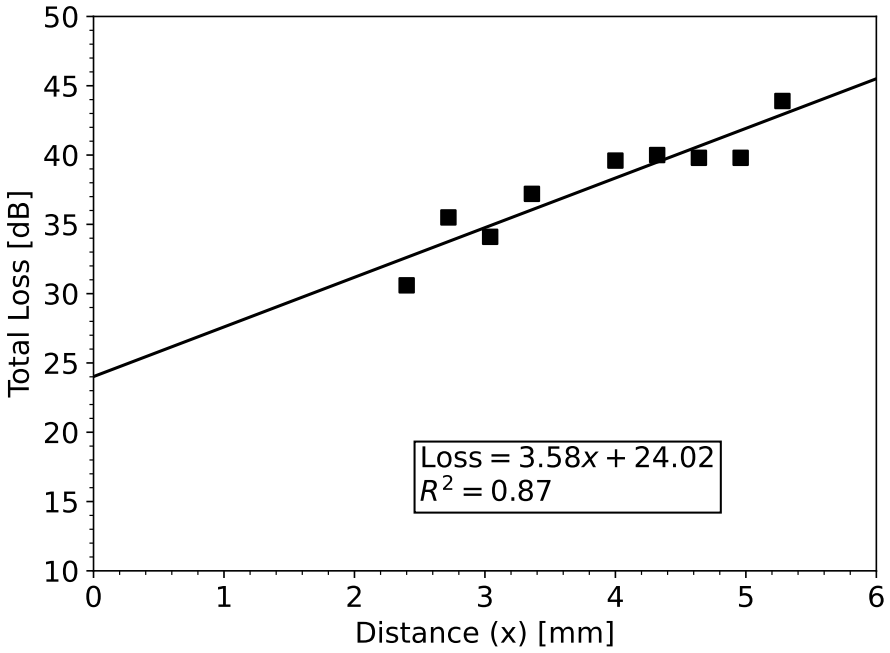


Figure 5.12 Total losses measured for bent waveguides on Chip B1.

calculated here is taken as a reference value for the rest of the waveguides, as the fabrication process was largely the same. For more accurate results, a larger range of waveguide lengths should be fabricated and this process should be repeated for each waveguide geometry.

### 5.3.2 Resonator Spectra

Micro-ring resonators form the basis of the proposed photon source design. In order to test fabrication capabilities with GSSe, some resonators were designed and fabricated on Chip B3. A total of five ring resonators were fabricated, with the parameters summarized in Table 5.1.

Table 5.1 Fabricated ring resonator parameters

| Ring | Radius [µm] | Gap [nm] |
|---|---|---|
| 1 | 8 | 300 |
| 2 | 8 | 500 |
| 3 | 12 | 300 |
| 4 | 12 | 500 |
| 5 | 12 | 700 |

Chip B3 waveguides were designed with grating couplers, which have a bandwidth of their own. To ensure that spectral features are due to the resonators and not the gratings, the transmission was recorded through waveguides with no rings as a comparison. To do so, light from a broadband infrared laser (Newport BBS-430) with a nominal power $\geq -5$ dBm over the range of $1540 - 1600$ nm was coupled into the gratings via optical fibres. The output transmission spectrum was recorded using an optical spectrum analyzer (OSA) (Agilent HP86142A).

The spectrum of the laser itself is presented in Figure 5.13.

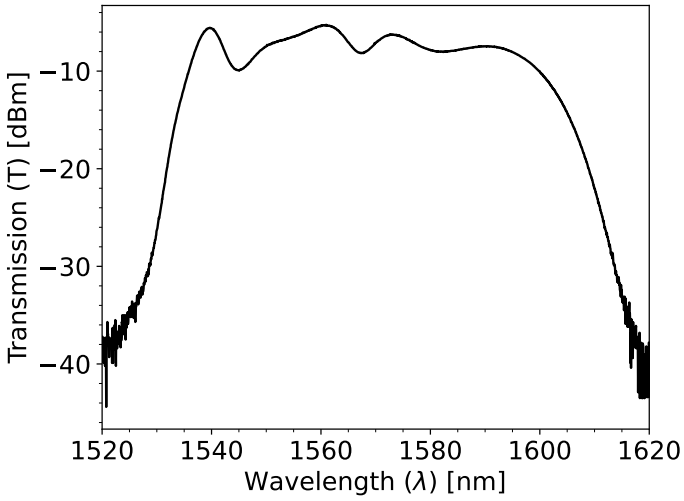


Figure 5.13 Spectrum of broadband laser.

The spectrum through a straight waveguide with the focusing grating coupler design is presented in Figure 5.14. The spectrum is filtered with a Savitzky-Golay filter to reduce noise. We can see that despite the low transmission, the shape of the spectrum remains similar to that of the laser itself, implying that the grating's bandwidth is larger than that of the laser.

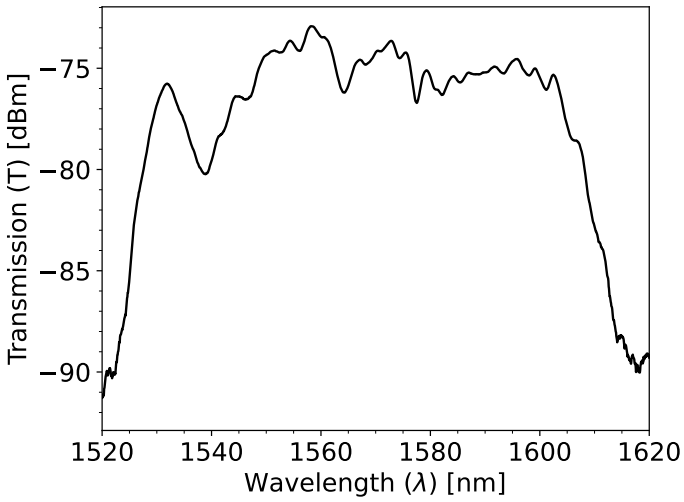


Figure 5.14 Transmission spectrum through waveguide 4 with focusing grating couplers.

Next, the spectrum through ring 1 was recorded, filtered, and presented in Figure 5.15, with the spectrum of waveguide 4 overlaid for comparison. The free spectral range (FSR) experimentally measured for ring 1 was about 16 nm, compared to a theoretical value of 13.4 nm ($\Delta = 19\%$). This difference can be explained by fabrication variability, as the exact dimensions of the waveguides differed from the nominal values, as well as experimental uncertainty caused by noisy data. From Figure 5.15, using Equation (5.6), the Q-factors of the highlighted peaks were calculated, yielding up to $1.9 \times 10^3$.

Finally, the spectrum through ring 3 was recorded, filtered, and presented in Figure 5.16. The experimental FSR is 9 nm, compared to the theoretical value of 8.4 nm ($\Delta = 7\%$). The measured value agrees well with the theoretical calculations, better than for ring 1, which can be attributed to the larger ring dimensions making fabrication more true to the design and thus to the simulated values. The spectrum is filtered with a Savitzky-Golay filter and two traces are averaged for this spectrum. The experimental Q-factors were found to be up to 940, which is smaller than for ring 1. It is worth noting that the spectra were still quite noisy, which could obscure the actual appearance of the resonance peaks.

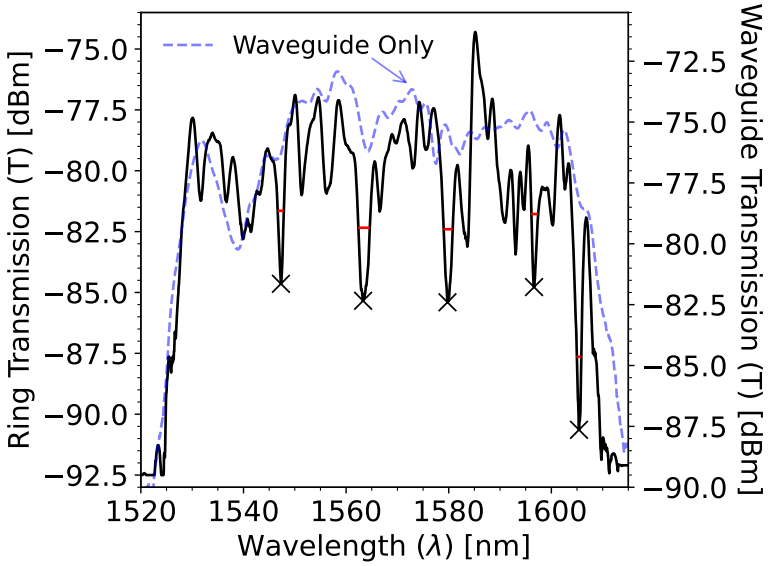


Figure 5.15 Transmission of ring 1 ($R = 8\,\mu\text{m}$).

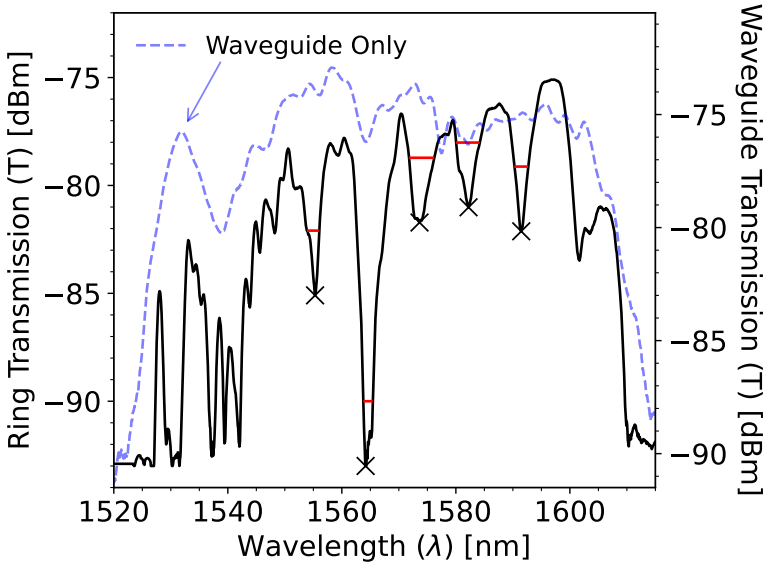


Figure 5.16 Transmission of ring 3 ($R = 12\,\mu\text{m}$).

The spectra through rings 2, 4, and 5 were too noisy to be adequately analyzed. Overall, the transmission is quite low even through the straight waveguides, which is a result of the poor outcome of the grating couplers fabricated. The spectra acquired from these resonators serve as preliminary results for future works, since no four-wave mixing could be observed under these high-loss conditions. Further improvements could be expected with better control of grating coupler and fibre alignment, polarization control, and more robust fabrication. Finally, resonators could be designed with alternate coupling configurations, such as racetrack resonators or pulley couplers to increase coupling length and increase coupling into the resonators [10, 26].

## 5.4 Nonlinear Waveguide Characterization

### 5.4.1 Setup

In order to attempt to observe four-wave mixing, an optical setup was prepared for Chip B2. A schematic of this setup is presented in Figure 5.17.

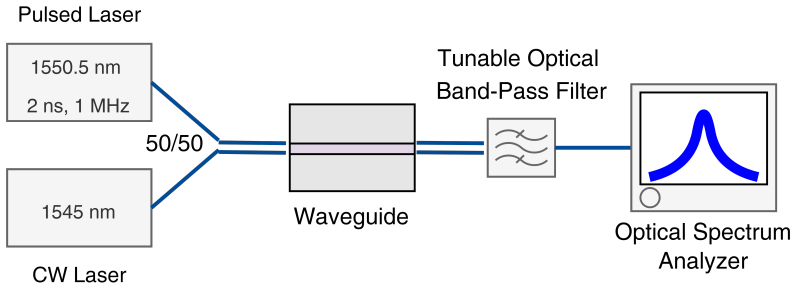


Figure 5.17 Schematic of the four-wave mixing setup.

The pump laser consisted of a pulsed laser with a wavelength of 1550.5 nm, a pulse duration of 2 ns, and a repetition rate of 1 MHz (MANLIGHT). The output pulse power was varied by adjusting the pump current via RS232 communication. The signal laser was the Keysight N7711A, tuned to a wavelength of 1545 nm with a continuous-wave (CW) input power of 16 dBm. The two lasers' signals were combined using a 50/50 fibre coupler (Oz Optics), of which an output was edge-coupled to the chip.

The waveguide under test corresponded to the second straight waveguide on Chip B2, having a width of 10 µm, a height of 1.1 µm and a total length of about 9 mm. For this waveguide, we found a nonlinear parameter $\gamma_{\mathrm{NL}}$ as in Equation (5.1) of 20.4 $\mathrm{W}^{-1}\,\mathrm{m}^{-1}$ using the $n_2 = 2.9 \times 10^{-17}$ $\mathrm{m}^2/\mathrm{W}$ found in Chapter 4.5 and the effective area extracted from FDE

simulations.

After the waveguide, the output edge-coupled fibre was connected to a tunable optical grating filter (JDS Uniphase TB9), which provides a bandwidth of approximately 1 nm around the target wavelength. The final output was then collected into an OSA (Agilent HP86142A).

### 5.4.2 Experiment

The precise central wavelength of each input laser was first measured with the OSA, giving $\lambda_p = 1550.5$ nm for the pump and $\lambda_s = 1544.931$ nm for the signal. From Equation (2.14), this gives a theoretical idler wavelength of $\lambda_i = 1556.2$ nm. The tunable filter was thus set to a central wavelength of 1556.2 nm, and the OSA sweep range was limited around this target. The noise spectrum of each laser at the idler wavelength range was also measured to ensure that no peaks could be accidentally misattributed.

The experiment was carried out by gradually increasing the pulsed pump laser's current until an evidence of an idler was recorded. At an input current of $I = 1500$ mA, corresponding to an average output power of $P_{p,\,av} = 1.75$ W (32.4 dBm) and a peak power $P_{p,\,peak} = 875$ W (59.4 dBm), FWM was successfully observed at the output of straight waveguide 2. The idler trace is presented in Figure 5.18.

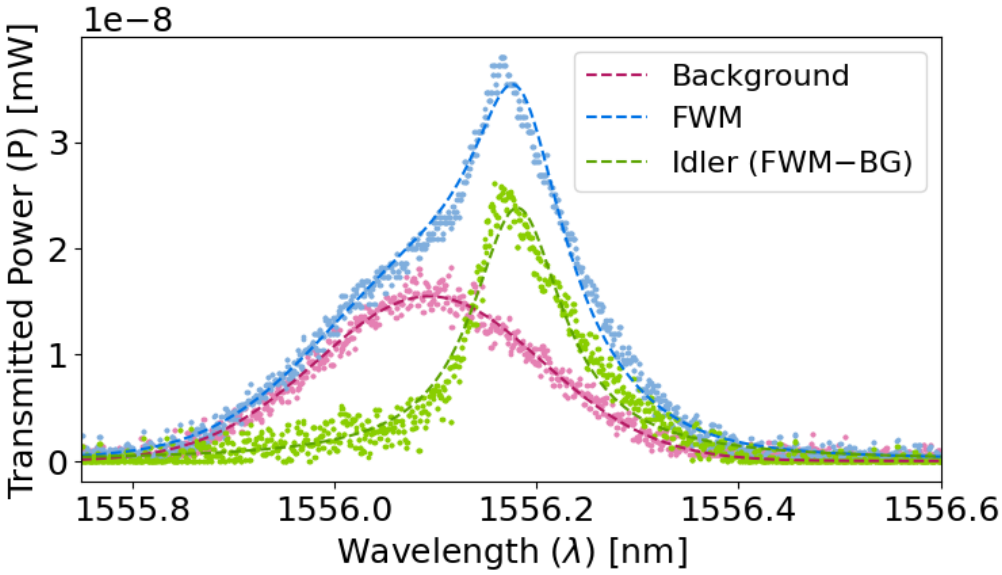


Figure 5.18 FWM idler spectrum observed in GSSe waveguide.

In Figure 5.18, the blue curve represents the "raw" FWM spectrum collected from the OSA,

with both pump and signal lasers active and the idler peak visible. The red trace corresponds to the background signal, i.e. the sum of the noise from each laser recorded separately. The Gaussian appearance is due to the tunable grating filter. Finally, the green trace is the idler's spectrum with the noise of each laser removed, corresponding to the difference between the blue and red curves. Given the pulsed nature of the pump, the idler was also pulsed, and the measured average power on the OSA was $-75.8$ dBm ($2.6 \times 10^{-8}$ mW), which corresponds to a peak power of $P_{\text{peak, i}} = -48.8$ dBm ($1.3 \times 10^{-5}$ mW). In order to determine the idler power in the waveguide, the insertion loss at the output facet of the waveguide must be subtracted. The insertion loss is estimated to be around 17 dB/facet for this waveguide, which yields an idler power in the waveguide of $P_{\text{avg, wg, i}} = -58.8$ dBm or $P_{\text{peak, wg, i}} = -31.8$ dBm. In order to evaluate performance, the FWM efficiency is defined as [89]

$$\eta_{\text{FWM}} = \frac{P_{\text{wg, i}}}{P_{\text{wg, s}}} \ , \tag{5.9}$$

where $P_{\text{wg, s}}$ is the power of the input signal in the waveguide. In the case of this experiment, accounting for 3 dB loss from the splitter and one facet's insertion loss, we have $P_{\text{wg, s}} = -4$ dBm. From Equation (5.9), we find an average conversion efficiency of $-54.8$ dB or a peak conversion efficiency of $-27.8$ dB.

### 5.4.3 Discussion

The conversion efficiency observed in this experiment was relatively low and a high pump power was required to observe FWM. This is not surprising when considering the tested structure, which consisted of very large, multimode waveguides. Despite a high $n_2$ measured for this material in Chapter 4.5, straight waveguides with no resonant structures require long enough path lengths for the nonlinear interaction to occur. As was previously observed on the waveguides fabricated on Chip B1, the propagation loss was likely more elevated than expected, which also has the effect of reducing this effective interaction length. We were unable to perform a precise measurement of the propagation losses for the waveguides of Chip B2 to confirm, since their length was too similar and coupling was difficult to reproduce consistently. In any case, the insertion loss was also elevated and could be improved using more precise alignment and lensed or high-NA fibres. Polarization was also not controlled in this experiment due to concerns about damaging equipment at high power, aside from the CW signal laser being linearly polarized, which means this result could likely be strongly improved under better experimental conditions. Finally, the use of a pulsed pump laser was necessary to achieve the high power required in this experiment, but this also means

idler generation is only possible when the pulse is present, which adds a statistical challenge to the observation of FWM. Using ring resonators such as those fabricated on Chip B3 could be highly beneficial in reducing the necessary input power required to observe FWM, especially if waveguide dimensions are also optimized for single-mode operation with smaller effective areas, boosting the nonlinear parameter. Unfortunately, the waveguides and ring resonators of Chip B3 exhibited too much loss for any nonlinear phenomenon to be observed. Additionally, the grating couplers on Chip B3 were damaged under high laser power, making FWM impossible to observe on this set of devices.

Overall, these results together serve as a proof of concept in the realization of waveguides, ring resonators, grating couplers, and finally, FWM in GSSe-based structures on-chip. While there is great room for improvement, these results can be combined to create better devices, and sub-objectives 2 and 3 can be considered completed.

# CHAPTER 6 CONCLUSION

In conclusion, this work aimed to explore $Ge_2Sb_2Se_5$ as a platform for nonlinear photonics and to lay the groundwork for the eventual fabrication of more complex devices, such as photon-pair sources on-chip. As a reminder, the main objective of this research was broken down into three sub-objectives, namely, the evaluation of the film's linear and nonlinear optical coefficients (1), and the fabrication of waveguides for linear (2) as well as nonlinear experiments (3). This was approached by performing various measurements on sputtered GSSe films, and then observing transmission and four-wave mixing in waveguides patterned from these films.

## 6.1 Summary of Works

The first part of this work focused on the deposition of GSSe by sputtering from two different targets, and some post-processing of the films with annealing. The material composition, stoichiometry, and surface oxidation was analyzed by XPS, where we found significant deviations from the expected $Ge_2Sb_2Se_5$ composition, with a result closer to $Ge_{25}Sb_{30}Se_{45}$ for Target 1, and $Ge_{29}Sb_{22}Se_{49}$ for Target 2, independent of any annealing. Oxidation was found to be extensive, with up to 42% oxygen, but limited to an overlayer thickness of less than 1 nm, which was deemed to have a negligible impact on future fabricated devices. The linear optical properties of these films were measured using spectroscopic ellipsometry with a Cody-Lorentz model, where we found refractive indices of about 2.93 and negligible absorption at a wavelength of 1550 nm for the as-deposited and low-temperature annealed films. The high-temperature 400 °C annealing showed an increased refractive index and absorption, consistent with GSSe crystallization. Finally, several z-scan measurements were performed on sputtered GSSe films, where we found elevated $n_2 \approx 2.9 \times 10^{-17}$ m$^2$/W and $\beta_{2PA} \approx 7.2 \times 10^{-11}$ m/W for as-deposited films and lower values of $n_2 \approx 0.81 \times 10^{-17}$ m$^2$/W and $\beta_{2PA} \approx 1.89 \times 10^{-11}$ m/W for the film annealed at 215 °C. All films had figures of merit on the order of that of silicon, and the annealed film showed a much higher irradiance damage threshold. Together, this concluded sub-objective 1.

The second part of this work used the optical coefficients previously extracted to design and fabricate GSSe waveguides and ring resonators. Linear propagation loss was measured for bent waveguides with a height of 400 nm and a component width of 3 µm, yielding elevated values of 3.58 dB/mm and an insertion loss of 12 dB/facet, but demonstrating propagation nonetheless, satisfying sub-objective 2. Micro-ring resonators were also demonstrated, as a

foundation for more complete devices down the line. Finally, four-wave mixing was observed in large GSSe waveguides, with an average conversion efficiency of $-54.8$ dB and a peak conversion efficiency of $-27.8$ dB, from which sub-objective 3 was completed. As a whole, the results presented in this work serve as a starting point for more in-depth, complex device fabrication and characterization.

## 6.2 Limitations

As a more general limitation, working with $Ge_2Sb_2Se_5$ posed somewhat of a logistical challenge, given the limited availability of sputtering targets from this material over the course of this thesis. Indeed, both targets had to be specially ordered, and were not readily available, creating additional time constraints on the project.

### 6.2.1 Thin Film Characterization

For the material characterization, XPS measurements were performed on sputtered films, from which an altered stoichiometry was deduced. However, no analysis was done on the sputtering targets themselves, and while they were purchased with 4N purity (99.99%), it is possible that there was innately a composition difference which could account for the observed deviations. Additionally, the sputtering equipment available did not offer substrate rotation, temperature control, or bias control, all of which could be helpful in controlling the film stoichiometry, mechanical properties, and uniformity.

In terms of the oxidation analysis, the depth profiling via XPS to determine the overlayer thickness assumes a uniform layer, which may be inaccurate in practice, and further spatial analysis using a method such as AFM could clarify this assumption of homogeneity. Also, the high-resolution oxidation analysis was not performed on the films from Target 2, which may display slightly different characteristics.

Another notion to verify would be the crystallinity of the samples, with and without annealing. Nucleation was visible at 400 °C, but given the complex nature of the crystallization process when accounting for substrate material, cooling and heating rates, as well as film thickness, a more quantitative analysis could be useful to validate the degree of crystallization and to confirm the amorphous nature of the as-deposited and low-temperature annealed films. In terms of optical characterization, potential crystallinity may also have impeded analysis for the high-temperature annealed samples, affecting the ellipsometric measurements.

For the z-scan process, the first important limitation comes from the nature of the analyzed samples. Given that the goal was to measure the nonlinear coefficients in thin film form, this

required relatively thick films ($\sim 2$ µm) on thin substrates to be able to obtain any readable signal. In fact, a prior experiment was done with a 400 nm GSSe film on a thicker glass substrate, and the nonlinear response was too small to be measurable. The related drawback was that this required the use of very high laser power resulting in high intensity irradiation of the samples, which could damage them in the process. Essentially, the thickness bounded the usable intensity range quite narrowly, which is one of the primary reasons for the uncertainty regarding the order of multi-photon absorption recorded.

### 6.2.2 Waveguides and Resonators

For GSSe waveguides and micro-ring resonators, the primary limitation was a result of fabrication challenges. While fabricating smaller, single-mode structures is theoretically advantageous, the practical realization of these proved to be rather difficult, with the small lithography resolution required for structures narrower than 600 nm and the resist thickness required for lift-off of films over 400 nm. Small structures also had a tendency to become unadhered from the substrate during lift-off, especially if using an ultrasound bath, and in other cases, significant film redeposition was noted and caused broken waveguides. As a result, the waveguides and resonators which were successfully produced were comparatively oversized, which severely limited the efficiency of FWM and likely induced more losses than could be achieved in an optimal scenario. Furthermore, the difficulties in reliably fabricating waveguides and resonators resulted in only a limited number of structures being usable for any experiments, which adds uncertainty as to the repeatability of some of these measurements.

For the four-wave mixing experiments in particular, the limitations were not only the waveguide dimensions being suboptimal, but also to do with the high laser power which was required to observe idler generation as a consequence. Due to the high power, the optical components available risked damage, and polarization controllers were not used. Since FWM is a polarization-sensitive process, the experiment outcome could have been improved in this way. The alignment setup used was also very sensitive to positioning and had a tendency to drift over time, which made acquiring spectra all the more challenging and affected the consistency of the results. The setup could be greatly improved using more stable fibre positioning stages.

## 6.3 Future Research

First and foremost, future work should aim to address the limitations highlighted in the previous section, with focus on fabricating more samples to repeat the necessary measurements,

with more optimal dimensions and characteristics. This would include performing z-scan measurements on thicker GSSe films to expand the range of intensities available, fabricating single-mode waveguides using EBL, and observing resonator-enhanced FWM. Given the observation of oxidation, the addition of a protective cladding on the structures could be examined to prevent long-term degradation, while verifying any impact on performance. The cladding may also improve the performance of grating couplers by reducing back-reflections from the input fibre.

Next, given the preliminary nature of the work reported in this thesis, many avenues remain for future research. As was presented at the beginning of this thesis, one of the primary interests of using GSSe is to exploit the potential photosensitivity of this ChG. To do so, the refractive index modulation of GSSe using near-bandgap illumination should be studied in order to verify the photosensitivity of this material and to quantify the magnitude of this response. The refractive index of the as-deposited films should first be studied before and after illumination with various levels of irradiation and exposure duration. The reversible nature of this process should also be characterized by studying the refractive index change of the illuminated films once they are annealed. Additional consideration should be made regarding the requirement of "priming" the film, where annealing is performed prior to any illumination in order to facilitate the reversion of any refractive index modulation.

Next, given successful fabrication of optimized waveguides coupled with micro-ring resonators, studies should exploit the photosensitivity of GSSe by using illumination to tune the refractive index, and thus the resonant wavelength of the resonators. The use of this tuning mechanism and the reversibility of the process with annealing can then be used to finally fabricate an integrated and reconfigurable photon source. The performance of the photon source could then be further characterized to validate the pair generation rate, and to eventually perform quantum photonics experiments.

# REFERENCES


[1] M. Olivier *et al.*, "Structure, nonlinear properties, and photosensitivity of $(GeSe_2)_{100-x}(Sb_2Se_3)_x$ glasses," *Optical Materials Express*, vol. 4, no. 3, pp. 525–540, Mar. 2014, publisher: Optica Publishing Group. [Online]. Available: https://opg.optica.org/ome/abstract.cfm?uri=ome-4-3-525

[2] T. Wang *et al.*, "Systematic z-scan measurements of the third order nonlinearity of chalcogenide glasses," *Optical Materials Express*, vol. 4, no. 5, pp. 1011–1022, May 2014, publisher: Optica Publishing Group. [Online]. Available: https://opg.optica.org/ome/abstract.cfm?uri=ome-4-5-1011

[3] T. Halenkovič *et al.*, "Amorphous Ge-Sb-Se-Te chalcogenide films fabrication for potential environmental sensing and nonlinear photonics," *Journal of Materiomics*, vol. 8, no. 5, pp. 1009–1019, Sep. 2022. [Online]. Available: https://www.sciencedirect.com/science/article/pii/S2352847822000326

[4] G. Lenz *et al.*, "Large Kerr effect in bulk Se-based chalcogenide glasses," *Optics Letters*, vol. 25, no. 4, pp. 254–256, Feb. 2000, publisher: Optica Publishing Group. [Online]. Available: https://opg.optica.org/ol/abstract.cfm?uri=ol-25-4-254

[5] Y. Hu *et al.*, "Mid-infrared nonlinear optical performances of Ge-Sb-S chalcogenide glasses," *Optical Materials Express*, vol. 11, no. 3, pp. 695–706, Mar. 2021, publisher: Optica Publishing Group. [Online]. Available: https://opg.optica.org/ome/abstract.cfm?uri=ome-11-3-695

[6] A. D. Bristow, N. Rotenberg, and H. M. van Driel, "Two-photon absorption and Kerr coefficients of silicon for 850–2200nm," *Applied Physics Letters*, vol. 90, no. 19, p. 191104, May 2007. [Online]. Available: https://doi.org/10.1063/1.2737359

[7] S. R. Flom *et al.*, "Ultrafast Z-scan measurements of nonlinear optical constants of window materials at 772, 1030, and 1550 nm," *Applied Optics*, vol. 54, no. 31, pp. F123–F128, Nov. 2015, publisher: Optica Publishing Group. [Online]. Available: https://opg.optica.org/ao/abstract.cfm?uri=ao-54-31-F123

[8] C. H. Bennett and G. Brassard, "Quantum cryptography: Public key distribution and coin tossing," *Theoretical Computer Science*, vol. 560, pp. 7–11, Dec. 2014. [Online]. Available: https://www.sciencedirect.com/science/article/pii/S0304397514004241

[9] H. Wang *et al.*, "Progress on Chip-Based Spontaneous Four-Wave Mixing Quantum Light Sources," *Advanced Devices & Instrumentation*, vol. 5, p. 0032, Jan. 2024, publisher: American Association for the Advancement of Science. [Online]. Available: https://spj.science.org/doi/10.34133/adi.0032

[10] P. Huang *et al.*, "Integrated Reconfigurable Photon-Pair Source Based on High-Q Nonlinear Chalcogenide Glass Microring Resonators," *Nano Letters*, vol. 23, no. 10, pp. 4487–4494, May 2023, publisher: American Chemical Society. [Online]. Available: https://doi.org/10.1021/acs.nanolett.3c00858

[11] B. E. A. Saleh and M. C. Teich, *Fundamentals of Photonics*. John Wiley & Sons, Mar. 2020, google-Books-ID: iozUDwAAQBAJ.

[12] A. M. Weiner, *Ultrafast Optics*. John Wiley & Sons, Sep. 2011, google-Books-ID: fhohaV7wJbYC.

[13] R. Boyd, *Nonlinear Optics*. Elsevier Science, 2020. [Online]. Available: https://books.google.ca/books?id=ynzZDwAAQBAJ

[14] C. Lian *et al.*, "Photonic (computational) memories: tunable nanophotonics for data storage and computing," *Nanophotonics*, vol. 11, no. 17, pp. 3823–3854, Sep. 2022, publisher: De Gruyter. [Online]. Available: https://www.degruyter.com/document/doi/10.1515/nanoph-2022-0089/html?lang=en

[15] Y. Zhang *et al.*, "Broadband transparent optical phase change materials for high-performance nonvolatile photonics," *Nature Communications*, vol. 10, no. 1, p. 4279, Sep. 2019, publisher: Nature Publishing Group. [Online]. Available: https://www.nature.com/articles/s41467-019-12196-4

[16] C. Kittel, *Introduction to Solid State Physics*, 8th ed. Wiley, 2004.

[17] A. V. Kolobov and K. Tanaka, "Photoinduced phenomena in amorphous chalcogenides: From phenomenology to nanoscale," in *Handbook of Advanced Electronic and Photonic Materials and Devices*. Academic Press, Jan. 2001, vol. 5, pp. 47–90. [Online]. Available: https://www.sciencedirect.com/science/chapter/edited-volume/abs/pii/B9780125137454500433

[18] J. D. Musgraves, J. Hu, and L. Calvez, *Springer Handbook of Glass*. Springer Nature, Nov. 2019.

[19] Y. Wang, K. D. Jöns, and Z. Sun, "Integrated photon-pair sources with nonlinear optics," *Applied Physics Reviews*, vol. 8, no. 1, p. 011314, Mar. 2021. [Online]. Available: https://doi.org/10.1063/5.0030258

[20] N. Vermeulen *et al.*, "Post-2000 nonlinear optical materials and measurements: data tables and best practices," *Journal of Physics: Photonics*, vol. 5, no. 3, p. 035001, May 2023, publisher: IOP Publishing. [Online]. Available: https://dx.doi.org/10.1088/2515-7647/ac9e2f

[21] M. Guignard *et al.*, "Chalcogenide Glasses Based on Germanium Disulfide for Second Harmonic Generation," *Advanced Functional Materials*, vol. 17, no. 16, pp. 3284–3294, 2007, _eprint: https://onlinelibrary.wiley.com/doi/pdf/10.1002/adfm.200700047. [Online]. Available: https://onlinelibrary.wiley.com/doi/abs/10.1002/adfm.200700047

[22] K. Garay-Palmett *et al.*, "Fiber-based photon-pair generation: tutorial," *JOSA B*, vol. 40, no. 3, pp. 469–490, Mar. 2023, publisher: Optica Publishing Group. [Online]. Available: https://opg.optica.org/josab/abstract.cfm?uri=josab-40-3-469

[23] C. Couteau *et al.*, "Applications of single photons to quantum communication and computing," *Nature Reviews Physics*, vol. 5, no. 6, pp. 326–338, Jun. 2023, publisher: Nature Publishing Group. [Online]. Available: https://www.nature.com/articles/s42254-023-00583-2

[24] E. Delcourt *et al.*, "Self-phase modulation and four-wave mixing in a chalcogenide ridge waveguide," *Optical Materials Express*, vol. 10, no. 6, pp. 1440–1450, Jun. 2020, publisher: Optica Publishing Group. [Online]. Available: https://opg.optica.org/ome/abstract.cfm?uri=ome-10-6-1440

[25] E. Delcourt, "Etude et exaltation des effets non-linéaires d'ordre trois en optique intégrée." Ph.D. dissertation, Université de Rennes, Dec. 2017.

[26] M. R. Krogstad, "Ge-Sb-Se Chalcogenide Glass for Near- and Mid-Infrared Nonlinear Photonics," Ph.D. dissertation, University of Colorado Boulder, 2017. [Online]. Available: https://scholar.colorado.edu/concern/graduate_thesis_or_dissertations/4x51hj00j

[27] M. Sheik-Bahae *et al.*, "Sensitive measurement of optical nonlinearities using a single beam," *IEEE Journal of Quantum Electronics*, vol. 26, no. 4, pp. 760–769, Apr. 1990. [Online]. Available: https://ieeexplore.ieee.org/document/53394/

[28] B.-U. Sohn *et al.*, "Observation of very high order multi-photon absorption in GeSbS chalcogenide glass," *APL Photonics*, vol. 4, no. 3, p. 036102, Mar. 2019. [Online]. Available: https://doi.org/10.1063/1.5085504

[29] D.-Y. Choi *et al.*, "Photo-induced and Thermal Annealing of Chalcogenide Films for Waveguide Fabrication," *Physics Procedia*, vol. 48, pp. 196–205, Jan. 2013. [Online]. Available: https://www.sciencedirect.com/science/article/pii/S1875389213004902

[30] H.-S. P. Wong *et al.*, "Phase Change Memory," *Proceedings of the IEEE*, vol. 98, no. 12, pp. 2201–2227, Dec. 2010, conference Name: Proceedings of the IEEE. [Online]. Available: https://ieeexplore.ieee.org/abstract/document/5609179

[31] K. A. Cerqua-Richardson *et al.*, "Comparison of nonlinear optical properties of sulfide glasses in bulk and thin film form," *Optical Materials*, vol. 10, no. 2, pp. 155–159, May 1998. [Online]. Available: https://www.sciencedirect.com/science/article/pii/S0925346797001420

[32] J. W. Silverstone *et al.*, "Silicon Quantum Photonics," *IEEE Journal of Selected Topics in Quantum Electronics*, vol. 22, no. 6, pp. 390–402, Nov. 2016, conference Name: IEEE Journal of Selected Topics in Quantum Electronics. [Online]. Available: https://ieeexplore.ieee.org/document/7479523

[33] K. Ikeda, Y. Shen, and Y. Fainman, "Enhanced optical nonlinearity in amorphous silicon and its application to waveguide devices," *Optics Express*, vol. 15, no. 26, pp. 17 761–17 771, Dec. 2007, publisher: Optica Publishing Group. [Online]. Available: https://opg.optica.org/oe/abstract.cfm?uri=oe-15-26-17761

[34] K.-Y. Wang and A. C. Foster, "Ultralow power continuous-wave frequency conversion in hydrogenated amorphous silicon waveguides," *Optics Letters*, vol. 37, no. 8, pp. 1331–1333, Apr. 2012, publisher: Optica Publishing Group. [Online]. Available: https://opg.optica.org/ol/abstract.cfm?uri=ol-37-8-1331

[35] C. Lacava *et al.*, "Nonlinear characterization of hydrogenated amorphous silicon waveguides and analysis of carrier dynamics," *Applied Physics Letters*, vol. 103, no. 14, p. 141103, Sep. 2013. [Online]. Available: https://doi.org/10.1063/1.4823579

[36] D. Duchesne *et al.*, "Efficient self-phase modulation in low loss, high index doped silica glass integrated waveguides," *Optics Express*, vol. 17, no. 3, pp. 1865–1870, Feb. 2009, publisher: Optica Publishing Group. [Online]. Available: https://opg.optica.org/oe/abstract.cfm?uri=oe-17-3-1865

[37] D. J. Moss *et al.*, "New CMOS-compatible platforms based on silicon nitride and Hydex for nonlinear optics," *Nature Photonics*, vol. 7, no. 8, pp. 597–607, Aug. 2013, publisher: Nature Publishing Group. [Online]. Available: https://www.nature.com/articles/nphoton.2013.183

[38] D. K. T. Ng *et al.*, "Exploring High Refractive Index Silicon-Rich Nitride Films by Low-Temperature Inductively Coupled Plasma Chemical Vapor Deposition and Applications for Integrated Waveguides," *ACS Applied Materials & Interfaces*, vol. 7, no. 39, pp. 21 884–21 889, Oct. 2015, publisher: American Chemical Society. [Online]. Available: https://doi.org/10.1021/acsami.5b06329

[39] W. C. Hurlbut *et al.*, "Multiphoton absorption and nonlinear refraction of GaAs in the mid-infrared," *Optics Letters*, vol. 32, no. 6, pp. 668–670, Mar. 2007, publisher: Optica Publishing Group. [Online]. Available: https://opg.optica.org/ol/abstract.cfm?uri=ol-32-6-668

[40] D. Franta *et al.*, "Determination of thicknesses and temperatures of crystalline silicon wafers from optical measurements in the far infrared region," *Journal of Applied Physics*, vol. 123, no. 18, p. 185707, May 2018. [Online]. Available: https://doi.org/10.1063/1.5026195

[41] X. Gai *et al.*, "Nonlinear absorption and refraction in crystalline silicon in the mid-infrared," *Laser & Photonics Reviews*, vol. 7, no. 6, pp. 1054–1064, 2013, _eprint: https://onlinelibrary.wiley.com/doi/pdf/10.1002/lpor.201300103. [Online]. Available: https://onlinelibrary.wiley.com/doi/abs/10.1002/lpor.201300103

[42] C. Grillet *et al.*, "Amorphous silicon nanowires combining high nonlinearity, FOM and optical stability," *Optics Express*, vol. 20, no. 20, pp. 22 609–22 615, Sep. 2012, publisher: Optica Publishing Group. [Online]. Available: https://opg.optica.org/oe/abstract.cfm?uri=oe-20-20-22609

[43] D. Franta *et al.*, "Optical characterization of SiO2 thin films using universal dispersion model over wide spectral range," in *Optical Micro- and Nanometrology VI*, vol. 9890. SPIE, Apr. 2016, pp. 253–267. [Online]. Available: https://www.spiedigitallibrary.org/conference-proceedings-of-spie/9890/989014/Optical-characterization-of-SiO2-thin-films-using-universal-dispersion-model/10.1117/12.2227580.full

[44] A. Rahim *et al.*, "Expanding the Silicon Photonics Portfolio With Silicon Nitride Photonic Integrated Circuits," *Journal of Lightwave Technology*, vol. 35, no. 4, pp. 639–649, Feb. 2017. [Online]. Available: https://ieeexplore.ieee.org/document/7589975

[45] T. Wang *et al.*, "Supercontinuum generation in bandgap engineered, back-end CMOS compatible silicon rich nitride waveguides," *Laser & Photonics Reviews*, vol. 9, no. 5, pp. 498–506, 2015, _eprint: https://onlinelibrary.wiley.com/doi/pdf/10.1002/lpor.201500054. [Online]. Available: https://onlinelibrary.wiley.com/doi/abs/10.1002/lpor.201500054

[46] J. Aitchison *et al.*, "The nonlinear optical properties of AlGaAs at the half band gap," *IEEE Journal of Quantum Electronics*, vol. 33, no. 3, pp. 341–348, Mar. 1997. [Online]. Available: https://ieeexplore.ieee.org/document/556002

[47] D. J. Wilson *et al.*, "Integrated gallium phosphide nonlinear photonics," *Nature Photonics*, vol. 14, no. 1, pp. 57–62, Jan. 2020, publisher: Nature Publishing Group. [Online]. Available: https://www.nature.com/articles/s41566-019-0537-9

[48] S. J. Madden *et al.*, "Long, low loss etched $As_2S_3$ chalcogenide waveguides for all-optical signal regeneration," *Optics Express*, vol. 15, no. 22, pp. 14 414–14 421, Oct. 2007, publisher: Optica Publishing Group. [Online]. Available: https://opg.optica.org/oe/abstract.cfm?uri=oe-15-22-14414

[49] S. Dai *et al.*, "Mid-infrared optical nonlinearities of chalcogenide glasses in Ge-Sb-Se ternary system," *Optics Express*, vol. 23, no. 2, pp. 1300–1307, Jan. 2015, publisher: Optica Publishing Group. [Online]. Available: https://opg.optica.org/oe/abstract.cfm?uri=oe-23-2-1300

[50] J. S. Sanghera *et al.*, "Non-linear properties of chalcogenide glasses and fibers," *Journal of Non-Crystalline Solids*, vol. 354, no. 2, pp. 462–467, Jan. 2008. [Online]. Available: https://www.sciencedirect.com/science/article/pii/S0022309307010915

[51] S. Serna *et al.*, "Nonlinear optical properties of integrated GeSbS chalcogenide waveguides," *Photonics Research*, vol. 6, no. 5, pp. B37–B42, May 2018, publisher: Optica Publishing Group. [Online]. Available: https://opg.optica.org/prj/abstract.cfm?uri=prj-6-5-B37

[52] F. Han *et al.*, "Mitigating waveguide loss in Ge–Sb–Se chalcogenide glass photonics," *Journal of Physics D: Applied Physics*, vol. 57, no. 30, p. 305107, May 2024, publisher: IOP Publishing. [Online]. Available: https://dx.doi.org/10.1088/1361-6463/ad43f5

[53] K. Lei *et al.*, "Hybrid silicon-chalcogenide glass-integrated photonic platform for EDFA-free four-wave mixing," *Optics Letters*, vol. 50, no. 17, pp. 5426–5429, Sep. 2025, publisher: Optica Publishing Group. [Online]. Available: https://opg.optica.org/ol/abstract.cfm?uri=ol-50-17-5426

[54] R. A. Loretz, T. J. Loretz, and K. A. Richardson, "Predictive method to assess chalcogenide glass properties: bonding, density and the impact on glass properties," *Optical Materials Express*, vol. 12, no. 5, pp. 2012–2027, May 2022, publisher: Optica Publishing Group. [Online]. Available: https://opg.optica.org/ome/abstract.cfm?uri=ome-12-5-2012

[55] J.-B. Dory *et al.*, "Ge–Sb–S–Se–Te amorphous chalcogenide thin films towards on-chip nonlinear photonic devices," *Scientific Reports*, vol. 10, no. 1, p. 11894, Jul. 2020, publisher: Nature Publishing Group. [Online]. Available: https://www.nature.com/articles/s41598-020-67377-9

[56] ——, "Origin of the Unusual High Optical Nonlinearities Observed in Glassy Chalcogenides," *Advanced Optical Materials*, vol. 11, no. 24, p. 2301154, 2023, _eprint: https://onlinelibrary.wiley.com/doi/pdf/10.1002/adom.202301154. [Online]. Available: https://onlinelibrary.wiley.com/doi/abs/10.1002/adom.202301154

[57] E. Baudet *et al.*, "Experimental design approach for deposition optimization of RF sputtered chalcogenide thin films devoted to environmental optical sensors," *Scientific Reports*, vol. 7, no. 1, p. 3500, Jun. 2017, number: 1 Publisher: Nature Publishing Group. [Online]. Available: https://www.nature.com/articles/s41598-017-03678-w

[58] M. Grayson *et al.*, "Enhancement of third-order nonlinearity of thermally evaporated GeSbSe waveguides through annealing," *Optics Express*, vol. 27, no. 23, pp. 33 606–33 620, Nov. 2019, publisher: Optica Publishing Group. [Online]. Available: https://opg.optica.org/oe/abstract.cfm?uri=oe-27-23-33606

[59] M. J. Madou, *Fundamentals of Microfabrication: The Science of Miniaturization, Second Edition*, 2nd ed. Boca Raton: CRC Press, Oct. 2018.

[60] M. Olivier *et al.*, "Photosensitivity of pulsed laser deposited Ge-Sb-Se thin films," *Optical Materials Express*, vol. 5, no. 4, pp. 781–793, Apr. 2015, publisher: Optica Publishing Group. [Online]. Available: https://opg.optica.org/ome/abstract.cfm?uri=ome-5-4-781

[61] D. Sahoo and R. Naik, "A review on the linear/nonlinear optical properties of Se doped chalcogenide thin films as potential optoelectronic applications," *Journal*

*of Non-Crystalline Solids*, vol. 597, p. 121934, Dec. 2022. [Online]. Available: https://www.sciencedirect.com/science/article/pii/S0022309322005294

[62] T. Kuriakose *et al.*, "Measurement of ultrafast optical Kerr effect of Ge–Sb–Se chalcogenide slab waveguides by the beam self-trapping technique," *Optics Communications*, vol. 403, pp. 352–357, Nov. 2017. [Online]. Available: https://www.sciencedirect.com/science/article/pii/S003040181730648X

[63] M. Grayson *et al.*, "Fabrication and characterization of high quality GeSbSe reflowed and etched ring resonators," *Optics Express*, vol. 30, no. 17, pp. 31 107–31 121, Aug. 2022, publisher: Optica Publishing Group. [Online]. Available: https://opg.optica.org/oe/abstract.cfm?uri=oe-30-17-31107

[64] G. W. Burr *et al.*, "Phase change memory technology," *Journal of Vacuum Science & Technology B*, vol. 28, no. 2, pp. 223–262, Mar. 2010. [Online]. Available: https://doi.org/10.1116/1.3301579

[65] S. Raoux, W. Wełnic, and D. Ielmini, "Phase Change Materials and Their Application to Nonvolatile Memories," *Chemical Reviews*, vol. 110, no. 1, pp. 240–267, Jan. 2010, publisher: American Chemical Society. [Online]. Available: https://doi.org/10.1021/cr900040x

[66] J. R. Rodriguez *et al.*, "Ge2Sb2Se5 Glass as High-capacity Promising Lithium-ion Battery Anode," *Nano Energy*, vol. 68, p. 104326, Feb. 2020. [Online]. Available: https://www.sciencedirect.com/science/article/pii/S221128551931033X

[67] T. Lacasse, "Mémoire optique à changement de phase pour calcul neuromorphique destiné à l'intelligence artificielle," Master's thesis, Polytechnique Montréal, Aug. 2023. [Online]. Available: https://publications.polymtl.ca/55106/

[68] T. Halenkovič *et al.*, "Linear and nonlinear optical properties of co-sputtered Ge-Sb-Se amorphous thin films," *Optics Letters*, vol. 45, no. 6, pp. 1523–1526, Mar. 2020, publisher: Optica Publishing Group. [Online]. Available: https://opg.optica.org/ol/abstract.cfm?uri=ol-45-6-1523

[69] H. Shahrokhabadi, A. Bananej, and M. Vaezzadeh, "Investigation of Cody–Lorentz and Tauc–Lorentz Models in Characterizing Dielectric Function of (HfO2)x(ZrO2)1–xMixed Thin Film," *Journal of Applied Spectroscopy*, vol. 84, no. 5, pp. 915–922, Nov. 2017. [Online]. Available: https://doi.org/10.1007/s10812-017-0565-5

[70] P. Němec, V. Nazabal, and M. Frumar, "Photoinduced phenomena in amorphous As4Se3 pulsed laser deposited thin films studied by spectroscopic ellipsometry," *Journal of Applied Physics*, vol. 106, no. 2, p. 023509, Jul. 2009. [Online]. Available: https://doi.org/10.1063/1.3173279

[71] J. Klein *et al.*, "Limitations of the Tauc Plot Method," *Advanced Functional Materials*, vol. 33, no. 47, p. 2304523, 2023, _eprint: https://advanced.onlinelibrary.wiley.com/doi/pdf/10.1002/adfm.202304523. [Online]. Available: https://onlinelibrary.wiley.com/doi/abs/10.1002/adfm.202304523

[72] E. Mammadov *et al.*, "Comparison of Optical Parameters of Ge–As(Sb)–Se(Te) Glassy Films," *Japanese Journal of Applied Physics*, vol. 50, no. 5S2, p. 05FC12, May 2011, publisher: IOP Publishing. [Online]. Available: https://iopscience.iop.org/article/10.1143/JJAP.50.05FC12/meta

[73] T. Halenkovič *et al.*, "Insight into the photoinduced phenomena in ternary Ge-Sb-Se sputtered thin films," *Photonics Research*, vol. 10, no. 9, pp. 2261–2266, Sep. 2022, publisher: Optica Publishing Group. [Online]. Available: https://opg.optica.org/prj/abstract.cfm?uri=prj-10-9-2261

[74] A. Zakery and S. R. Elliott, *Optical Nonlinearities in Chalcogenide Glasses and Their Applications*. Springer Science & Business Media, Jun. 2007, google-Books-ID: LD-Fkybb3R0IC.

[75] B. Gu, W. Ji, and X.-Q. Huang, "Analytical expression for femtosecond-pulsed *Z* scans on instantaneous nonlinearity," *Applied Optics*, vol. 47, no. 9, pp. 1187–1192, Mar. 2008, publisher: Optica Publishing Group. [Online]. Available: https://opg.optica.org/ao/abstract.cfm?uri=ao-47-9-1187

[76] M. Chen *et al.*, "High-sensitivity measurements of the nonlinear absorption coefficient of wide bandgap oxide thin films with the Z-scan method," *Optical Materials Express*, vol. 12, no. 2, pp. 533–544, Feb. 2022, publisher: Optica Publishing Group. [Online]. Available: https://opg.optica.org/ome/abstract.cfm?uri=ome-12-2-533

[77] A. Gnoli, L. Razzari, and M. Righini, "Z-scan measurements using high repetition rate lasers: how to manage thermal effects," *Optics Express*, vol. 13, no. 20, pp. 7976–7981, Oct. 2005, publisher: Optica Publishing Group. [Online]. Available: https://opg.optica.org/oe/abstract.cfm?uri=oe-13-20-7976

[78] R. D. Nalda *et al.*, "Limits to the determination of the nonlinear refractive index by the Z-scan method," *Journal of the Optical Society of America B*, vol. 19, no. 2, p. 289, Feb. 2002. [Online]. Available: https://opg.optica.org/abstract.cfm?URI=josab-19-2-289

[79] "Infrared glasses and materials technical properties | SCHOTT." [Online]. Available: https://www.schott.com/en-ca/products/infrared-glasses-and-materials-p1000261/technical-details

[80] M. Dinu, F. Quochi, and H. Garcia, "Third-order nonlinearities in silicon at telecom wavelengths," *Applied Physics Letters*, vol. 82, no. 18, pp. 2954–2956, May 2003. [Online]. Available: https://doi.org/10.1063/1.1571665

[81] G. Boudebs *et al.*, "Experimental observation of higher order nonlinear absorption in tellurium based chalcogenide glasses," *Optics Communications*, vol. 232, no. 1, pp. 417–423, Mar. 2004. [Online]. Available: https://www.sciencedirect.com/science/article/pii/S0030401803024258

[82] B. Gu *et al.*, "Z-scan theory for material with two- and three-photon absorption," *Optics Express*, vol. 13, no. 23, pp. 9230–9234, Nov. 2005, publisher: Optica Publishing Group. [Online]. Available: https://opg.optica.org/oe/abstract.cfm?uri=oe-13-23-9230

[83] J. Wang *et al.*, "Z-scan theory with simultaneous two- and three-photon absorption saturation," *Optics & Laser Technology*, vol. 44, no. 2, pp. 390–393, Mar. 2012. [Online]. Available: https://www.sciencedirect.com/science/article/pii/S0030399211002283

[84] P. Kultavewuti, "Integrated Sources of Polarization Entangled Photon Pair States via Spontaneous Four-Wave Mixing in AlGaAs Waveguides," Ph.D., University of Toronto (Canada), Canada – Ontario, CA, 2017, iSBN: 9780355446289. [Online]. Available: https://www.proquest.com/docview/1991041945/abstract/E947F37BA9A0403CPQ/2

[85] C. K. Lai *et al.*, "Integrated nonlinear photonics with chalcogenide glasses: compositions, properties, applications, and roadmap [Invited]," *Optical Materials Express*, vol. 15, no. 12, pp. 3210–3241, Dec. 2025, publisher: Optica Publishing Group. [Online]. Available: https://opg.optica.org/ome/abstract.cfm?uri=ome-15-12-3210

[86] L. Chrostowski and M. Hochberg, *Silicon Photonics Design: From Devices to Systems*. Cambridge: Cambridge University Press, 2015. [Online]. Available: https://www.cambridge.org/core/books/silicon-photonics-design/BF3CF13E8542BCE67FD2BBC7104ECEAB

[87] Y. Wang, "Grating coupler design based on silicon-on-insulator," Ph.D. dissertation, University of British Columbia, 2013. [Online]. Available: https://open.library.ubc.ca/soa/cIRcle/collections/ubctheses/24/items/1.0073806

[88] P. P. Absil *et al.*, "Wavelength conversion in GaAs micro-ring resonators," *Optics Letters*, vol. 25, no. 8, pp. 554–556, Apr. 2000, publisher: Optica Publishing Group. [Online]. Available: https://opg.optica.org/ol/abstract.cfm?uri=ol-25-8-554

[89] G. Agrawal, *Nonlinear Fiber Optics*, 3rd ed., ser. Optics and Photonics. Academic Press, Oct. 2012. [Online]. Available: https://www.sciencedirect.com/book/monograph/9780123970237/nonlinear-fiber-optics

# APPENDIX A ELLIPSOMETRY

Results of ellipsometry fits using Cody-Lorentz model for each sample. Resulting Tauc plots are also presented.

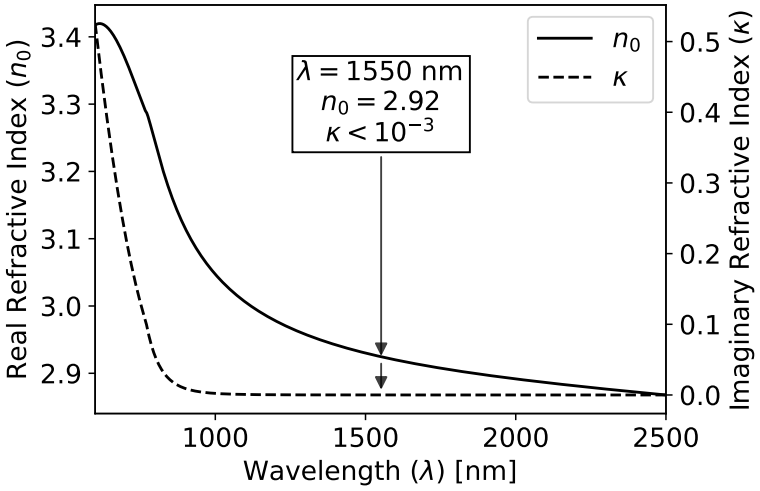


(a) Refractive index

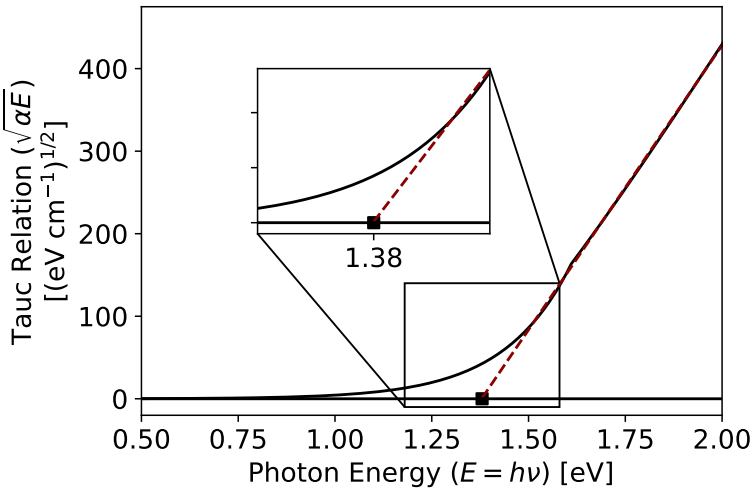


(b) Tauc plot

Figure A.1 Sample 1 data (Target 1 – as-deposited).

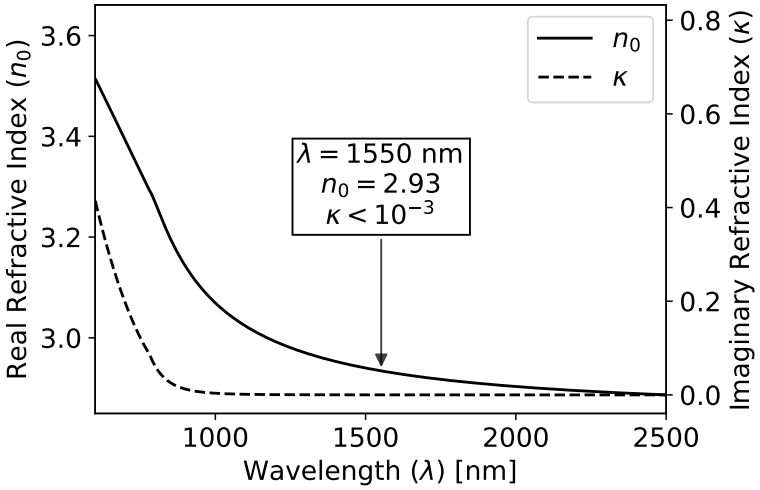


(a) Refractive index

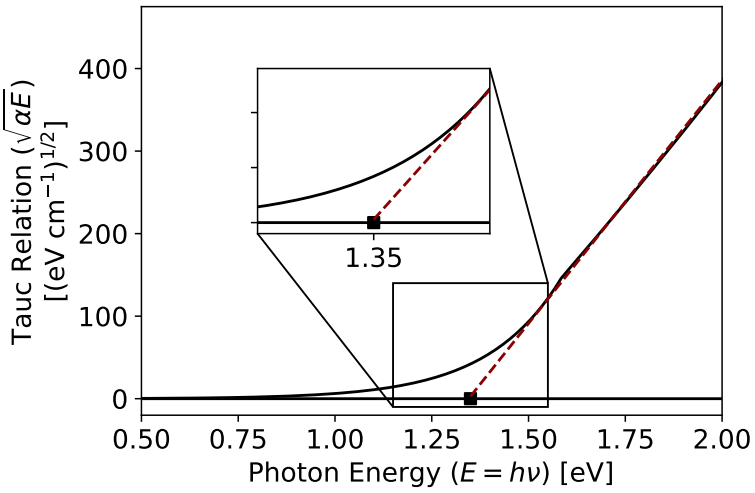


(b) Tauc plot

Figure A.2 Sample 2 data (Target 2 – as-deposited).

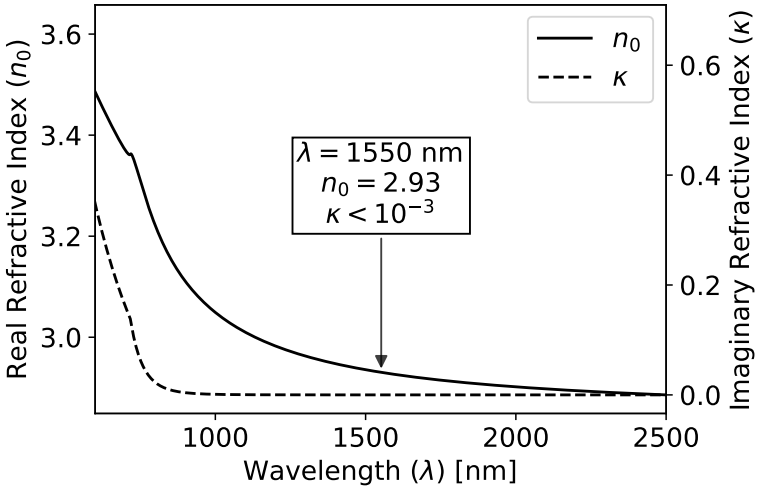


(a) Refractive index

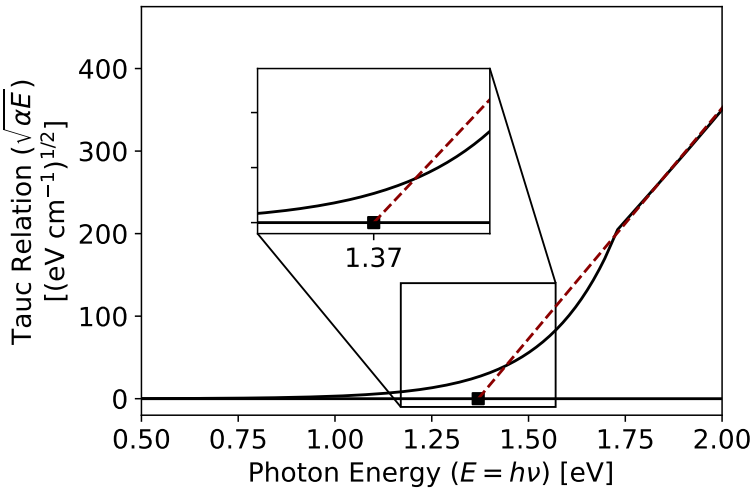


(b) Tauc plot

Figure A.3 Sample 3 data (Target 2 – 215 °C).

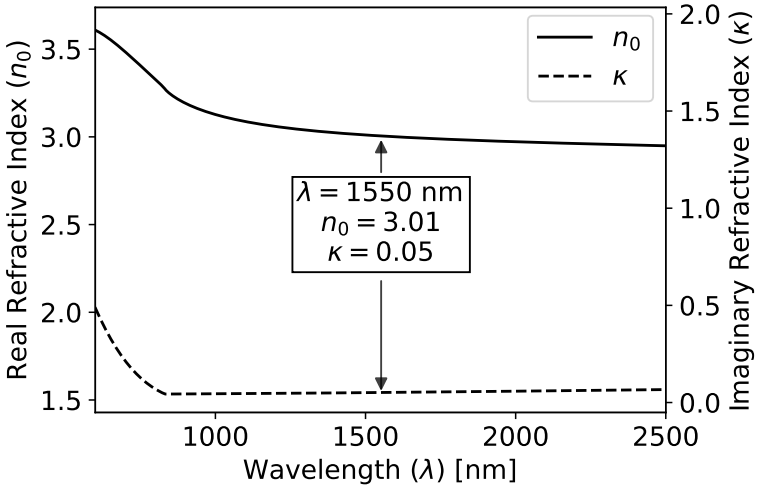


(a) Refractive index

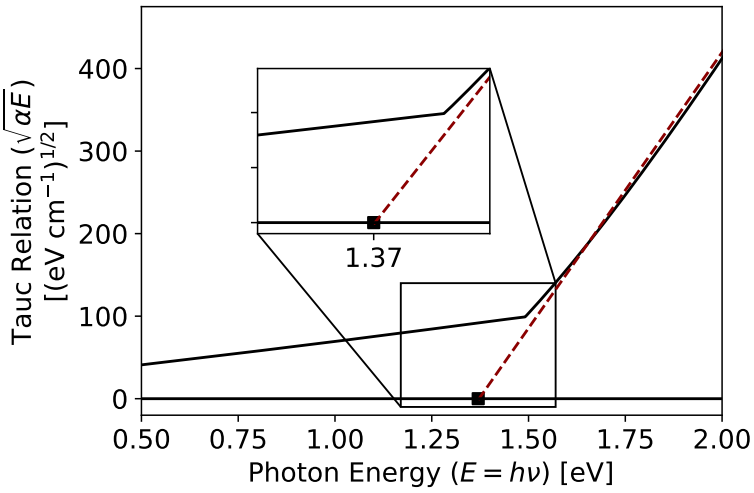


(b) Tauc plot

Figure A.4 Sample 4 data (Target 2 – 400 °C).

# APPENDIX B Z-SCAN PROCESS

The data processing for the z-scans is clarified in further detail here. This process, as well as the python code used, was designed by Pierre-Luc Thériault at Polytechnique Montréal.

First, since the measured laser output power is read from a power meter in a separate reference branch, a second power meter is placed at the sample's position to allow us to accurately correlate the power in the reference branch during the measurement to the power actually received at the sample. The power at the sample position is plotted against the power at the reference and a linear fit is performed to obtain the calibration incident power ratio.

Next, the beam waist radius at focus is calculated by placing the photodetector itself at the sample position and translating it across the $z$ optical axis, with the laser on. Snapshots are taken and the imaged beam diameter is measured at each point. A fit of the diameter data is then performed using the Gaussian beam equation, while letting the beam quality factor $M^2$ vary as a parameter to account for imperfections. The fitted waist is used for subsequent calculations.

Then, the photodetector's integration time may need to be adjusted when the laser power is changed in order to avoid saturation or weak signal. With the laser output off, the background noise of the photodetector is measured with the sample in place over a range of exposure durations. This result is interpolated to allow a calculation of the expected background noise using each experiment's actual integration time. The experiment-specific background noise can then be later subtracted from the recorded transmission.

The sample is placed on a motorized stage programmed to travel through the focal point of the Gaussian laser beam. As the stage translates, the InGaAs detector captures snapshots of the transmitted beam profile at specified intervals. For each of these snapshots, a two-dimensional Gaussian profile is fitted around the brightest spot of the image. In order to obtain the open aperture transmission data points, the intensity is integrated over the entire area of the detector. For the closed aperture data points, a circular mask of $N$ pixels around the central point of the beam is included in the calculation. The closed aperture trace is normalized, dividing by the open aperture data, while the open aperture trace is normalized to its maximum.